AD-A097 811   WYOMING UNIV LARAMIE DEPT OF MECHANICAL ENGINEERING   F/G 11/4
                FINITE ELEMENT MICROMECHANICAL ANALYSIS OF A UNIDIRECTIONAL COM--ETC(U)
   FEB 81 D A CRANE, D F ADAMS   DAAG46-79-C-0076
UNCLASSIFIED   UWME-DR-101-101-1   AMMRC-TR-81-7   NL

LEVEL

AD

AMMRC TR 81-7

FINITE ELEMENT MICROMECHANICAL ANALYSIS OF A UNIDIRECTIONAL COMPOSITE INCLUDING LONGITUDINAL SHEAR LOADING

February 1981

David A. Crane
Donald F. Adams

Composite Materials Research Group
Mechanical Engineering Department
University of Wyoming
Laramie, Wyoming 82071

FINAL REPORT   Contract No. DAAG46-79-C-0076

DTIC
ELECTE
APR 1 0 1981
S   D
C

DTIC FILE COPY

Prepared for

ARMY MATERIALS AND MECHANICS RESEARCH CENTER
Watertown, Massachusetts   02172

81 4 10 001

DISPOSITION INSTRUCTIONS

AMMRC REPORT NO.
AMMRC TR-81-7

WYOMING REPORT NO.
UWME-DR-101-101-1

FINITE ELEMENT MICROMECHANICAL ANALYSIS OF

A UNIDIRECTIONAL COMPOSITE INCLUDING

LONGITUDINAL SHEAR LOADING.

FINAL REPORT.

Sep 77 - Dec 80

DAVID A. CRANE

DONALD F. ADAMS

DTIC
ELECTE
APR 1 0 1981
S
D
C

FEBRUARY 1981

ARMY MATERIALS AND MECHANICS RESEARCH CENTER

CONTRACT NO. DAAG46-79-C-0076

1L161102AH42

COMPOSITE MATERIALS RESEARCH GROUP

MECHANICAL ENGINEERING DEPARTMENT

UNIVERSITY OF WYOMING

LARAMIE, WYOMING 82071

REPORT DOCUMENTATION PAGE	READ INSTRUCTIONS BEFORE COMPLETING FORM

1. REPORT NUMBER	2. GOVT ACCESSION NO.	3. RECIPIENT'S CATALOG NUMBER
AMMRC TR 81-7	AD-A097 811	

4. TITLE *(and Subtitle)*	5. TYPE OF REPORT & PERIOD COVERED
Finite Element Micromechanical Analysis of a Unidirectional Composite Including Longitudinal Shear Loading	Final Report September 1979–December 1980
	6. PERFORMING ORG. REPORT NUMBER UWME-DR-101-101-1

7. AUTHOR(s)	8. CONTRACT OR GRANT NUMBER(s)
David A. Crane Donald F. Adams	DAAG46-79-C-0076

9. PERFORMING ORGANIZATION NAME AND ADDRESS	10. PROGRAM ELEMENT. PROJECT, TASK AREA & WORK UNIT NUMBERS
Composite Materials Research Group Mechanical Engineering Department University of Wyoming Laramie, Wyoming 82071	D/A Project:1L61102AH42 AMCMS Code: 611102.11.42

11. CONTROLLING OFFICE NAME AND ADDRESS	12. REPORT DATE
Army Materials and Mechanics Research Center Watertown, Massachusetts 02172	February 1981
	13. NUMBER OF PAGES 117

14. MONITORING AGENCY NAME & ADDRESS(if different from Controlling Office)	15. SECURITY CLASS. (of this report)
	Unclassified
	15a. DECLASSIFICATION/DOWNGRADING SCHEDULE

16. DISTRIBUTION STATEMENT (of this Report)

Approved for public release; distribution unlimited

17. DISTRIBUTION STATEMENT (of the abstract entered in Block 20, if different from Report)

18. SUPPLEMENTARY NOTES

The view, opinions, and/or findings contained in this report are those of the authors and should not be construed as an official Department of the Army position, policy, or decision, unless so designated by other documentation.

19. KEY WORDS (Continue on reverse side if necessary and identify by block number)

Composite materials	Elastoplastic materials
Micromechanics analysis	Temperature effects
Finite element analysis	Moisture effects
Longitudinal shear loading	Fiber anisotropy

20. ABSTRACT (Continue on reverse side if necessary and identify by block number)

A microscopic region of a unidirectional composite is modeled by a finite element micromechanical analysis using a generalized plane strain formulation, but including longitudinal shear loading. The analysis is capable of treating elastic, transversely isotropic fiber materials, as well as isotropic, elastoplastic matrix materials. Matrix material properties are considered to be temperature- and/or moisture-dependent. A special Gaussian elimination procedure is modified for the present treatment. Stresses are

DD FORM 1473 EDITION OF 1 NOV 65 IS OBSOLETE

calculated for each element and appropriate failure criteria invoked. First-element failure is the limit of the present analysis. Other possible forms of results are: unidirectional composite properties, overall composite stress-strain response, and various plots of internal stress contours.

The longitudinal shear loading capability permits the analysis of shear response of unidirectional composites in the fiber direction. Solid rod torsion test data used to obtain experimental verification indicate good agreement with the theoretical predictions for glass/epoxy and graphite/epoxy at various temperature and moisture conditions.

In conjunction with a laminated plate point stress analysis, the present micromechanical analysis has been used to predict the stress-strain response into the inelastic range of a graphite/epoxy $[\pm45]_{4S}$ laminate. Available experimental data for various environmental conditions indicate excellent agreement with the analytical predictions.

FORWARD

This Final Report presents the results of a one-year study of the title problem under Contract DAAG46-79-C-0076 for the Army Materials and Mechanics Research Center (AMMRC), Watertown, Massachusetts. Initially the AMMRC Program Monitor was Dr. Byung-Lip Lee of the Composites Division. The study was completed under the direction of Dr. Robert Lewis, Chief, Composites Division.

Program Manager and Principal Investigator at the University of Wyoming was Dr. Donald F. Adams, Professor of Mechanical Engineering. Co-Principal Investigator was Mr. David E. Walrath, Staff Scientist in Mechanical Engineering. The study was conducted by Mr. David A. Crane, Graduate Student in Mechanical Engineering, as a Masters Thesis under the direction of Dr. D.F. Adams.

The assistance of graduate students Mohamed M. Monib and Daniel P. Murphy, through their many discussions of topics of mutual interest, is gratefully acknowledged.

Accession For

NTIS GRA&I

DTIC TAB

Unannounced

Justification

By

Distribution/

Availability Codes

Avail and/or

Dist   Special

A

TABLE OF CONTENTS

LIST OF FIGURES

LIST OF TABLES

LIST OF SYMBOLS

a_i, b_i, c_i, a_j, etc.	Coordinate position constants for shape function
$[B]$	Gradient shape function matrix
BW	Bandwidth
C_1, C_2, C_3 ... C_6	Experimentally determined constants for least squares curve fit
$[D]$	Material properties matrix
E, E'	Modulus of elasticity, longitudinal and transverse, respectively
$\{F\}$	Element nodal force vector
G'	Longitudinal shear modulus
$[K]^e$	Element stiffness matrix
K_{11}, K_{12}, etc.	Element stiffness matrix terms
M	Percent moisture by weight
$2M_T$	Octahedral shear stress - plastic octahedral shear strain tangent modulus
N_i, N_j, N_k	Shape functions
n	Inverse of radius of curvature in Richard-Blacklock equation
P_1, P_2, P_3, etc.	Stress allowables
R	Highest difference in element node number
S_{ij}, s_{ij}	Deviatoric stress tensor
T	Temperature
u, v, w	Node point displacement component in x, y, z directions

w_n	Constant z-displacement component
x, y, z	Micromechanics coordinate directions
X, Y, Z	Ply coordinate directions
1, 2, 3	Laminate coordinate directions
a_1, a_2, a_3, etc.	Arbitrary variables in shape function derivation
α_L, α_T	Coefficient of thermal expansion, longitudinal and transverse, respectively
β_L, β_T	Coefficient of moisture expansion, longitudinal and transverse, respectively
γ	Shear strain
γ_{xy}, γ_{xz}, γ_{yz}	Shear strain components
δ_i	Node point displacement
$\{\delta\}$	Element node point displacement vector
δ_{ij}	Kronecker delta
ε	Strain
ε_x, ε_y, ε_z	Normal strain components
$\{\varepsilon\}$	Element strain vector
λ	Arbitrary scalar
ν	Poisson's ratio
σ	Stress
σ_x, σ_y, σ_z	Normal stress components
$\bar{\sigma}_x$, $\bar{\sigma}_y$, $\bar{\sigma}_z$	Average applied normal stresses
$\{\sigma\}$	Element stress vector
σ_0	Asymptotic stress value in Richard-Blacklock equation

τ	Shear stress
τ_{xy}, τ_{xz}, τ_{yz}	Shear stress components
$\overline{\tau}_{xy}$, $\overline{\tau}_{xz}$, $\overline{\tau}_{yz}$	Average applied shear stresses

SECTION 1

INTRODUCTION

The benefits and shortcomings of micromechanical analyses of uni-
directional composites have now been weighed for over a decade. A
major restriction has been the problem of relating microanalyses to
the overall behavior of a laminate. To gain insight into this prob-
lem, it is instructive to consider the well-known process of design-
ing with metals as opposed to the task of employing advanced compo-
sites in structures.

For centuries metals have been the materials considered almost
universally for countless applications. Metals with the desired stiff-
ness, strength, toughness, etc., can be chosen from information at
arm's reach, for each specific application. This vast amount of in-
formation has greatly simplified design using metals. But because
metals are in most cases isotropic and ultimate strengths pertain to
all material directions, there is often unneeded strength in certain
material directions. A truss member to be loaded axially in tension,
for example, requires high strength in the axial direction, but trans-
versely only minimal strength is needed. Thus, the high degree of ani-
sotropy typically exhibited by a composite material is not necessarily
a handicap in many high-performance structures. Composite materials
can be chosen for weight savings, and designed to specific strength
requirements in specific material directions. Because of the vast
possibilities created through material design for specific

applications, the use of composite materials has initiated a new era of materials technology, and the result is that a much more complete approach to structural mechanics has become necessary.

The transition from the use of simple isotropic metals to orthotropic composite plies and anisotropic laminates for structural systems necessitates much more involved analysis methods. While design with metals has been practical for centuries, composite materials are just emerging from their own "Iron Age." A large amount of analysis and technology must be developed before the full potential of composite materials can be realized.

While overall properties of a material are needed for the design of any part, an additional dimension of composite materials behavior is the unique problem of the complex stress state present on the microscopic scale. When a fiber of high strength and modulus is imbedded in a matrix material of relatively low strength and modulus, local stress concentrations are induced that are significant to the overall behavior of the composite. The mathematical characterization of this situation is known as micromechanics analysis while a larger scale analysis, i.e., lamination theory, is known as macromechanics.

Macromechanics is concerned with the overall properties of a composite laminate, or can be concerned with the contribution of each ply to the overall effect. In contrast, micromechanics attempts to predict such phenomena as matrix yielding, crack initiation, and unidirectional composite ply behavior, using an analysis concerned with the local scale. This is important for understanding particular failure initiation modes and predicting properties of unidirectional

composites. Most existing micromechanics analyses employ a finite element numerical scheme, using the material properties of fiber and matrix to predict the microstress distributions, assuming a state of generalized plane strain. This type of analysis could also be performed using a three-dimensional finite element analysis, although much more computer time and memory would be necessary. Ideally, a three-dimensional micromechanics analysis should eventually be developed as a check of the generalized plane strain formulation. While previously existing analyses allow only a longitudinal normal load in the out-of-plane direction, the present analysis permits a longitudinal shear loading capability. Miller and Adams [1] predicted in 1977, "more attempts will be forthcoming to marry micromechanical analyses . . . with various lamination analyses," and this is one of the primary reasons for the addition of a longitudinal shear loading capability. Results of a laminate point stress analysis can be analyzed further by using such a micromechanics formulation. The laminate analysis will reveal the stress state in each ply, from which the microanalysis can predict local inelastic behavior and reveal the complex stress state within the matrix material. This type of analysis can be considered to be an important first step in bridging the gap between micromechanics and macromechanics.

SECTION 2

HISTORICAL REVIEW

The importance of longitudinal shear stress in a composite material is evidenced by the fact that load is transferred to a fiber predominantly through longitudinal shear loading. This stress also happens to act in a weak direction of the composite, making it a critical load. Even though longitudinal shear loading is an important consideration, there have been few studies of it pertaining to micromechanics of a composite.

Early in 1967, Adams and Doner [2] revealed a numerical formulation involving the theory of elasticity. They modeled one quadrant of a repeating fundamental region of a rectangular array of fibers by employing a finite difference representation, and subsequently solved the problem by an over-relaxation procedure. Stress concentration factors and composite shear moduli were calculated for various fiber volumes for a number of cross-sectional shapes of fibers in an epoxy matrix. This first step was soon multiplied as numerical analyses developed and computers became more advanced.

A few years later, a closed form series solution was developed by Sendeckyj [3] for longitudinal shear loading. Admittedly, the solution was tedious due to the solution technique employed, and fell short of being exact due to the required truncation of the infinite series. Nonuniform fiber spacing, various filament radii and

variation of the shear modulus from fiber to fiber were some of the impressive capabilities.

Another elastic solution was achieved by Foye [4] in 1968. The finite element numerical method was employed in this sweeping generalized plane strain study, which included two fiber arrangements, separate and combined loading of five of the six components of stress, contours of stresses in the matrix around a fiber, unidirectional ply composite properties, and an evaluation of the accuracy of various finite element models. In addition, an incremental inelastic analysis was proposed, which was eventually employed by Baker and Foye [5] in 1969. This extended work revealed a more legitimate stress distribution because inelastic behavior was considered. Foye continued to publish results of this analysis in 1970 [6] and 1973 [7]. The work documented in 1973 essentially clarified the aforementioned work of 1969 [5].

Although this analysis was a significant achievement, there were still some limitations to be overcome. The iterative scheme inherently accumulated error during inelastic increments which would grow to significant size as the number of inelastic increments increased. The iterative inelastic analysis, termed the method of initial strains, had been chosen, even though it degenerates for highly inelastic behavior, because the alternative method (the tangent modulus method) would have required an unavailable amount of computer memory for the additional longitudinal shear loading capability. Even though the method of initial strains had the advantage of requiring only one

initial inversion of the stiffness matrix, the tangent modulus method was found to be slightly faster, with equal accuracy and the ability to model highly inelastic materials [8].

In the past 15 years, computers have been developed considerably, and the disadvantages attributed to the tangent modulus method have been blunted by the increased size of computer memory. Advantages of the tangent modulus approach began to clearly emerge in the analysis presented by Adams [9, 10] in 1970. This was further developed in his subsequent work reported in References [11, 12, 13, 14]. This analysis method was subsequently adapted by Miller and Adams [1, 15, 16], incorporating work by Crossman [17] and Branca [18]. It was a generalized plane strain formulation, including longitudinal normal loading, but not longitudinal shear. The work of Miller and Adams was particularly valuable due to the addition of a hygrothermal loading capability along with hygrothermally-dependent material properties, and Branca's [18] efficient loading scheme. This generalized plane strain approach is readily expanded to include a longitudinal shear loading capability.

SECTION 3

ANALYSIS METHOD

The changes in theory that arise due to the incorporation of an
out-of-plane shear capability in a generalized plane strain formula-
tion, which includes only a normal stress in the out-of-plane direc-
tion, are significant. In addition, there are far reaching conse-
quences in the finite element solution technique. The added stress
and strain components require revisions in the elastoplastic consti-
tutive equations. In addition, the special treatment of the compati-
bility of additional boundary conditions results in a special strain-
displacement relation. Implementing these changes into a finite
element analysis, although following classical developments, is
difficult. Use of the existing computer program [1] required its
thorough revision. In many cases, where before a plane stress state
was the only consideration, a stress tensor was involved in developing
suitable failure criteria, principal stress calculations, etc.

A complete description of each aforementioned consideration is
presented in the following subsections.

Generalized Plane Strain

Leknitskii [19] defines generalized plane strain in a very general
manner, which has been simplified for purposes of the present analysis.
This treatment allows displacements to occur in all three coordinate
directions, yet retains the advantages of the plane strain assumption.

Specifically, each displacement is dependent upon the x- and y-coordinate directions, and the displacement in the z-direction has an added linear dependence on the z-coordinate, which is considered the axial coordinate of a composite in the present analysis (Figure 1).
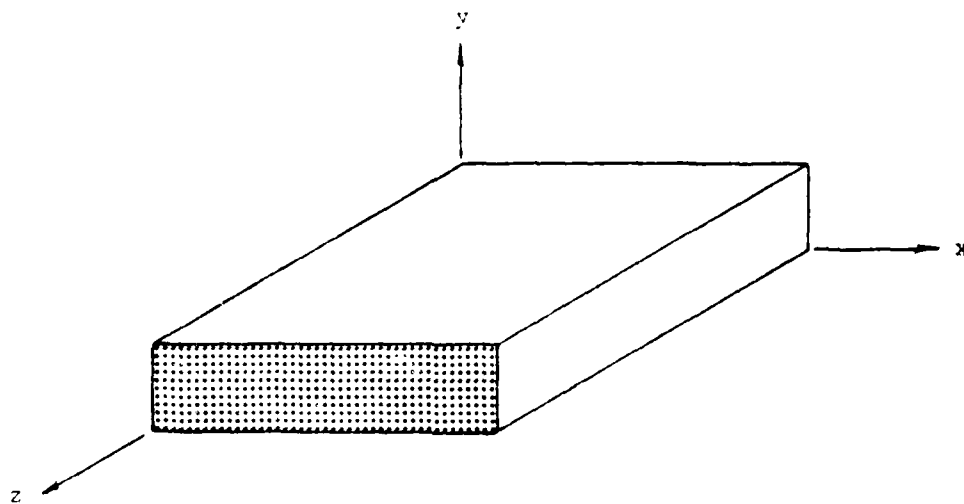
Figure 1. Fiber packing arrangement of a unidirectional composite.

The displacement functionals in equation form are:

$$u = u(x,y)$$
$$v = v(x,y) \tag{1}$$
$$w = w(x,y) + C_1 z$$

where

u represents the x-displacement

v represents the y-displacement

w represents the z-displacement

and C_1 is a yet unspecified constant.

Previous investigators [1] making use of the generalized plane strain assumption simplified the expression for the z-displacement by assuming it was dependent only on the axial coordinate position. Eliminating the functional dependence on the x- and y-coordinates essentially eliminated axial shear deformations, while allowing only constant axial normal displacements.

Including the x and y dependence of the z-displacement allows a special form of axial shear deformation corresponding to the generalized plane strain treatment. Expressions for strain can now be calculated for the continuum, and simplified according to Eqs. (1):

$$\varepsilon_x = \frac{\partial u}{\partial x} \qquad \gamma_{xy} = \frac{\partial u}{\partial y} + \frac{\partial v}{\partial x}$$

$$\varepsilon_y = \frac{\partial v}{\partial y} \qquad \gamma_{xz} = \frac{\partial w}{\partial x} + \cancel{\frac{\partial u}{\partial z}}^{0} \qquad (2)$$

$$\varepsilon_z = \frac{\partial w}{\partial z} \qquad \gamma_{yz} = \frac{\partial w}{\partial y} + \cancel{\frac{\partial v}{\partial z}}^{0}$$

where ε represents normal strain and γ represents engineering shear strain. These expressions govern the displacement of the continuum in question.

Constitutive Equations

The key element of the relationship between load and displacement of a continuum is the consititutive equation. Each constituent material of a composite has unique properties represented in its own constitutive equation. In the present analysis, the fiber material is considered to be isotropic and transversely isotropic in order to model fibers such as graphite, but can be reduced to a simple elastic,

isotropic material for the purpose of characterizing fibers such as boron and glass. The matrix material is considered to be isotropic and elastoplastic, the plastic response being modeled by the Prandtl-Reuss flow rule.

A constitutive equation involving only four stress and strain components has been derived in detail [1], but the two additional longitudinal shear components require additional consideration. As discussed by Baker and Foye [5], the two additional shear stress-shear strain equations are

$$
\begin{aligned}
\tau_{xz} &= G' \, \gamma_{xz} \\
\tau_{yz} &= G' \, \gamma_{yz}
\end{aligned}
\tag{3}
$$

where G' is the longitudinal shear modulus and τ represents shear stress. When Eqs. (3) are included in the complete set of constitutive equations for transversely isotropic elastic behavior, a material properties matrix [D] is generated as

$$
[D] = \frac{E}{Q}
\begin{bmatrix}
1 - \frac{E \nu'^2}{E'} & \nu + \frac{E \nu'^2}{E'} & 0 & 0 & 0 & (1 + \nu)\nu' \\
 & 1 - \frac{E \nu'^2}{E'} & 0 & 0 & 0 & (1 + \nu)\nu' \\
 & & \frac{Q}{2(1+\nu)} & 0 & 0 & 0 \\
 & & & \frac{E'Q}{2E(1+\nu')} & 0 & 0 \\
 & & & & \frac{E'Q}{2E(1+\nu')} & 0 \\
 \text{Symmetric} & & & & & 1 - \frac{E \nu'^2}{E'}
\end{bmatrix}
\tag{4}
$$

where

$$Q = (1 + \nu)(1 - \nu - \frac{2E\nu'^2}{E'})$$

ν = in-plane Poisson's ratio

ν' = major Poisson's ratio

E = transverse elastic modulus

E' = longitudinal elastic modulus

In obtaining Eq. (4), the relation $G = E/2(1 + \nu)$ has been utilized.
The constitutive equation for isotropic material behavior is well-known
and is merely a simplification of Eq. (4), where the longitudinal and
transverse moduli, and the Poisson's ratios, are equal:

$$[D] = \frac{E(1 - \nu)}{(1 + \nu)(1 - 2\nu)}
\begin{bmatrix}
1 & \frac{\nu}{1 - \nu} & 0 & 0 & 0 & \frac{\nu}{1 - \nu} \\
 & 1 & 0 & 0 & 0 & \frac{\nu}{1 - \nu} \\
 & & \frac{1 - 2\nu}{2(1 - \nu)} & 0 & 0 & 0 \\
 & & & \frac{1 - 2\nu}{2(1 - \nu)} & 0 & 0 \\
 & & & & \frac{1 - 2\nu}{2(1 - \nu)} & 0 \\
 & \text{Symmetric} & & & & 1
\end{bmatrix} \quad (5)$$

This Eq. (5) pertains to elastic, isotropic materials whether they are
fiber or matrix.

The constitutive equation must also represent elastoplastic materi-
al behavior in the matrix after yielding occurs. An octahedral shear
stress yield criterion is employed, and plastic strain is assumed to be
proportional to the deviatoric stress tensor, using the Prandtl-Reuss

flow rule. Reference [1] discusses sources of more information related
to these two criteria. A plane strain treatment of elastoplastic
behavior by Adams [11] is readily adapted to a generalized plane strain
treatment, as outlined briefly in Appendix A. The resulting constitu-
tive equation is

$$[D] = \begin{bmatrix} & & & & & & \end{bmatrix} \qquad (6)$$

the individual terms are described in Appendix A.

Finite Element Formulation

A major consideration in the finite element formulation is the
desire to have a combined loading capability, where any combination
of loads can be applied simultaneously. This leads to the seemingly
impossible task of applying separate and contradictory boundary con-
ditions simultaneously. Before these factors can be considered in
detail, the fundamental problem must first be set up.

The finite element model to be used in this investigation is
based on the assumption that the fibers are distributed in a square
array, as shown in Figure 1, although any rectangular array is entirely
possible. Previous investigators [1, 10, 20] have shown that there is

little loss of modeling accuracy due to this assumption. Considering
the behavior of a unidirectional composite with a relatively long axial
dimension, certain load symmetry and geometric symmetry assumptions can
be made, as described in Reference [4]. While there are four axes of
geometric symmetry for the unit cell (Figure 2a), only two can be used
due to load symmetry considerations. When considering that each load
is assumed to deform the unit cell in a uniform manner, load symmetry
about the x and y axes for all five stress components can be easily
seen. Only one quadrant of the unit cell (Figure 2b) need be con-
sidered to describe the behavior of the unit cell and of an entire
continuum of unit cells.

A detailed description of the boundary conditions is necessary,
beginning with the normal displacements. Due to the previously
mentioned constraints of the system, normal displacements of the
boundaries of the quadrant (Figure 2b) are restricted to those which
cause the boundary to displace only parallel to the original boundary.
This being explained in great detail elsewhere [1], attention will be
focused on the shear displacements. In the absence of longitudinal
shear loading, deformation in the z-direction is simply a constant,
uniform deformation of the entire frontal cross-section of the quadrant.
Shear deformations constrain only the loaded boundary to displace uni-
formly in the z-direction, while the opposite face remains stationary
in the z-direction. A τ_{yz} shear stress, for example, causes the face
at $y = b$ (see Figure 3) to move uniformly in the z-direction while the
face at $y = 0$ is fixed in the z-direction. Meanwhile, the faces at

a) Unit cell of the fiber arrangement

b) Quadrant to be analyzed
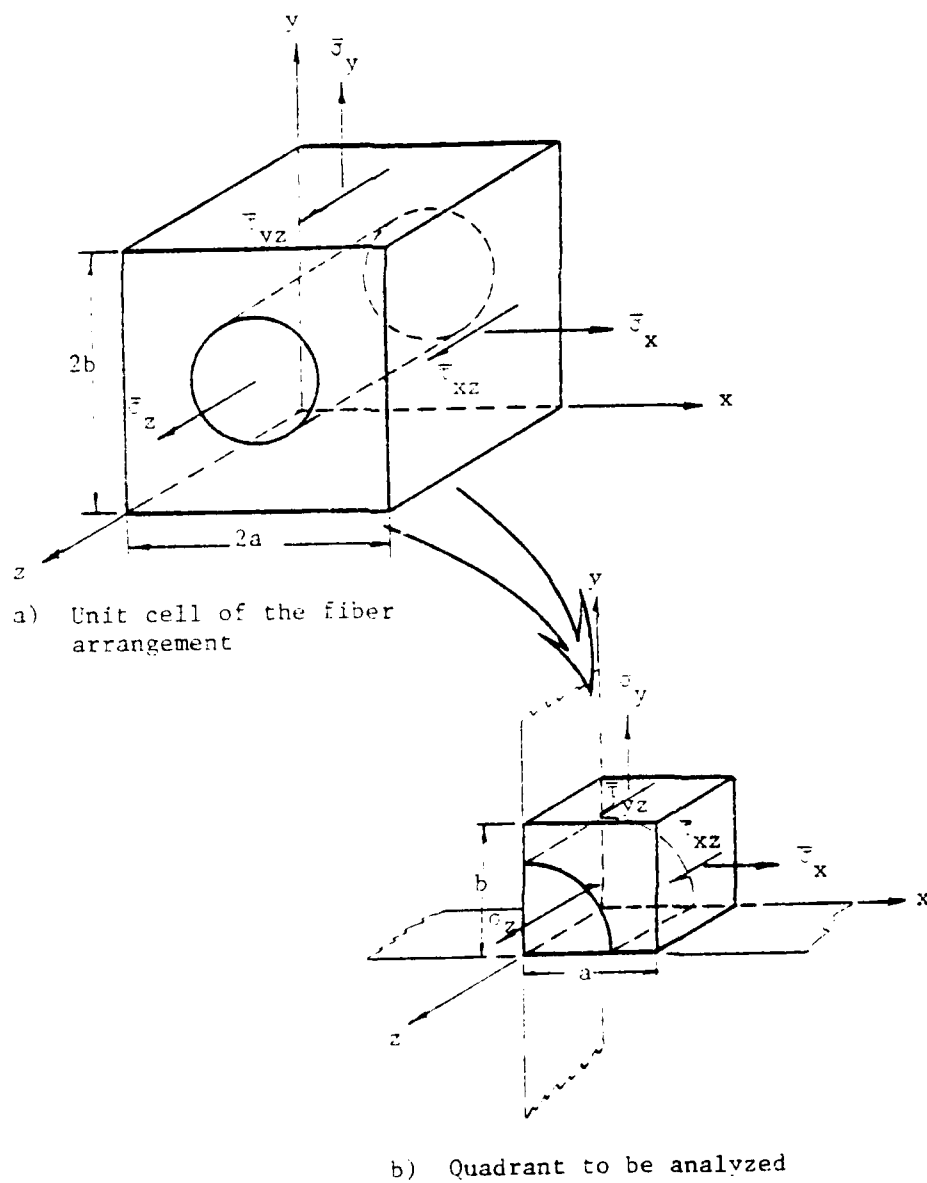
Figure 2. Symmetry simplification of the fiber arrangement.
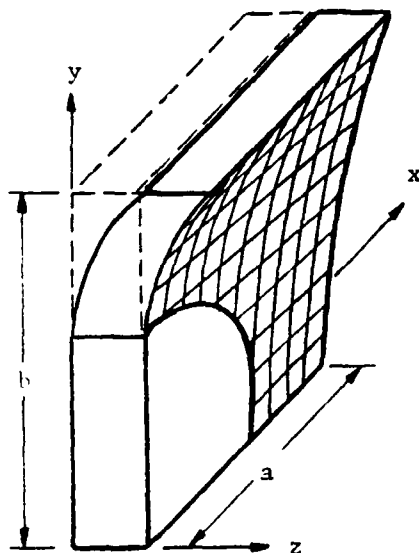
Figure 3. Shear deformation of the finite element model due to shear loading.

x = 0 and x = a are free to move in the z-direction as strains are induced. Similar treatment of the other longitudinal shear stress follows. It will be noted that these restrictions are not compatible, i.e., while the face at x = 0 is required to be fixed in one case, it is required to be free in the other case. To solve this anomaly, the analysis must be considered for the representative elements of the entire quadrant.

Constraints following those of Reference [2] are imposed on the special generalized plane strain deformation of the finite element continuum due to a τ_{yz} shear stress:

$$w = C \quad \text{along} \quad y = b$$
$$w = 0 \quad \text{along} \quad y = 0 \tag{7}$$
$$\frac{\partial w}{\partial x} = 0 \quad \text{along} \quad x = 0, \, x = a$$

Likewise for τxz loading:

$$w = C \quad \text{along } x = a$$

$$w = 0 \quad \text{along } x = 0 \tag{8}$$

$$\frac{\partial w}{\partial y} = 0 \quad \text{along } y = 0, \; y = b$$

where C represents a constant displacement. It will again be noted that the two shear boundary conditions cannot be applied to the same node simultaneously. A method of considering the two shear loads in separate problems while permitting combined shear loading is desired in the finite element formulation.

It is possible to apply the two shear boundary conditions separately by adjusting the elemental strain-displacement relation. The derivation of this relation for a regular treatment of generalized plane strain is outlined in Appendix B. The resulting Eq. (B-17) must be adapted to manage the shear boundary conditions separately. Since the boundary conditions are concerned with displacements, the shear displacements must be considered to be separate and unique entities at each node point rather than combined into a general z-displacement as in Eq. (B-17). Thus, a τ_{xz} shear stress induces a z-displacement w_{xz}, and a τ_{yz} shear stress induces a z-displacement w_{yz}. These separate displacements can be arbitrarily specified without affecting other boundary conditions if the strain-displacement matrix equation is expanded slightly as follows:

$$
\begin{Bmatrix} \varepsilon_x \\ \varepsilon_y \\ \gamma_{xy} \\ \gamma_{xz} \\ \gamma_{yz} \\ \varepsilon_z \end{Bmatrix}
= \frac{1}{2A}
\begin{bmatrix}
b_i & 0 & 0 & 0 & b_j & 0 & 0 & 0 & b_k & 0 & 0 & 0 & 0 \\
0 & c_i & 0 & 0 & 0 & c_j & 0 & 0 & 0 & c_k & 0 & 0 & 0 \\
c_i & b_i & 0 & 0 & c_j & b_j & 0 & 0 & c_k & b_k & 0 & 0 & 0 \\
0 & 0 & b_i & 0 & 0 & 0 & b_j & 0 & 0 & 0 & b_k & 0 & 0 \\
0 & 0 & 0 & c_i & 0 & 0 & 0 & c_j & 0 & 0 & 0 & c_k & 0 \\
0 & 0 & 0 & 0 & 0 & 0 & 0 & 0 & 0 & 0 & 0 & 0 & 2A
\end{bmatrix}
\begin{Bmatrix} u_i \\ v_i \\ wxz_i \\ wyz_i \\ u_j \\ v_j \\ wxz_j \\ wyz_j \\ u_k \\ v_k \\ wxz_k \\ wyz_k \\ w_n \end{Bmatrix}
\tag{9}
$$

where i, j, and k represent the three respective nodes of an element, and w_n represents the constant normal axial displacement.
It will be noted that the three extra columns in the matrix and the added zeros effectively prevent the longitudinal shear strains from influencing each other and the remainder of the strains. The added terms in the displacement vector will also be noted. Observing the expression for elemental shear strain γ_{yz} above, provides a check of the last boundary condition in Eq. (7) which is now inherent in the strain-displacement equation. The shear strain γ_{yz}, equal to $\frac{\partial w}{\partial y}$, is seen to depend only on the variables c_i, c_j and c_k, which are merely differences in the x-coordinates of the nodes of an element. Because the w_{xz} displacement is treated separately from the w_{yz} displacement, the expression for γ_{yz} does not include a $\gamma_{xz}\left(\frac{\partial w}{\partial x}\right)$ shear strain, and this is inherent in the expression. Therefore, this special boundary condition has been incorporated into the strain-displacement equation.

The remaining finite element formulation follows a three-dimensional formulation by Zienkiewicz [21], as shown in abbreviated form in the following equations:

$$[K]^e = \int_{vol} [B]^T [D][B] \; d(vol) \tag{10}$$

$$\{\delta\} = [K]^{-1}\{F\} \tag{11}$$

$$\{\epsilon\} = [B]\{\delta\} \tag{12}$$

$$\{\sigma\} = [D][B]\{\delta\} \tag{13}$$

where

$\{\delta\}$ = nodal displacements

$\{\epsilon\}$ = elemental strains

[B] = strain-displacement matrix

[D] = constitutive equation

$\{\sigma\}$ = elemental stresses

$[K]^e$ = elemental stiffness matrix

$\{F\}$ = nodal force vector

$[K]^{-1}$ = inverse of the global stiffness matrix.

Elemental stiffness matrices are developed in Eq. (10), which combined together for the entire model form a global stiffness matrix. This is inverted for use in Eq. (11), to solve for nodal displacements. Element strains and stresses are calculated from the displacement vector in Eqs. (12) and (13), respectively. Two differences from Zienkiewicz's formulation are the nodal force vector and, of course, the nodal displacement vector. The displacement vector was previously defined; the nodal force vector proves to be very similar, due to the fact that there are five force components and displacement components

possible at each node of the finite element grid. Because the solution technique involves the force vector to a large extent, it will be described in more detail next.

Solution Technique

A finite element analysis computer program developed by Miller and Adams [1] has been adapted for the modified form of generalized plane strain. The additional components of stress and strain result in the necessity of a thorough revision of the basic solution technique. The Branca technique [18] for applying loads and boundary conditions, and the specialized Gaussian elimination solution of the stiffness matrix, are the major burdens in the revision. Developing these new techniques revealed a more efficient procedure for storing the stiffness matrix. The solution technique involves the application of loads and boundary conditions, which is a logical starting point for the following description.

To describe the Branca technique [18], a small two-element model shown in Figure 4 will be considered. The applied loads shown are
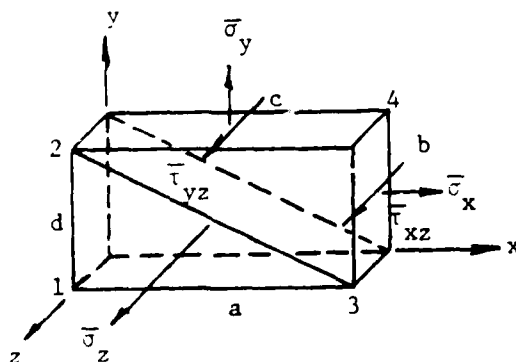
Figure 4. Simplified model for example solution technique.

actually applied as nodal forces, resulting in five separate loading

components possible at each node. As explained in detail by Miller

and Adams [1], the axial normal load is assumed to cause a constant

displacement in the z-direction at every node. The solution technique

for that z-displacement combines all the axial stiffness terms and

axial load terms into one, and one displacement term is solved for,

which represents the z-displacement of all node points. Therefore,

with the remaining four loads at each node, the resulting load vector

for the entire model is 17 terms long, as is the displacement vector

(see Eq. 14), (where F_{17} and δ_{17} represent the z-direction force and

displacement, respectively).

The global stiffness matrix is created from the elemental stiff-

ness matrices by means of classical techniques [21, 22], but the

application of boundary conditions to the global stiffness matrix is

necessary. Assume the model in Figure 4 to be loaded and constrained

in a manner similar to the total finite element grid. Before boundary

conditions are applied, the diagonalized stiffness matrix appears as

in Eq. (14). Each row of the original matrix governs the behavior of

a node due to a particular load. There are four rows for every node

in the finite element grid. In addition, the last row and column

represent behavior due to normal axial loads. It will be noted that

terms in a square stiffness matrix are arranged in regular rows and

columns, but upon diagonalization the columns are skewed upward to

the right. A row in a square stiffness matrix is represented differ-

ently in a diagonalized stiffness matrix; terms that were to the left

(14)

(15)

Boundary Condition
Columns

X Y XZ YZ Z

of the diagonal are now in the skewed column, while the remainder of
the row now begins in Column 1. A typical diagonalized row is
underlined in Eq. (14).

Table 1 shows the nodal constraints upon the model in Figure 4
necessary to mimic the behavior of a composite in a micromechanics
analysis. Effects upon the stiffness matrix due to a fixed node are
simple; the row of the stiffness matrix pertaining to the direction
of fixity of the node is zeroed except for the diagonal term, which
is given a value of one. It will be noted that part of a zeroed row
is skewed as described previously and is shown by the underlined terms
in Eq. (15). Upon solution, this causes a zero displacement to be
calculated at this node. When all the fixed constraints are invoked,
the stiffness matrix appears as in Eq. (15).

TABLE 1

NODAL CONSTRAINTS

Respective Load	Direction Of Constraint	Constrained Nodes	
		Fixed	Constant
τ_x	x	1,2	3,4
τ_y	y	1,3	2,4
τ_{xz}	z	1,2	3,4
τ_{yz}	z	1,3	2,4

The Branca technique [18] involves the constant displacement boundary conditions. It combines separate force-displacement equations within the matrix Eq. (15), that are affected by similar constant displacement boundary conditions. For example, the x-forces on Nodes 8 and 9, F_9 and F_{13} respectively (see Figure 6), can be combined into one total force. Displacements δ_9 and δ_{13} are set equal due to the constant displacement boundary conditions, which allows some combining of terms. A special equation results which sums the terms of the equation involving F_9 and the terms involving F_{13}. This equation now describes the x-direction behavior of side b of Figure 6. To incorporate the effects of each constant displacement boundary condition within the stiffness matrix, this same logic was developed into a pattern [18] to ease the development of the FEM ESA program. There are two steps in this pattern of applying boundary conditions, which will be called "columnizing" and "combining." Again consider Row 9, which represents the displacement of Node 9 in the x-direction due to an x-load. For a constant x-displacement on side b of the model, the two nodal displacements on that side (8 and 9) must be equal. Now the two respective rows must be combined such that there will be a combined stiffness term representing this constant displacement, and respective forces must be added together resulting in a combined force. Solving the combined stiffnesses and forces equation results in an average displacement on side b. The first step, "columnizing," involves adding the boundary condition row to another boundary condition column particularly set up for this particular equation. Row 9 shows the

Boundary Condition Columns

$$
\begin{array}{|c c c c c|}
 & X & Y & XZ & YZ & Z \\
\hline
0 & 0 & 0 & 0 & 0 \\
0 & 0 & 0 & 0 & 0 \\
0 & 0 & 0 & 0 & 0 \\
0 & 0 & 0 & 0 & 0 \\
0 & 0 & 0 & 0 & 0 \\
(K_{63} + K_{613}) & 0 & (K_{66} + K_{614}) & (K_{611} + K_{615}) & (K_{68} + K_{616}) & (K_{617}) \\
0 & 0 & 0 & 0 & 0 \\
(K_{89} + K_{813}) & 0 & (K_{68} + K_{814}) & (K_{811} + K_{815}) & (K_{88} + K_{816}) & (K_{817}) \\
(K_{99} + K_{913}) & 0 & (K_{69} + K_{914}) & (K_{911} + K_{915}) & (K_{89} + K_{916}) & (K_{917}) \\
0 & 0 & 0 & 0 & 0 \\
(K_{911} + K_{1113})(K_{611} + K_{1114})(K_{1111} + K_{1115})(K_{811} + K_{1116})(K_{1117}) \\
0 & 0 & 0 & 0 & 0 \\
(K_{913} + K_{1313})(K_{613} + K_{1314})(K_{1113} + K_{1315})(K_{813} + K_{1316})(K_{1317}) \\
(K_{914} + K_{1314})(K_{614} + K_{1414})(K_{1114} + K_{1415})(K_{814} + K_{1416})(K_{1417}) \\
(K_{915} + K_{1315})(K_{615} + K_{1415})(K_{1115} + K_{1515})(K_{815} + K_{1516})(K_{1517}) \\
(K_{916} + K_{1316})(K_{616} + K_{1416})(K_{1116} + K_{1615})(K_{816} + K_{1616})(K_{1617}) \\
(K_{917} + K_{1317})(K_{617} + K_{1417})(K_{1117} + K_{1715})(K_{817} + K_{1617})(K_{1717}) \\
\end{array}
$$

(16)

Effective Stiffness Area

five boundary condition columns enlarged, that were initially shown in Eq. (15). The new terms were created by columnizing, for example; Rows 9 and 13 of Eq. (15), representing the x-direction stiffnesses of Node 3, are now stored in the X Column of Eq. (16). The previous positions of the terms that were just relocated must be eliminated since their effects have been taken into account in the boundary condition columns: setting diagonal terms equal to one and the remaining terms in question equal to zero, eliminates their contribution. Because boundary conditions were involved in each direction on each node, in this case, the regular stiffness matrix is totally eliminated when its terms are combined into the boundary condition columns, as seen to the right of the vertical dashed line (Eq. 16).

The second step is shown by arrows in Eq. (16), representing the combination of boundary condition rows, located within the special boundary condition column area, into the final effective stiffness area (Eq. 17). These manipulations to include the two additional shear boundary conditions being considered follow closely the technique used in References [18] and [1]. For example, each term of Row 6 in Eq. (16), (representing y-direction stiffness) is added to its respective column in Row 14 (as shown by the respective arrow). Eq. (17) shows the resulting terms of the summation due to the combining operation. Final manipulations of the effective stiffness area are employed to simplify the Gaussian elimination. Since Eq. (17) is symmetric, the redundant terms can be eliminated (see Eq. 18). Also, the new diagonal terms are positioned in Column 1, consistent with the previous diagonalized form.

Effectiveness Stiffness Area

	X	Y	XZ	YZ	Z
X	$K_{99} + 2K_{913}$ $+ K_{1313}$	$K_{69} + K_{914}$ $+ K_{613} + K_{1314}$	$K_{911} + K_{915}$ $+ K_{1113} + K_{1315}$	$K_{89} + K_{916}$ $+ K_{813} + K_{1316}$	$K_{917} + K_{1317}$
Y	$K_{69} + K_{613}$ $+ K_{414} + K_{1314}$	$K_{66} + K_{1313}$ $+ 2K_{614}$	$K_{611} + K_{615}$ $+ K_{1114} + K_{1415}$	$K_{68} + K_{616}$ $+ K_{814} + K_{1416}$	$K_{617} + K_{1417}$
XZ	$K_{911} + K_{1113}$ $+ K_{915} + K_{1315}$	$K_{611} + K_{1114}$ $+ K_{615} + K_{1514}$	$K_{1111} + K_{1515}$ $+ 2K_{1115}$	$K_{811} + K_{1116}$ $+ K_{815} + K_{1516}$	$K_{1117} + K_{1517}$
YZ	$K_{89} + K_{813}$ $+ K_{916} + K_{1316}$	$K_{68} + K_{814}$ $+ K_{616} + K_{1416}$	$K_{811} + K_{815}$ $+ K_{1116} + K_{1615}$	$K_{88} + K_{1616}$ $+ 2K_{816}$	$K_{817} + K_{1617}$
Z	$K_{917} + K_{1317}$	$K_{617} + K_{1714}$	$K_{1117} + K_{1715}$	$K_{817} + K_{1617}$	K_{1717}

$$(17)$$

$$
\begin{Bmatrix} F_x \\ F_y \\ F_{xz} \\ F_{yz} \\ F_z \end{Bmatrix}
=
\begin{bmatrix}
K_{11} & \cdots & K_{13} & K_{14} & K_{15} \\
K_{22} & \cdots & 0 & K_{24} & K_{25} \\
K_{33} & \cdots & 0 & 0 & K_{35} \\
K_{44} & \cdots & 0 & 0 & 0 \\
K_{55} & \cdots & 0 & 0 & 0
\end{bmatrix}
\begin{Bmatrix} \delta_x \\ \delta_y \\ \delta_{xz} \\ \delta_{yz} \\ \delta_z \end{Bmatrix}
$$

$$(18)$$

The size of the stiffness matrix evident in Eq. (14) becomes enormous when dealing with large finite element models. This stiffness matrix uses by far the majority of computer memory necessary, and decreasing its size also reduces the computer time needed to solve it. One way to decrease the size of the stiffness matrix is evident in Eq. (18), where the large stiffness matrix was reduced to a system of five equations. This method eliminates the rows and columns of the stiffness matrix where boundary conditions are involved. These eliminations take place as the stiffness matrix is being assembled. The amount of the reduction possible depends entirely on the number of boundary conditions invoked, but the advantage is significant for the types of finite element grids employed in this investigation, and doesn't reduce accuracy. It should be noted that this method of eliminating rows and columns was also utilized by Branca [18].

Next, general applied loads are input to Eq. (18) and overall displacements are solved for. The resulting displacements are those of the boundary nodes, which are then substituted back into the original displacement vector (shown in Eq. 14). The elemental strains and stresses can then be calculated.

The special stiffness formulation discussed above caused complexities in the Gaussian elimination procedure. Branca [18] who first developed the special Gaussian elimination scheme, also testified that it required intricate bookkeeping. Bookkeeping complexities are compounded in the present analysis due to the added boundary conditions, but the theory upon which Gaussian elimination is based remains

unchanged. Thus the Gaussian elimination procedure degenerates into an involved exercise in bookkeeping and programming.

Computer Implementation

Implementing the preceding theory into the FORTRAN computer program of Reference [1] results in the new generalized plane strain, finite element micromechanics analysis described in the flowchart in Appendix C. The incremental procedure utilized by Miller and Adams [1] remains intact in the present analysis except for the calculation of octahedral shear stress, which now includes the two added shear stress terms. This tangent modulus method enables highly inelastic materials to be managed easily.

In developing the analysis, another consideration was found to be essential for an efficient computer program. Designing the finite element mesh efficiently has a profound effect on the size of the stiffness matrix. The highest difference in node numbers in any one element determines the bandwidth of the stiffness matrix, i.e.,

$$BW = (R + 1)4 + 5 \tag{19}$$

where

BW = bandwidth of stiffness matrix

R = highest node number difference

The addition of 5 is due to the special boundary condition columns. The finite element mesh, besides the requirement to have a fine mesh in areas of high stress gradients, is also required to have a minimum R value. Additionally, due to the loading technique, the highest node number is also required to be located at the upper right-hand corner

of the mesh. A model was developed as shown in Figure 5 that fulfilled
these requirements, by arranging node points in rows and columns
(although obscure), and numbering the nodes one row at a time in
successive columns. There are 13 rows and 13 columns resulting in
169 nodes and 288 elements. The resulting R value is 14, making the
bandwidth 65, as calculated from Eq. (19).

In a typical program run, utilizing the finite element model of
Figure 5, the stiffness matrix alone requires 37,180 words (60 bits
per word) of central memory on the CDC Cyber 760 computer system. This
amount is over 40 percent of the entire central memory necessary, which
is approximately 90,000 words. An average time used by the central
processor to run the program for each increment is 5.57 seconds. This
value varies between 5 seconds and 8 seconds per increment, depending
on the number of increments, for the applications in this investigation
and most investigations.

Increment sizes should be under 500 psi for in-plane normal
stresses and longitudinal shear stresses, while axial normal stresses
should be about 1000 psi or under for typical fibers of high stiffness
(glass or graphite). During highly inelastic behavior, increments
should be decreased accordingly to values on the order of 100 psi.

Failure Theories

There are three failure theories necessary for a comprehensive
prediction of failure in the present micromechanics analysis. An
octahedral shear stress criterion is used to define failure of the
matrix. This is a measure of the distortional energy stored in the
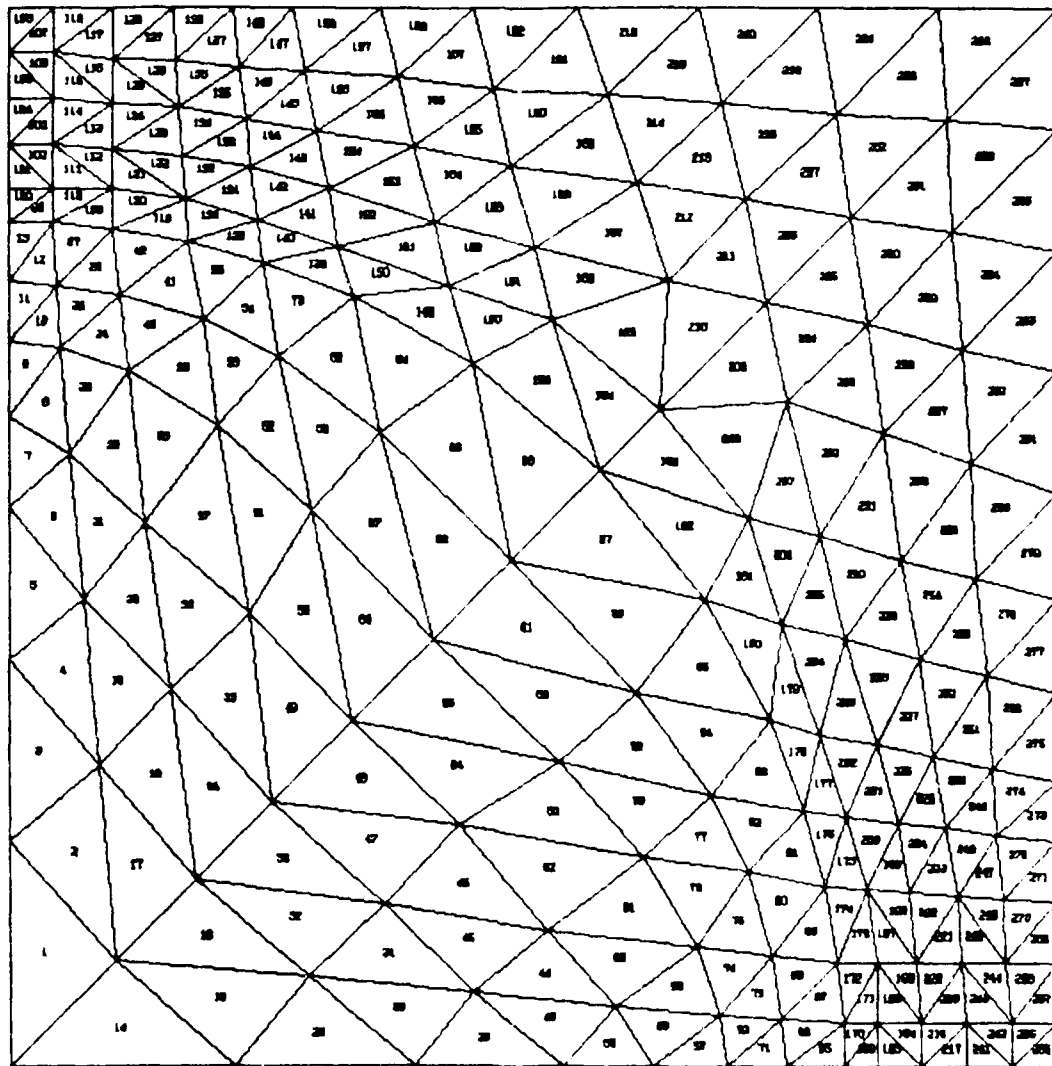
FINITE ELEMENT MESH

Figure 5.   Typical finite element model of quadrant to be analyzed.

matrix. The limitation of this criterion is that it is not suitable for a hydrostatic load, since there is no distortional component present in hydrostatic loading. Therefore, a hydrostatic criterion is also invoked by testing for a hydrostatic stress state higher than the ultimate value.

In prior analyses [1] the fiber was tested for failure by a simple maximum stress criterion. Since only three normal stresses existed, a more complicated criterion was not needed. Because shear stresses also exist in the present analysis, a new criterion must be invoked. The fact that graphite is an orthotropic (transversely iso-tropic) material increases the complexity of the problem. A criterion specifically designed for orthotropic materials, and which considers the entire stress tensor, is the Tsai-Wu [23] failure criterion. Experimental results show that the Tsai-Wu criterion predicts failure far better than a maximum stress or maximum strain criterion [24]. The Tsai-Wu tensor form is also of a more general character than the Tsai-Hill criterion [24]. The only awkward characteristic of the Tsai-Wu criterion is the P_{12} term. This has been discussed widely in the literature, but Narayanswami and Adelman [25] show that neglecting this term rarely causes an error greater than 10 percent. This is the so-called "Modified Tsai-Wu" failure criterion. Assuming tensile and compressive allowable stresses to be equal, the form of the equation becomes:

$$P_1\sigma_1 + P_2\sigma_2 + P_3\sigma_3 + P_4\sigma_4 + P_5\sigma_5 + P_6\sigma_6$$
$$+ F_{11}\sigma_1^2 + P_{22}\sigma_2^2 + P_{33}\sigma_3^2 + P_{44}\sigma_4^2 + P_{55}\sigma_5^2 + P_{66}\sigma_6^2 = 1 \tag{20}$$

where σ represents the actual stress components, and the P terms

represent stress allowables as defined by Tsai and Wu [23].

SECTION 4

CONSTITUENT MATERIAL PROPERTIES

The matrix system used for experimental verification pur⌐oses in
the present investigation was Hercules 3501-6 epoxy resin [26]. Because
longitudinal shear loading is a major consideration in the present
study, it is appropriate to employ matrix constituent material proper-
ties derived from longitudinal shear experimental data. Solid rod
torsion test shear data were available for this matrix material [27].
This test has been shown to be a viable means of determining shear
moduli and shear strengths [28]. Each test specimen was approximately
4 inches long, with a diameter of $\frac{1}{4}$ inch, fabricated in a mold similar
to those shown in Reference [28]. These tests were performed on dry
specimens and specimens saturated with moisture, at three temperature
conditions, viz., $21^{o}C$ (room temperature) $100^{o}C$, and $160^{o}C$.

Data from either shear tests or tensile tests can be readily con-
verted to octahedral shear stress-octahedral shear strain expressions
for input to the analysis [29]. Previous investigators [30] had already
calculated the octahedral shear stress-octahedral shear strain behavior
of the epoxy matrix using uniaxial tensile test data, as indicated in
Figure 6. Similar results reduced from solid rod torsion test data by
the present investigator are shown in Figure 7. The tensile test speci-
mens were of a "dog-bone" configuration; approximate dimensions were
1/10 inch thick, $\frac{1}{2}$ inch width, $2\frac{1}{2}$ inch gage length, and 5 inch overall

34
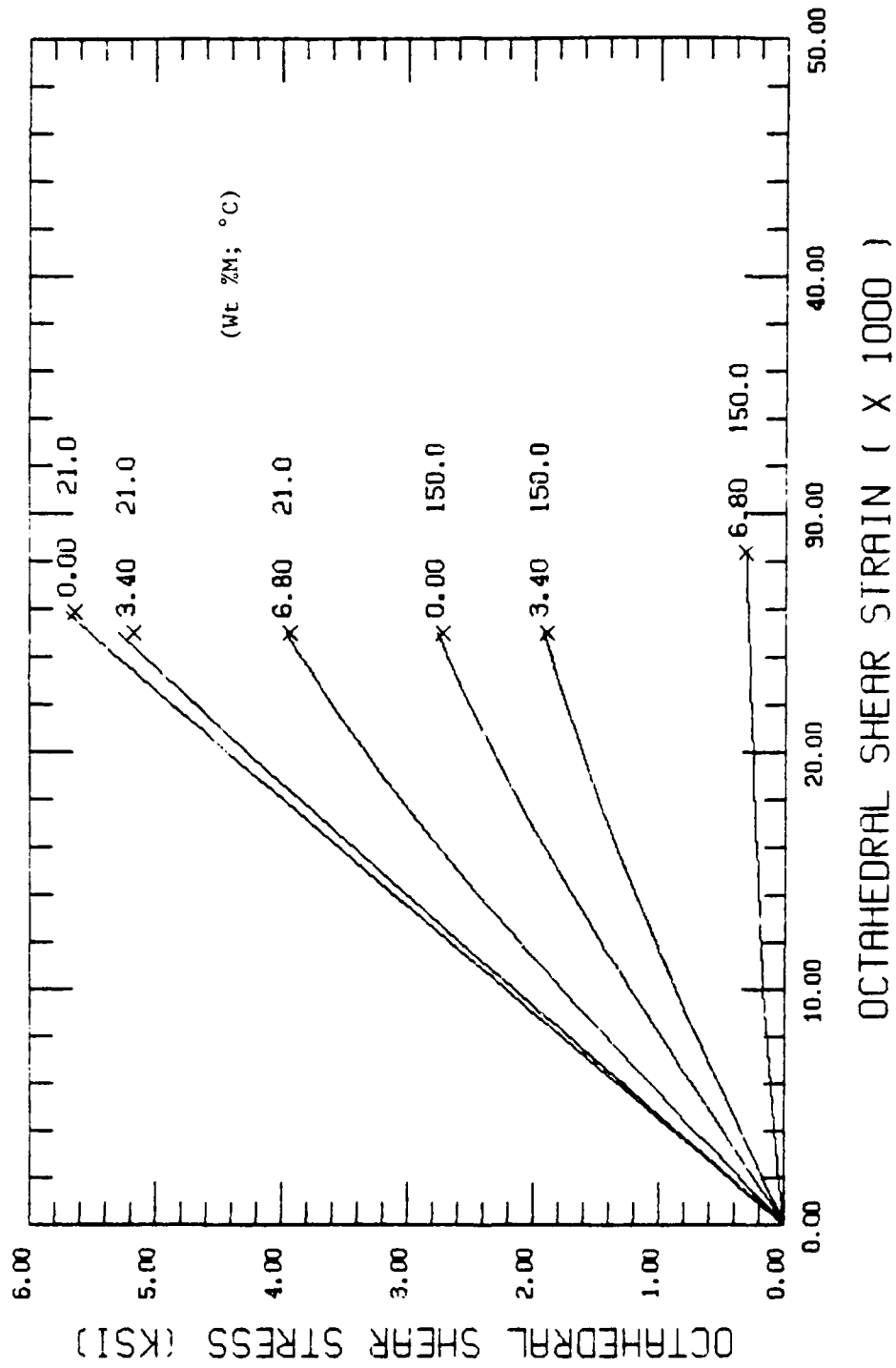
Figure 6. Hercules 3501-6 epoxy matrix octahedral shear stress-strain curves as generated from uniaxial tensile tests.

OCTAHEDRAL SHEAR STRAIN (X 1000)

OCTAHEDRAL SHEAR STRESS (KSI)

14.00

12.00

10.00

8.00

6.00

4.00

2.00

0.00

0.00   50.00   100.00   150.00   200.00   250.00   300.00

(Wt %M; °C)

0.0   21.0
3.4   21.0
6.8   21.0

0.0   100.0
3.4   100.0
6.8   100.0

0.0   160.0
3.4   160.0
6.8   160.0
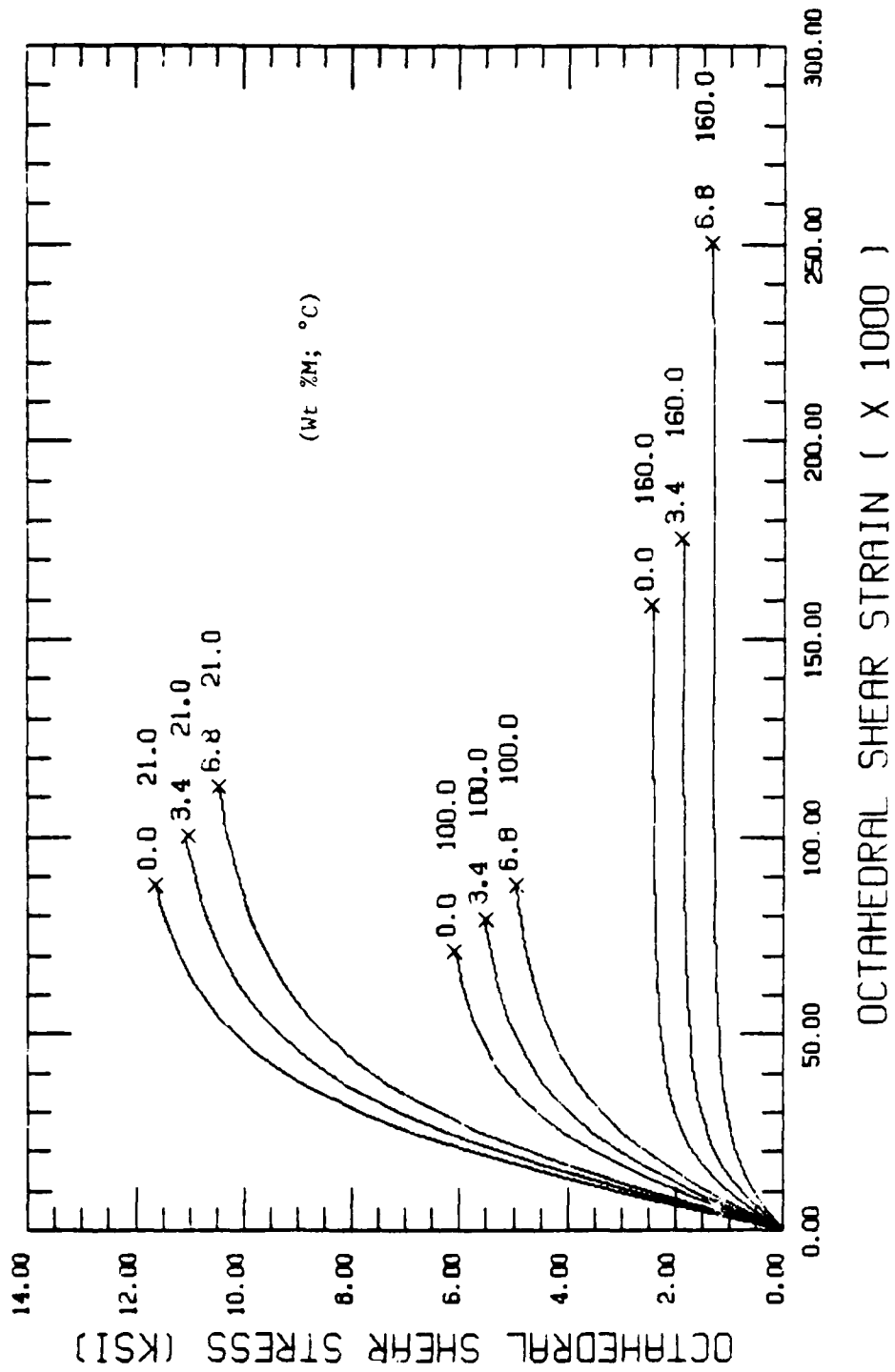
Figure 7. Hercules 3501-6 epoxy matrix octahedral shear stress-strain curves
as generated from solid rod torsion tests.

length. To use either of these sets of data in the micromechanics computer program, they must be expressed in equation form, with temperature and moisture as independent variables. First, a curve-fitting method, developed by Richard and Blacklock [31], was used to fit each data curve (at each test condition). This method defines each curve in terms of an initial slope, an asymptotic stress value, and a radius of curvature that connects these two values. The general form of the Richard-Blacklock equation for stress is:

$$\sigma = \frac{E \varepsilon}{\left[1 + \left| \frac{E \varepsilon}{\sigma_0} \right|^n \right]^{1/n}} \tag{21}$$

where

E = initial slope of stress-strain

σ_0 = the asymptotic stress value

n = inverse of the radius of curvature

ε = strain

Each constant (E, σ_0 and n) from each test condition, and values for ultimate stress, are then used in another curve-fit relation which expresses each value by an equation dependent upon temperature and moisture. It is a second-order, least-squares development resulting in an equation with six constants. For example, the initial slope would be expressed as:

$$E = C_1 T^2 + C_2 M^2 + C_3 MT + C_4 M + C_5 T + C_6 \tag{22}$$

where

T = Temperature (°C)

M = Percent moisture by weight

Resulting expressions for σ_o, E, n and ultimate stress are defined by the constants listed in Table 2.

TABLE 2

EXPERIMENTALLY-DETERMINED CONSTANTS FOR TEMPERATURE- AND
MOISTURE-DEPENDENT OCTAHEDRAL SHEAR STRESS-OCTAHEDRAL
SHEAR STRAIN CURVES AS OBTAINED FROM SOLID ROD TORSION
TEST DATA FOR HERCULES 3501-6 EPOXY RESIN

Values Dependent on T and M	CONSTANTS					
	c_1	c_2	c_3	c_4	c_5	c_6
E (lb/in²)	-4.464×10^{-2}	4.205×10^{-4}	6.098	-8.510×10^{3}	-1.434×10^{3}	3.430×10^{5}
σ_o (lb/in²)	3.423×10^{-2}	0	1.299×10^{-1}	1.847×10^{2}	-7.767×10^{1}	1.401×10^{4}
n (in⁻¹)	-1.190×10^{-6}	0	0	-3.699×10^{-2}	-1.357×10^{-3}	2.348
σ_u (lb/in²)	6.515×10^{-2}	2.773×10^{-1}	8.478×10^{-2}	-1.776×10^{2}	-7.301×10^{1}	1.322×10^{4}

Incorporating these equations directly into the computer program enables the calculation of tangent modulus values for each load increment, as needed for the inelastic material properties matrix defined in Section 3. The ultimate octahedral shear stress is also calculated for use in the octahedral shear stress failure criterion, also discussed in Section 3.

Comparing the octahedral shear stress-octahedral shear strain curves generated from tensile and from shear test data, Figures 6 and 7, respectively, the shear test data show modulus values slightly higher, but close enough to attest to the general accuracy of the experimental data. Another observation is the significant extent of inelastic behavior of the epoxy resin when subjected to shear test conditions, (Figure 7) in contrast to the limited plastic response exhibited by the uniaxial tensile data. A possible reason for this difference is the unique effect of flaws in each type of specimen. The thin, "dog-bone", tensile specimen is more susceptible to stress concentrations due to flaws such as voids or microcracks than the shear specimen. That is, the shear specimen is more stable in the presence of flaws because only the material on the surface of the rod is highly stressed. This surface is smooth and has a low number of flaws because the specimen is fabricated in a carefully polished steel mold. Internal flaws in the rod specimens have a reduced influence compared to those in the tensile specimens, which are subjected to a uniformly high stress throughout their volume.

Another factor possibly contributing to the difference is the accuracy of the test conditions, i.e., the accuracy and uniformity of test temperature and moisture conditions which were maintained. In both cases, moisture-conditioned specimens were actually tested in a dry environment, which tended to drive out the surface moisture, especially at the high test temperatures. The stress induced in the tensile specimens due to this moisture gradient probably affected the

modulus and strength much more than in the thicker shear specimens.
Also, the use of "clam-shell" heaters for elevated temperature tests
was a possible source of error in both test cases because of the po-
tential nonuniformity of temperature around the test specimen, and the
difficulty in accurately controlling the temperature in such a setup.

It is difficult to attribute the differences in behavior between
the tensile and shear specimens to experimental error alone, however,
and at this point it is impossible to use one form of the data to refute
the other. Unfortunately, there are no other published shear data
available that could provide insight to the problem. However, there are
some tensile data available that require a review.

The tensile data for the Hercules 3501-6 epoxy resin discussed by
Browning [32] show some important similarities to the shear data shown
in Figure 7. His data show a transition temperature above which
material properties are degraded greatly; this is particularly signifi-
cant at high moisture contents. This transition is a change from a
"glassy" solid behavior (high modulus), to a "rubbery" material behavior
(low modulus), as temperature increases. The present shear data (Figure
7) also suggest a transition temperature over the entire range of
moistures. For example, the zero moisture results can be observed as a
function of increasing temperature. At 100°C, the ultimate octahedral
shear stress has decreased as has the ultimate octahedral shear strain.
But, as temperature is increased further, ultimate strain increases
dramatically, as ultimate stress continues to decrease. A similar re-
sponse is observed for the high condition as temperature increases.

Up to the transition temperature, a slight decrease in ultimate strain takes place as the ultimate stress drops to nearly half the room temperature value. Temperature has a softening effect (lowering the modulus), while lowering the strength, but the material still has a "glassy" behavior, as seen in the decreasing ultimate strain.

When there is no moisture present, low temperature ultimate stresses and ultimate strains from the shear data are much higher than from Browning's data [32]. At the high temperature of $160^{\circ}C$, the shear data ultimate stress prediction dips below Browning's prediction, but the ultimate strain prediction is nearly five times higher than Browning's.

When moisture is added, the trend in ultimate stresses and strains in the shear test data and Browning's data are similar. Both sets of data show the plasticizing effect of high temperature and moisture.

Overall, the present solid rod shear data show much more pronounced inelastic behavior at all conditions than the tensile data of Browning. This leads to higher ultimate stress and strain predictions.

When comparing the octahedral shear curves of Figure 6, generated from tensile test data [30] by the present investigator, to Browning's results, modulus values are seen to be only slightly higher. Again at high temperature and moisture conditions, the present tensile data show lower moduli values, and lower ultimate stress and strain values. The presence of a glass transition is only hinted at in the present data, by the slight increase in ultimate strain when temperature is increased from room temperature to $150^{\circ}C$ at the saturated moisture condition.

Overall, the highly elastic and low ultimate strain behavior of the
tensile data follows Browning's tensile data more closely than the
shear data do. This is as ecpected since the data resulted from
similar tensile test methods.

Based upon the above comparisons, the shear data of Figure 7
appear to be reasonable, but they are enough unlike the tensile data
of Figure 6 and Browning's results [32] to require more experimental
evidence. More precise and comprehensive shear data for temperature
and moisture variations need to be generated, while considering the
molecular structure and chemistry involved in the resin system.

Fiber properties were mainly obtained from Hercules [33] and
Owens-Corning [34] literature, for the AS-graphite fiber and the S2-
glass fiber, respectively. Shear moduli and shear stress allowables
necessary for stiffness calculations and the fiber failure criterion
were easily found for the S2-glass (assumed isotropic). For the graph-
ite fiber, in-plane and longitudinal shear tests required to determine
these properties are not commonly performed on a fiber, due to its
small diameter. Instead, a shear modulus value was calculated in the
transverse plane of symmetry from the respective values of Young's
modulus and Poisson's ratio. It was necessary to estimate values of
longitudinal shear modulus and longitudinal shear ultimate stress from
data for other similar graphite fibers [35]. The values were 5.0 Msi
and 225 ksi respectively, as shown in Table 3. The transverse shear
stress being relatively unimportant because of the inability of the
analysis to directly apply transverse shear loads, a value of 25 ksi

transverse shear allowable was chosen. Microscopically the graphite
fiber is much like a composite due to the longitudinally arranged
graphite crystal structure. Thus, a low transverse allowable shear
stress is a viable approximation.

Properties of the constituent materials are presented in Table 3,
with estimated values denoted by an asterisk (*). Two sets of epoxy
matrix material properties at room temperature, dry conditions are
also shown, generated from tensile and shear experimental data (Figures
6 and 7).

TABLE 3

CONSTITUENT MATERIAL PROPERTIES FOR AS-GRAPHITE FIBER,
S2-GLASS FIBER, AND 3501-6 EPOXY RESIN

PROPERTY	Hercules AS-Graphite Fiber [23]	Owens-Corning S2-Glass Fiber [24]	Hercules 3501-6 Epoxy Matrix (Room Temperature, Dry) (from Tensile Test Data [26])	(from Shear Test Data [27])
Longitudinal Modulus, E_1 (Msi)	32.0	12.5	0.62	0.84
Transverse Modulus, E_2 (Msi)	2.0	12.5	0.62	0.84
Longitudinal Shear Modulus, G_{12} (Msi)	5.0*	5.2	0.23	0.31
Transverse Shear Modulus, G_{23} (Msi)	0.90	5.2	0.23	0.31
Major Poisson's Ratio, ν_{12}	0.20	0.22	0.34	0.34*
In-Plane Poisson's Ratio, ν_{23}	0.25	0.22	0.34	0.34*
Longitudinal Tensile Strength (ksi)	450.0	700.0	12.0	24.6
Transverse Tensile Strength (ksi)	50.0*	700.0	12.0	24.6
Longitudinal Shear Strength (ksi)	225.0	150.0*	5.0	12.3
Transverse Shear Strength (ksi)	25.0	150.0*	5.1	12.3
Longitudinal Coefficient of Thermal Expansion ($\times 10^{-6}$ in/in)	-0.36	5.0	40.0	40.0
Transverse Coefficient of Thermal Expansion ($\times 10^{-6}$ in/in)	9.7	5.0	40.0	40.0
Coefficient of Moisture Expansion	0	0	2.0	2.0

*Estimated

SECTION 5

NUMERICAL RESULTS

Test cases analyzed using the longitudinal shear loading version of the generalized plan strain micromechanics program indicate that the new analysis performs all of the same operations as the old version, with the addition of a shear loading capability. As theory predicts, there is no coupling between shear and normal loads during elastic load increments, but during increments beyond the elastic limit the Prandtl-Reuss flow rule is in effect and coupling does occur. When the deviatoric stress tensor is non-zero (during inelastic increments), the Prandtl-Reuss flow rule causes each elemental stiffness matrix to become fully populated. This in turn forces each stress term to be dependent on each strain term. Thus, a shear stress can then induce a small normal strain, which is impossible in elasticity theory, but entirely possible in plasticity theory. In fact, all stress components have an effect on all strain components if the deviatoric stress tensor is fully populated. Looking back to Eq. (6), it can be seen that the inelastic constitutive equation governs the coupling. The additional strain induced during inelastic increments is due to the two deviatoric stress terms within each term of that constitutive equation. This effect is small, but significant enough to warrant its inclusion. This inelastic strain contribution has been observed to be up to 6 percent of the total strain. To demonstrate that the longitudinal version of the micromechanics analysis provides

accurate and useful results, two types of examples have been devised. The first uses the constituent material properties to predict results using longitudinal shear loading analysis which are then compared to actual solid rod torsional shear data, for two different composite materials. The second example predicts laminate behavior using the longitudinal shear loading analysis in conjunction with a laminate point stress analysis.

Comparisons of Analytical Predictions with Solid Rod   rsion Test Data

Solid rod shear data had been generated [27] fo   mposite spec-imens as well as for the previously discussed solid rod torsion tests of the epoxy matrix. Fibers used in the composite specimens were the Hercules AS-graphite fiber [33] and the Owens-C .ning ?-glass fiber [34]. Hercules 3501-6 epoxy resin was used as the matrix system. These composites will henceforth be referred to as GR/EP and GL/EP, respectively, for the graphite and glass fiber composites.

Using the properties evaluated from the previously discussed solid rod torsion tests of the matrix system alone (Section 4), the micromechanics analysis predicted the composite shear stress-shear strain behavior. Because composite tests of GR/EP and GL/EP were performed in the same program as the matrix solid rod torsion tests, they provided the logical source of data comparision. These comparisions are shown in Figures 8 through 12 for GR/EP, and Figures 13 through 17 for GL/EP. Tests were performed at room temperature, 100°C, 160°C, at two moisture conditions, i.e., dry and fully saturated (6.75 percent moisture by weight). Although data were also available

45

SHEAR STRAIN (X 1000)
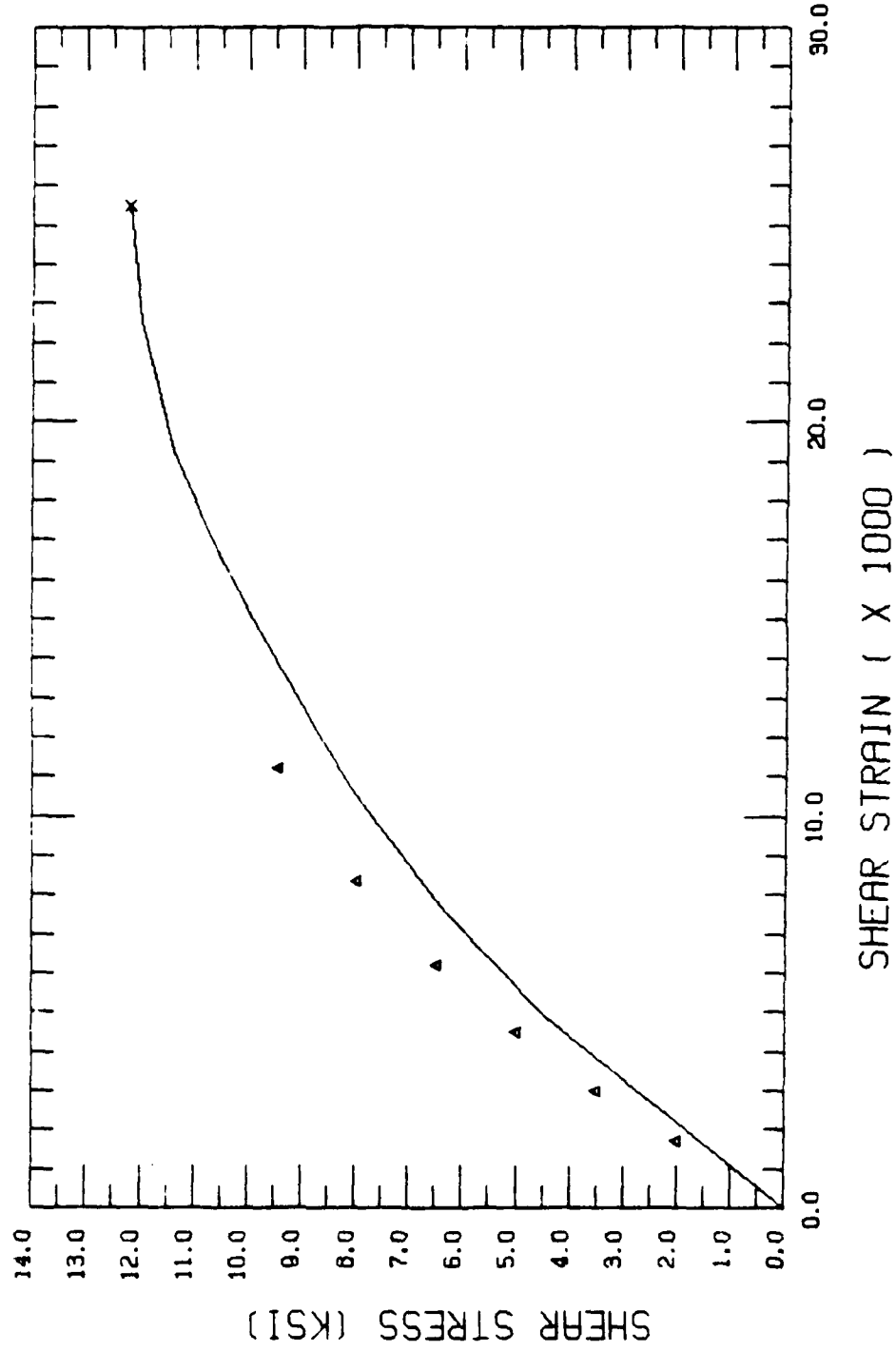
SHEAR STRESS (KSI)

Figure 8.   Shear stress-shear strain curves for graphite/epoxy at room temperature, dry conditions, comparing micromechanics predictions (shown in triangles) with solid rod torsion test data (shown in solid line).

SHEAR STRAIN (X 1000)
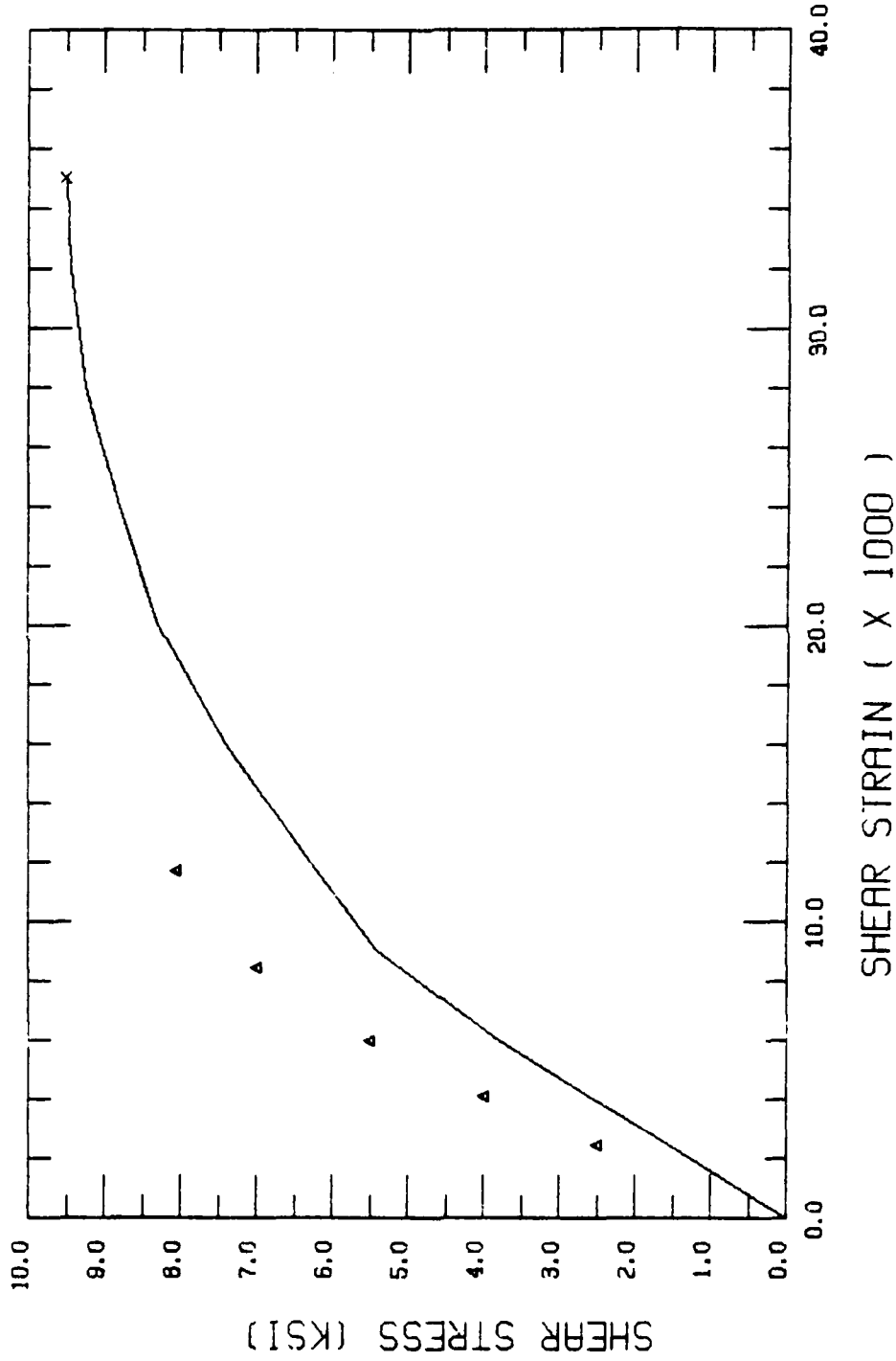
SHEAR STRESS (KSI)

Figure 9. Shear stress-shear strain curves for graphite/epoxy at room temperature, saturated (6.75%M by weight) conditions, comparing micromechanics predictions (shown in triangles) with solid rod torsion test data (shown in solid line).

47
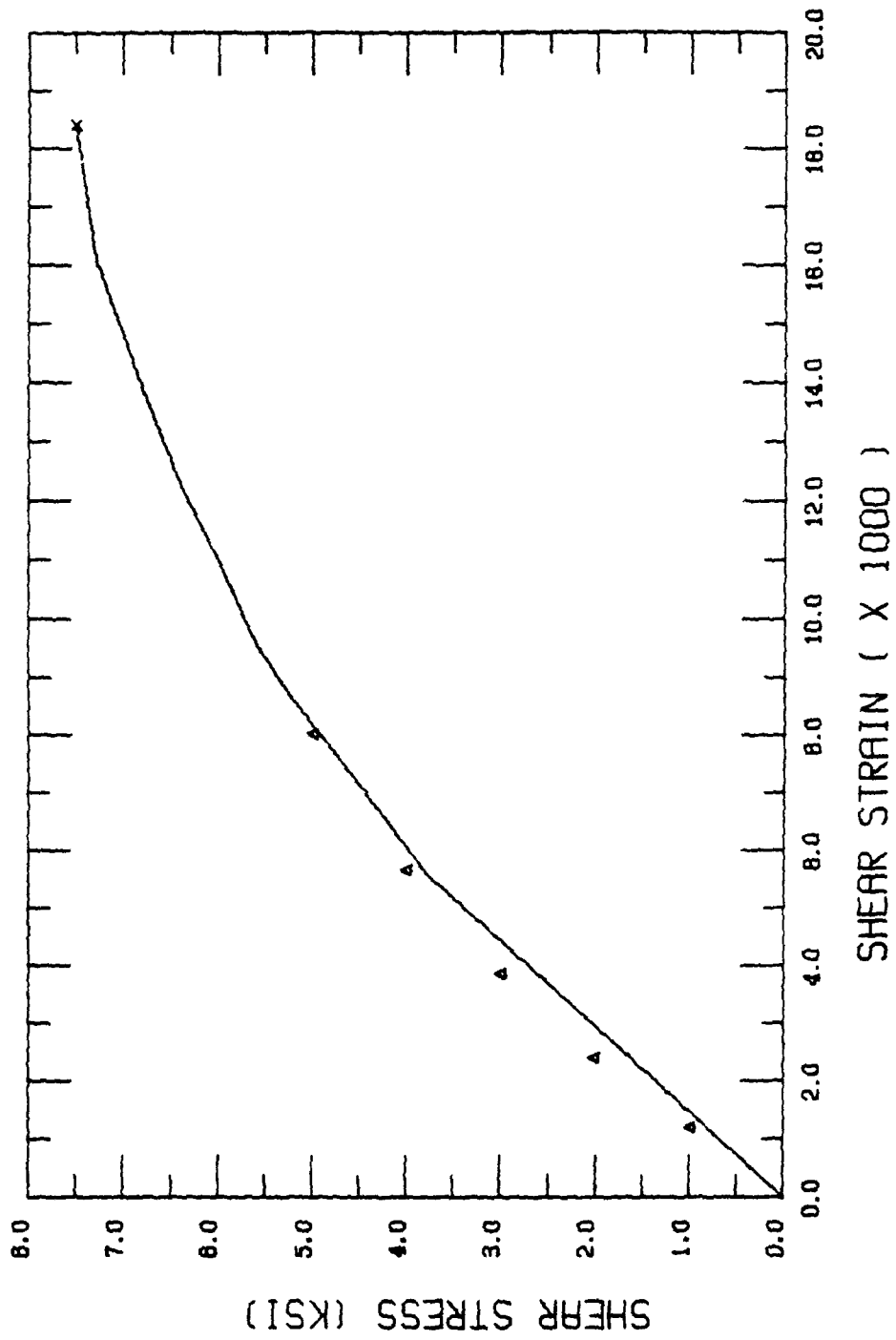
Figure 10. Shear stress-shear strain curves for graphite/epoxy at 100°C, dry conditions, comparing micromechanics predictions (shown in triangles) with solid rod torsion test data (shown in solid line)
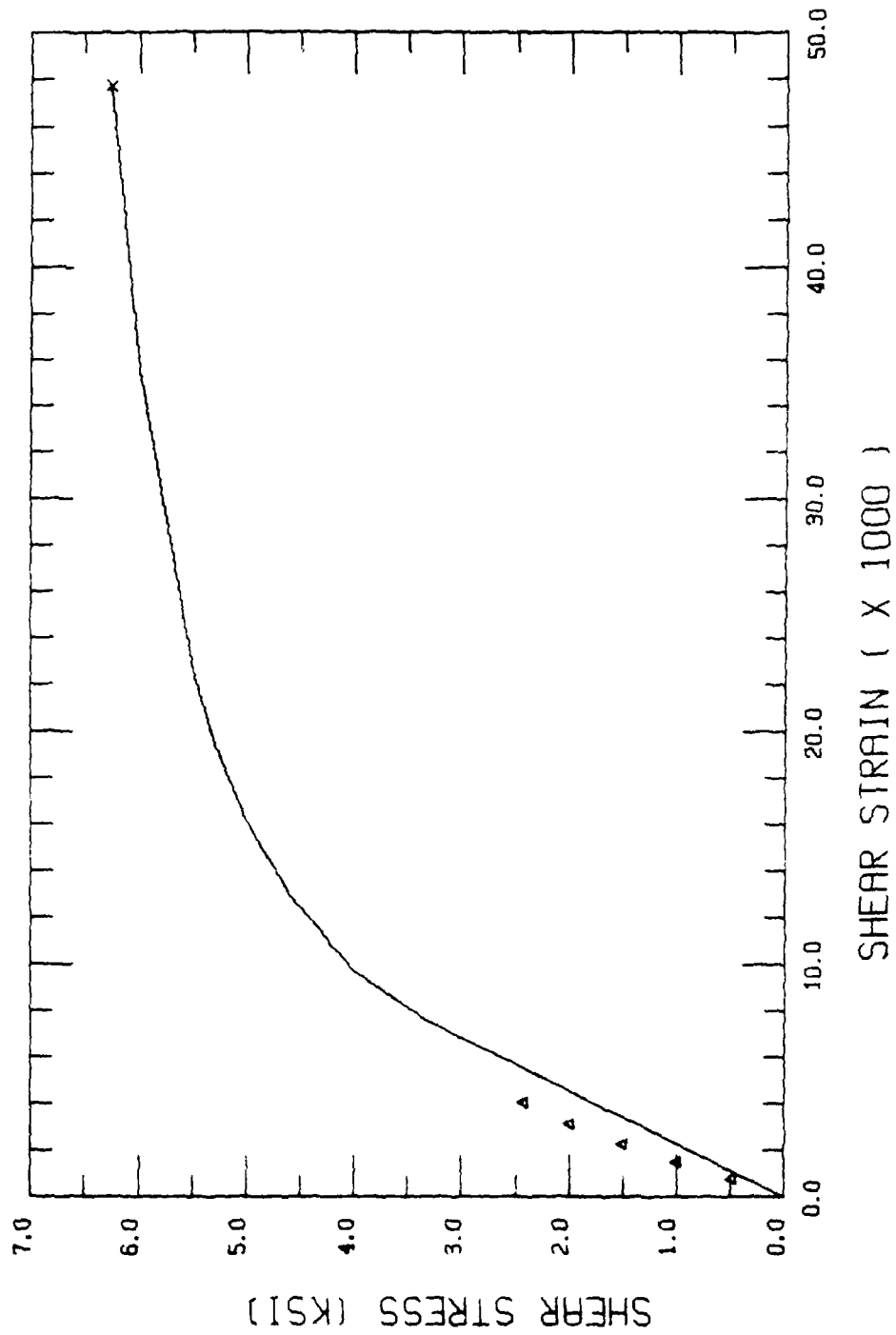
Figure 11. Shear stress-shear strain curves for graphite/epoxy at 100°C, saturated (6.75%M by weight) conditions, comparing micromechanics predictions (shown in triangles) with solid rod torsion test data (shown in solid line).
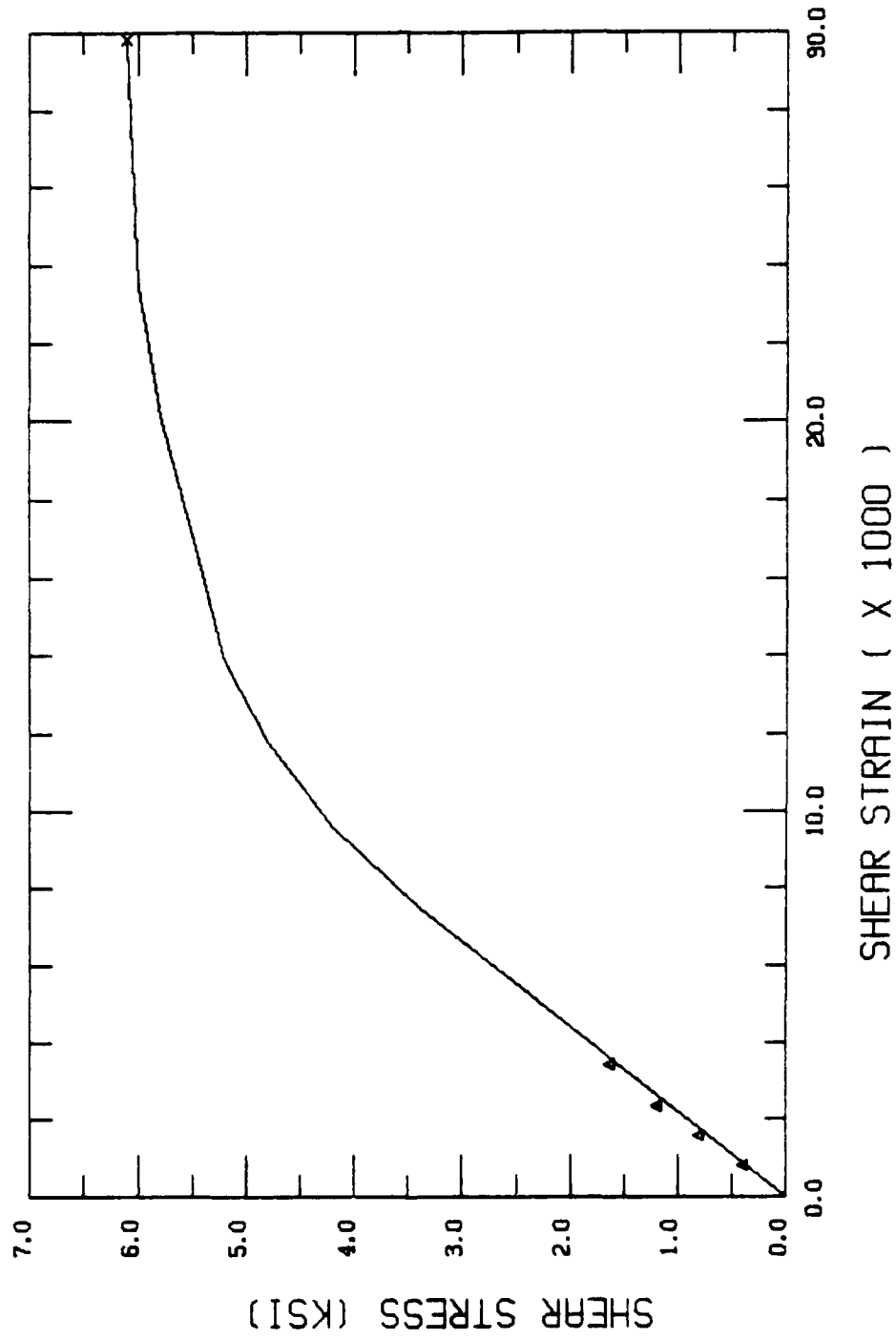
SHEAR STRAIN (X 1000)

Figure 12. Shear stress-shear strain curves for graphite/epoxy at 160°C, dry conditions, comparing micromechanics predictions (shown in triangles) with solid rod torsion test data (shown in solid line).
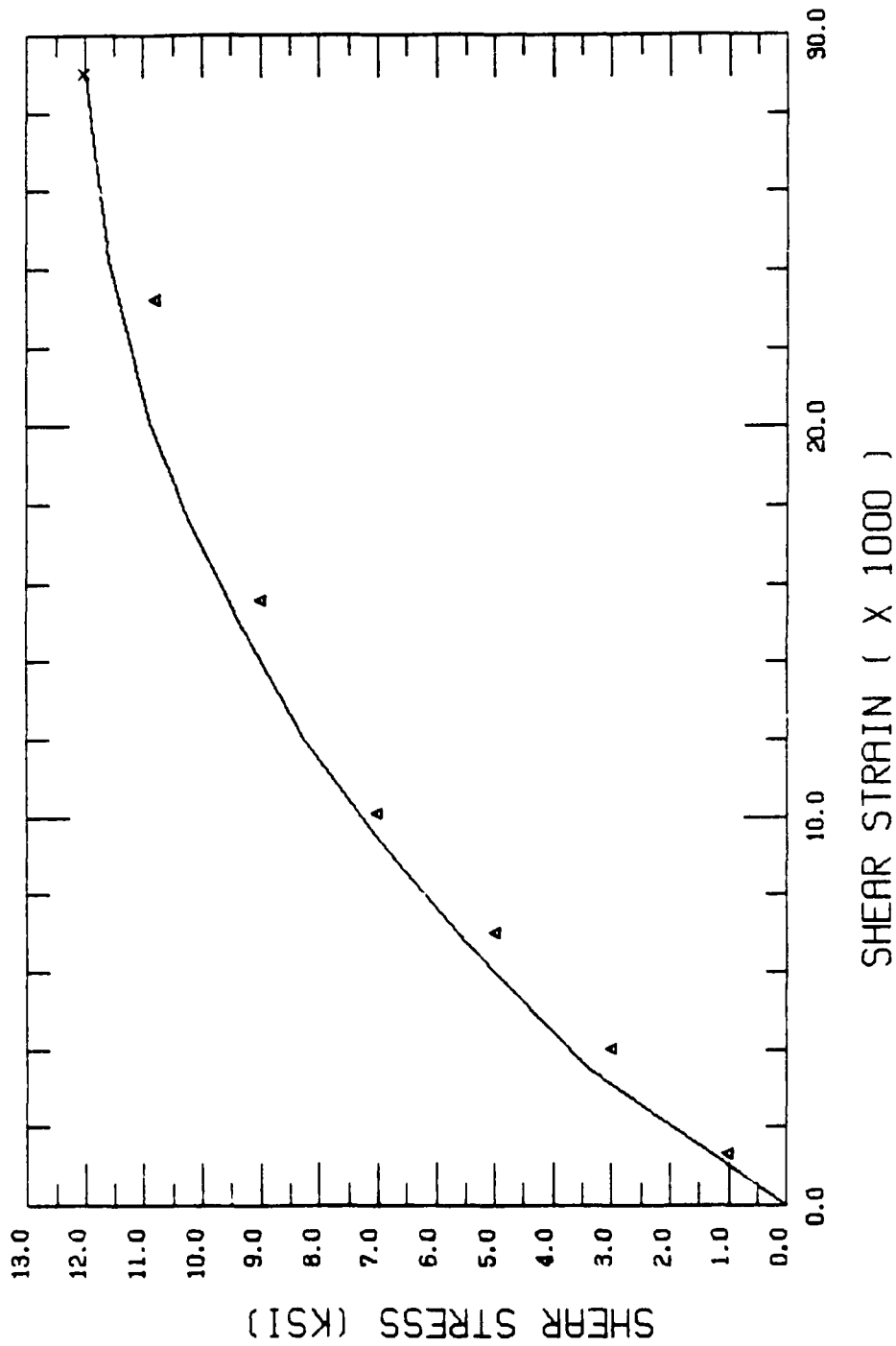
SHEAR STRAIN (X 1000)

Figure 13. Shear stress-shear strain curves for glass/epoxy at room temperature, dry conditions, comparing micromechanics predictions (shown in triangles) with solid rod torsion test data (shown in solid line).
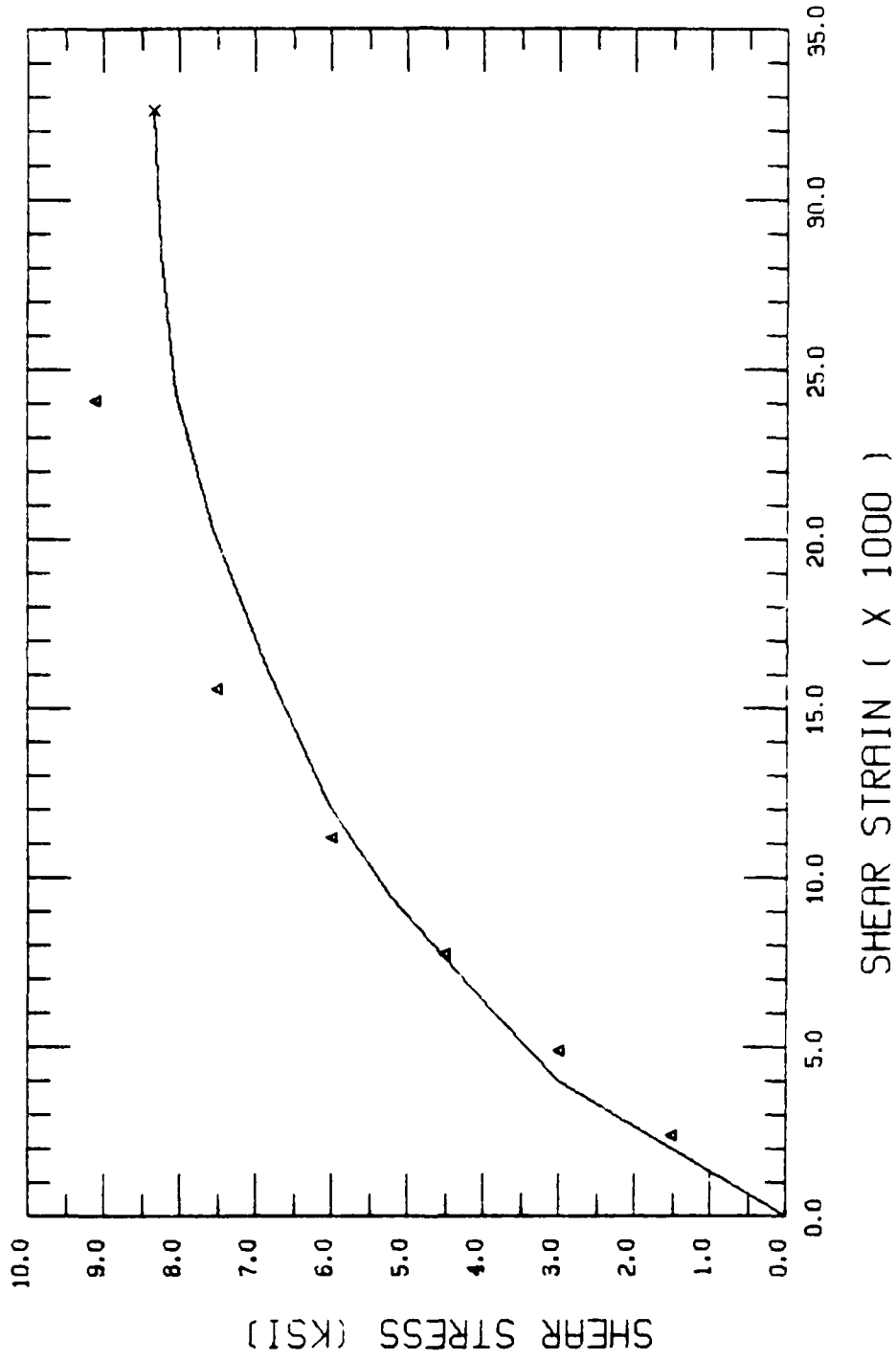
SHEAR STRAIN (X 1000)

Figure 14. Shear stress-shear strain curves for glass/epoxy at room temperature, saturated (6.75%M by weight) conditions, comparing micromechanics predictions (shown in triangles) with solid rod torsion test data (shown in solid line).

SHEAR STRAIN (X 1000)
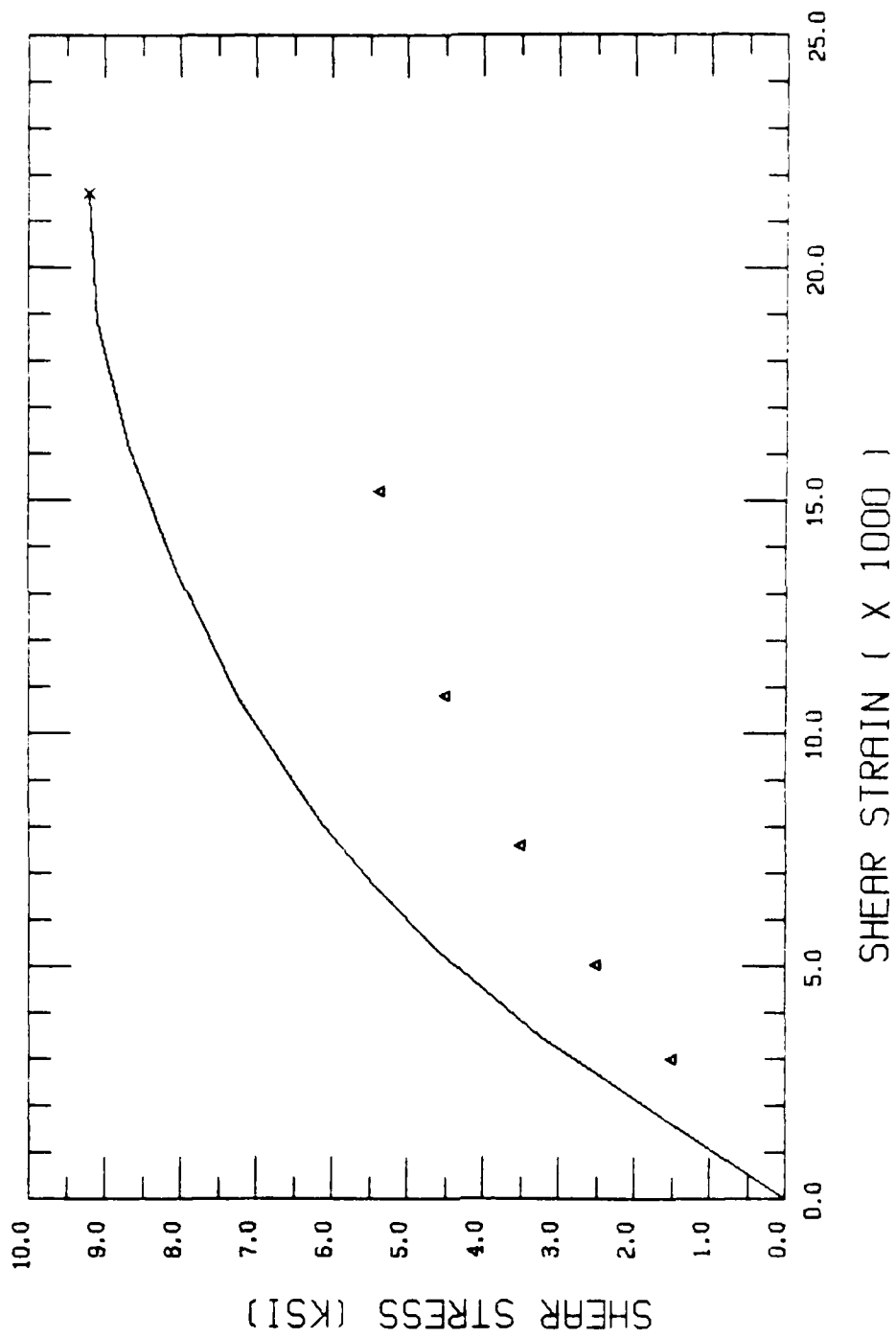
SHEAR STRESS (KSI)

Figure 15. Shear stress-shear strain curves for glass/epoxy at 100°C, dry conditions, comparing micromechanics predictions (shown in triangles) with solid rod torsion test data (shown in solid line).

SHEAR STRAIN (X 1000)
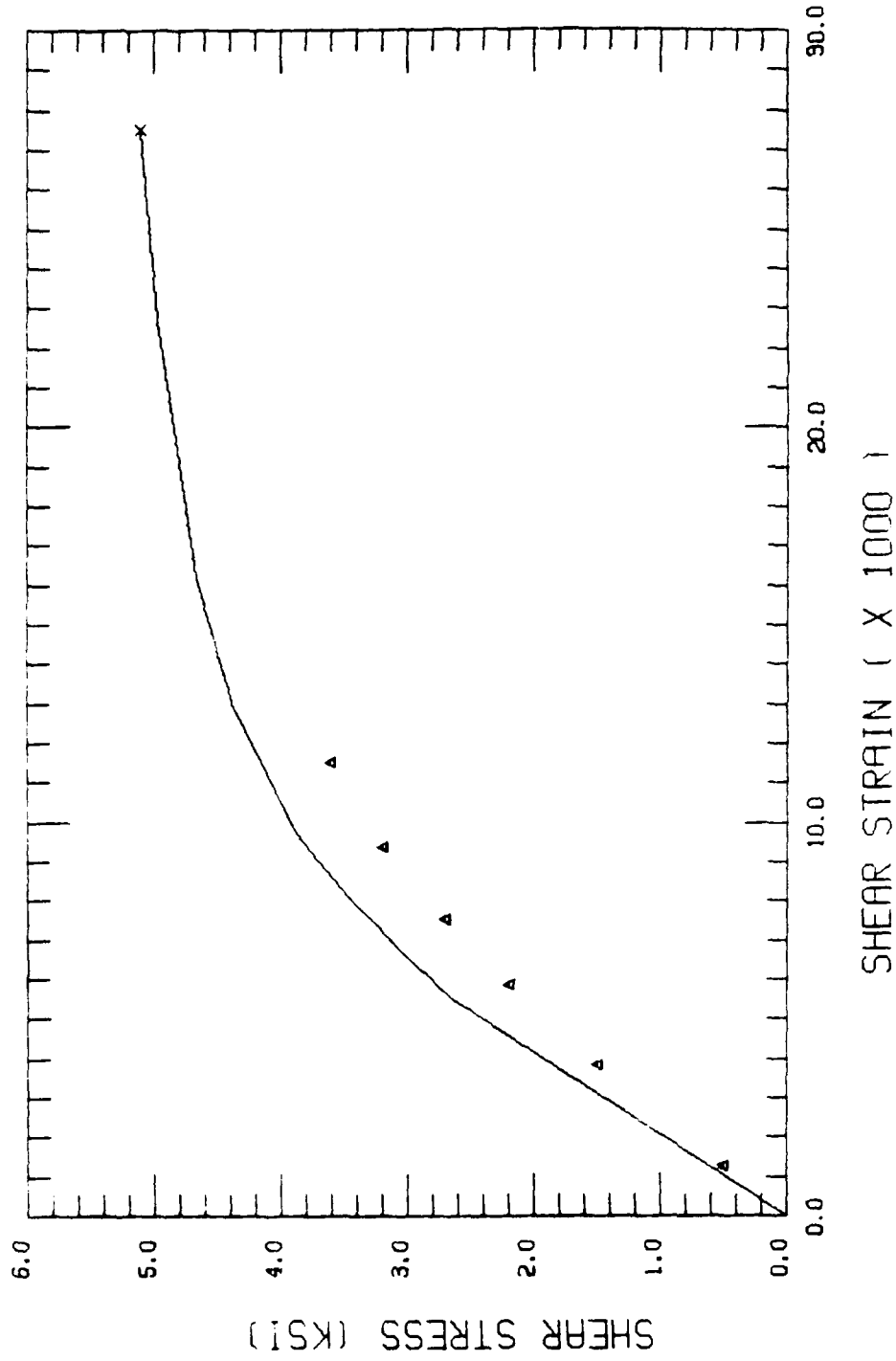
SHEAR STRESS (KSI)

Figure 16. Shear stress-shear strain curves for glass/epoxy at 100°C, saturated (6.75%M by weight) conditions, comparing micromechanics predictions (shown in triangles) with solid rod torsion test data (shown in solid line).

54

SHEAR STRAIN (X 1000)
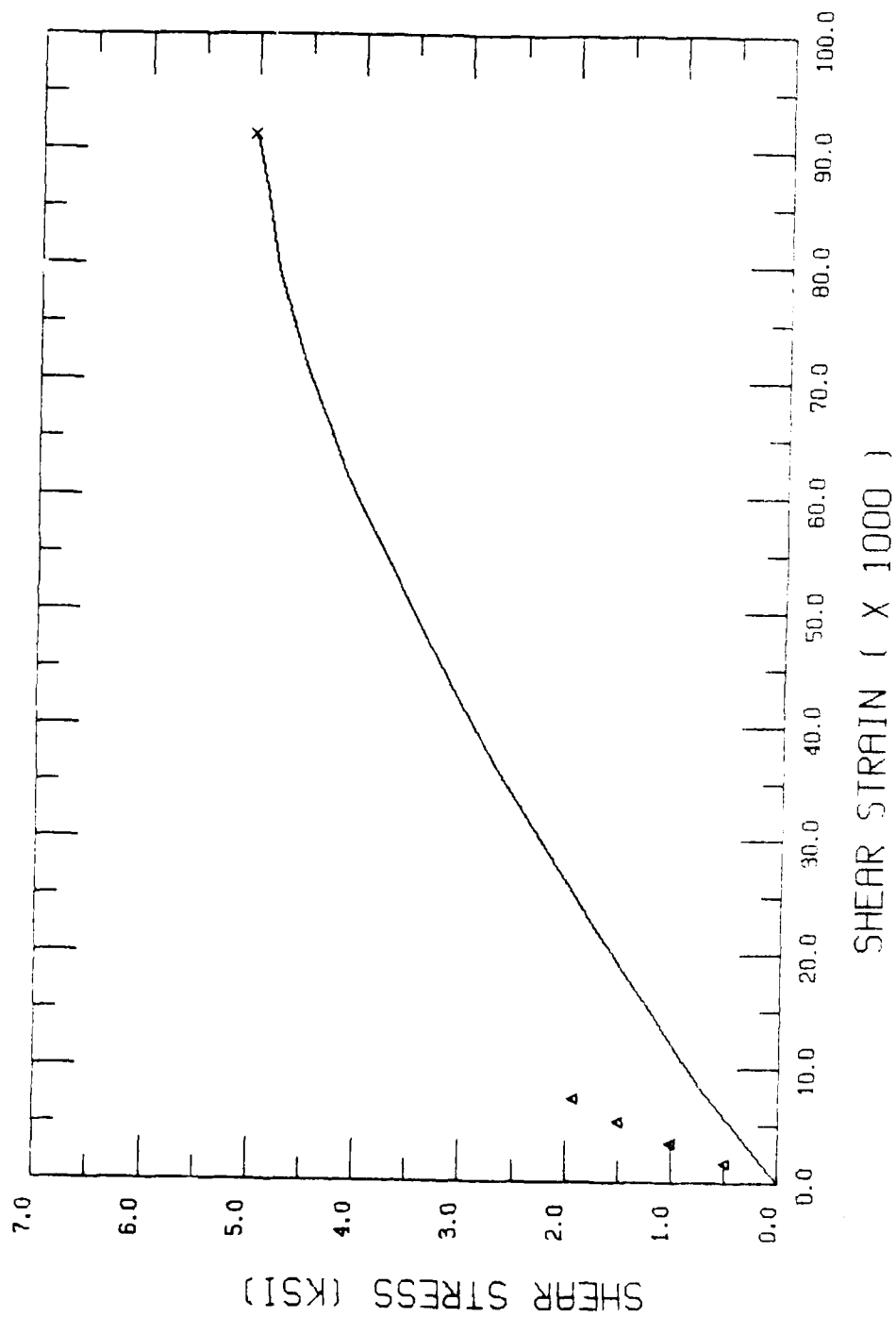
SHEAR STRESS (KSI)

Figure 17. Shear stress-shear strain curves for glass/epoxy at 160°C, dry conditions, comparing micromechanics predictions (shown in triangles) with solid rod torsion test data (shown in solid line).

for fully saturated composite specimens tested at 160°C for both the GR/EP and the GL/EP, the analysis showed failure initiation occuring before preconditioning was completed. Thus, these cases were omitted. This signifies the occurrence of microcracking before the composite is loaded mechanically, solely due to thermal and moisture loads. Thus, not only do temperature and moisture increases lower the matrix properties, they induce stresses sufficiently high to cause failure. As Figures 8 through 17 show, in most cases the predicted composite stress-strain curves were in close agreement with experimental results.

At present, the longitudinal shear micromechanics analysis is only operational up to first element failure, which signifies crack initiation or some other local failure on the micro scale. The present lack of a crack propagation capability prevents the analysis from predicting the actual failure strength of a composite; but it does predict inelastic behavior and the initiation of failure. Thus, each of the Figures 8 through 17 show only the initial portion of the complete shear stress-shear strain curve, but enough to reveal the accuracy of the prediction technique.

The analysis exhibited excellent agreement with experimental values of composite modulus for the GR/EP specimens, along with good predictions of yield strength. This was a significant improvement over the results obtained when using tensile data to generate the octahedral shear stress-octahedral shear strain curves for the matrix material. The tensile data exhibited much less nonlinearity, as indicated in Figure 6. Although the use of data generated from these

tensile tests caused the micromechanics analysis to predict low values for first element failure and low yield predictions, initial modulus predictions were quite accurate, as expected since the initial slopes in Figures 6 and 7 are similar. Therefore, the tension data cannot be refuted, but the results suggest that highly inelastic matrix material behavior does occur when high shear loads are present. Thus, subsequent data comparisions in this section will employ the solid rod torsion test data. In future investigations, the physical signigicance of this difference between the two test methods will deserve some attention.

The slight but consistent overprediction by the analysis of the experiment's stress-strain curves for GR/EP will be noted, while the results for GL/EP are more scattered. It is assumed that the large modulus difference between fiber and matrix is to blame for the slight overpredictions. Considering Table 3 further, the contrast between moduli of fibers and matrix are clearly evident: the longitudinal normal and shear moduli of both fibers are much higher than that of the epoxy. For future consideration it will also be noted that the transverse modulus differences from fiber to matrix are much higher for GL/EP than GR/EP. A general statement can be made concerning these differences: the higher the modulus difference between fiber and matrix, the higher the stress concentrations in a composite resulting from an applied load (loading according to the particular direction of those moduli). Large modulus difference also signifies that any flaw in the composite will magnify the already present stress concentrations,

thus degrading the composite properties. The analysis idealizes a composite material by assuming perfectly homogeneous materials (neglecting all flaws), and perfect bonding between fiber and matrix. Because actual composite materials have many flaws in the form of voids, extraneous inclusions, and debondings, to mention the most common, the present analysis is expected to overpredict slightly in most cases.

Consider the dry GR/EP results in Figures 8, 10, and 12. The overprediction error decreases as temperature increases; at 160°C the predicted modulus and the experimentally measured modulus are essentially equal. The increased temperature causes softening of the matrix material, thus relieving high stress concentrations. Any flaws and imperfect fiber-matrix bonds that occur in the composite affect the total behavior of the composite less, thus the analysis predicts more accurately. This hypothesis is reinforced by a study of the octahedral shear stress contours, as will be discussed later.

The larger errors in the predictions for saturated moisture conditioned GR/EP specimens (Figures 9 and 11) can be attributed to the stress intensity caused by high moisture dilation. While temperature softens the matrix greatly, moisture causes only small degradation of material stiffness, as shown in the octahedral shear stress-octahedral shear strain curves in Figure 7. The higher stresses intensify the detrimental effects of flaws, causing a discrepancy between experiment and theory. Again, the trend toward lower errors as the temperature is increased will be observed.

Although trends are predicted correctly for the GL/EP composites, there is a significant difference between the analysis and the actual experimental data. Figures 13, 14 and 16 show comparisons at room temperature, dry, room temperature, saturated and 100°C, saturated conditions, respectively. These examples show reasonably close agreement between theory and experiment. Large variations are observed for both of the elevated temperature, dry test conditions, however, as shown in Figures 15 and 17. Because the matrix at elevated temperature is highly nonlinear and very low in strength, the prediction is made more difficult than for the other test cases. Also, the probability of experimental error increased at the highest temperature condition (160°C) due to the limitations in temperature control available at the time of the testing, as discussed in Section 4. Disregarding the results in Figure 17 for the above reasons, the results for GL/EP represent underpredictions. As temperature increases, the underpredictions grow for each separate moisture condition. The cause of this error is unknown at this time; a study of the stress contours offered no explanation.

Typical behavior of a shear specimen on the micro scale can be seen clearly in the contour plots produced from the micromechanics results of dry GR/EP specimens tested at room temperature. Octahedral shear stresses due to curing ranged up to 75 percent of the elastic limit, as shown in Figure 18a. Octahedral shear stress is an indicator of distortional energy in the material; the highest values are seen to occur in regions of close fiber spacing, directly between the fibers,
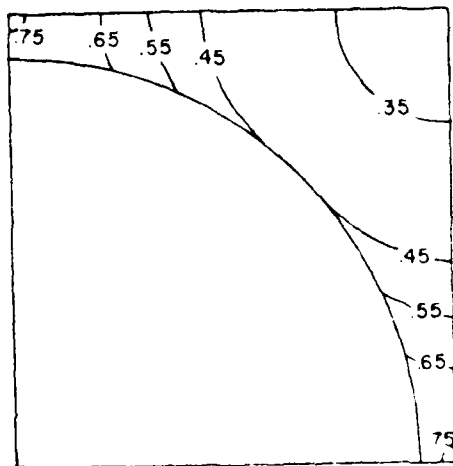
a) Octahedral shear stress
   after cooldown from 177°C
   cure temperature to 21°C
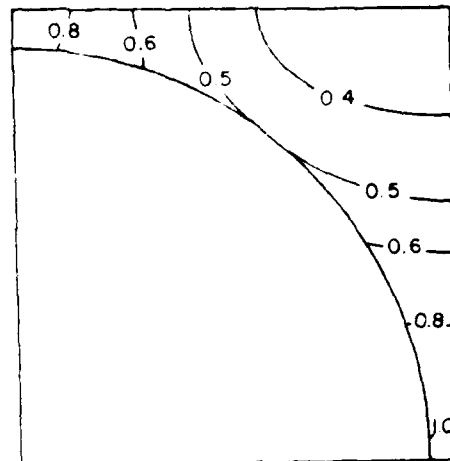
b) Octahedral shear stress
   at predicted first element
   yield, $\bar{\tau}_{xz}$ = 2 ksi
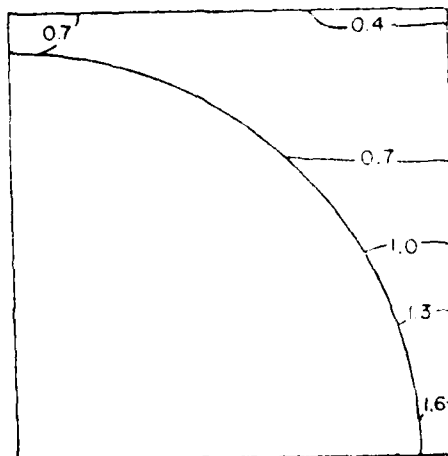
c) Octahedral shear stress
   at experimentally deter-
   mined composite yield
   stress, $\bar{\tau}_{xz}$ = 4.5 ksi
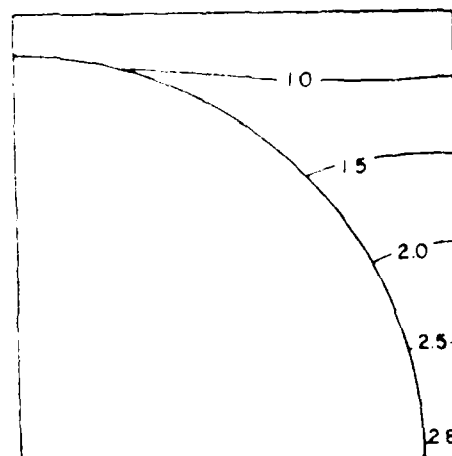
d) Octahedral shear stress
   at predicted first element
   failure, $\bar{\tau}_{xz}$ = 9.5 ksi

Figure 18.   Contour plots of octahedral shear (normalized with respect
             to matrix yield stress, 4.18 ksi), maximum principal, min-
             imum principal, interface normal, and interface shear stress
             within a graphite/epoxy solid rod torsion specimen at room
             temperature, dry conditions.

e) Maximum principal stress (ksi) at predicted first element failure, τ_{xz} = 9.5 ksi
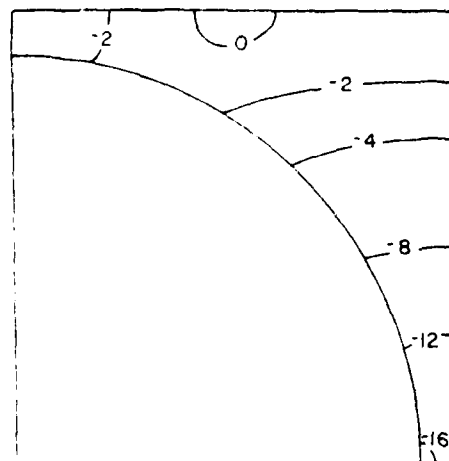
f) Minimum principal stress (ksi) at predicted first element failure, τ_{xz} · 9.5 ksi
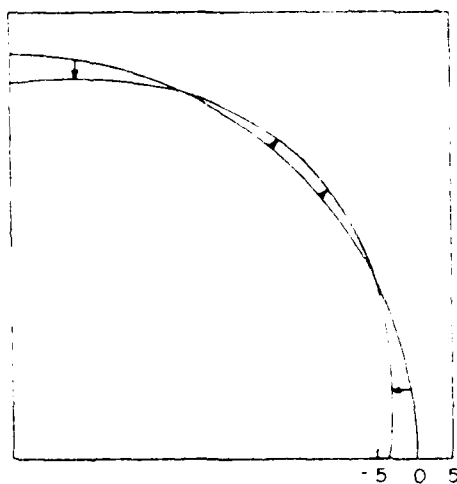
g) Interface normal stress (ksi) after cooldown from 177°C cure temperature to 21°C

h) Interface normal stress (ksi) at predicted first element failure, τ_{xz} = 9.5 ksi

Figure 18. (continued) Contour plots of octahedral shear (normalized with respect to matrix yield stress, 4.18 ksi), maximum principal, minimum principal, interface normal, and interface shear stress within a graphite/epoxy solid rod torsion specimen at room temperature, dry conditions.
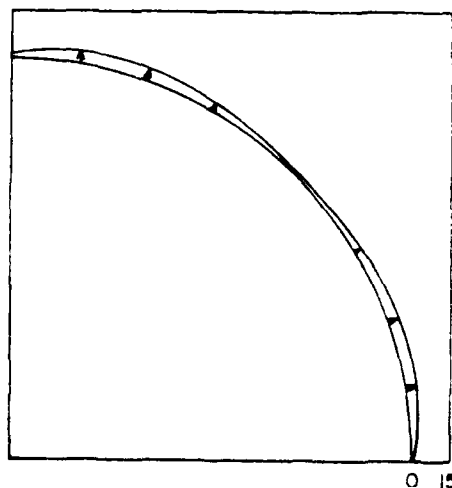
i) Interface shear stress
(ksi) after cooldown
from 177°C cure temper-
ature to 21°C
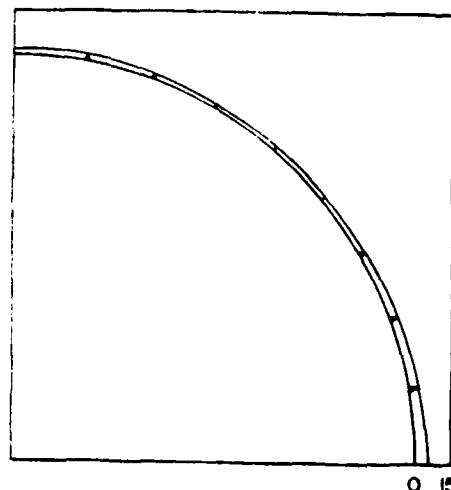
j) Interface shear stress
(ksi) at first element
yield, τ_{xz} = 2.5 ksi
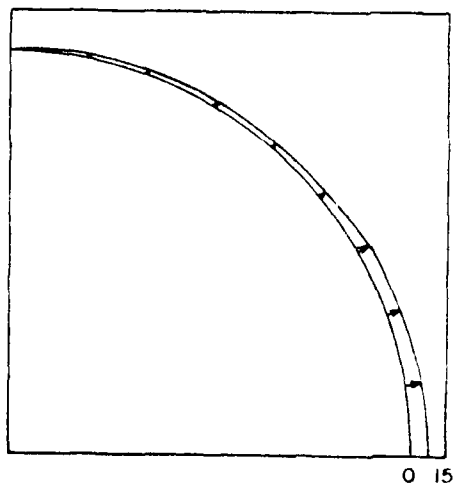
k) Interface shear stress
(ksi) at data yield
point, τ_{xz} = 4.5 ksi
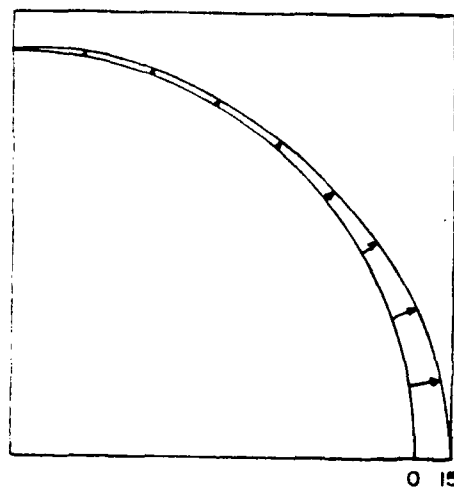
l) Interface shear stress
(ksi) at first element
failure, τ_{xz} = 9.5 ksi

Figure 18.   (continued)   Contour plots of octahedral shear (normalized
with respect to matrix yield stress, 4.18 ksi), maximum
principal, minimum principal, interface normal, and inter-
face shear stress within a graphite/epoxy solid rod torsion
specimen at room temperature, dry conditions.

62

where element yield (Figure 18b) and eventually first failure (Figure
18d) occur. The 2.8% contour value corresponding to first element
failure represents an octahedral shear stress of 11.9 ksi. In Figure
8, the data indicate yield at 4.5 ksi, although the octahedral shear
stress contour plot (Figure 18c) shows nearly 20 percent of the matrix
to have already yielded, revealing the fact that local matrix yielding
occurs long before the composite as a whole begins to show any sign of
nonlinear response. Even the predicted shear stress-shear strain
response (shown by the triangles in Figure 8) remains nearly linear
well past the point of first element yielding.

While the octahedral shear stress failure criterion predicts
failure directly between fibers, a maximum stress criterion would dis-
agree; high tensile stresses are seen to occur near the fiber in
Figure 18e. High compressive stresses are seen to occur at the
interface along the x axis of symmetry (Figure 18f) at the fiber-matrix
interface, indicating a potential failure of the interface bond. The
octahedral shear stress criterion indicates a probable interfiber
microcrack failure, which would propagate to the interface, or merely
cause a split directly between adjacent fibers. Both criteria predict
failure in the same general region of close fiber spacing, but when
dealing with an actual composite, the actual failure mode will also be
influenced by the particular flaws in that region. For example, a
local region of poor fiber/matrix bonding would be opened by the high
tensile stress shown in Figure 18e.

Cooldown from the cure temperature induces high compressive normal stresses at the interface, due to the contraction of matrix material around the fiber (Figure 18g). The contraction of the matrix material in conjunction with the constant displacement boundary conditions moves the boundaries together slightly, enough to compress the small volume of material near the axes of symmetry. This normal stress is unaffected by subsequently applied longitudinal shear loads, and only slightly increased by contributions due to inelastic material response at higher levels of the applied shear stress, as shown in Figure 18h. The reasons for this are that there is no coupling between normal and shear stresses during elastic behavior, and that when coupling does occur (when the matrix behavior is inelastic), the deviatoric stress tensor is so sparsely populated that the normal stress is only increased by about three percent.

Due to the additional longitudinal shear stress components, the present analysis must include both in-plane and out-of-plane shear stresses in the interface shear stress contour plots, in contrast to previous treatments [15, 30, 38]. Now the shear stress contour represents only the magnitude; the direction of the interface shear stress can vary from position to position along the fiber in any direction on the fiber surface.

Interface shear stresses developed during cooldown (Figure 18i) are only 25 percent of the shearing stress at failure (Figure 18l). It will be noted that the curing stresses become purely hydrostatic on the horizontal and vertical axes of symmetry and at 45°, due to

geometric symmetry. Viewing Figures 18i, j, k and l consecutively shows that the initial curing residual shear stress is small relative to the load-induced shear stress, which eventually initiates failure.

The GR/EP under a test condition of room temperature, when moisture-saturated (6.75 percent moisture by weight), reveals very high octahedral shear stresses and interface normal stresses due to moisture dilatation, as seen in Figures 19a and 19b. Although thermal contraction during cooldown counteracts the subsequent moisture dilatation, the extent of moisture dilatation far overshadows the thermal contraction. The majority of matrix material is already inelastic before loads are applied, (Figure 19a) which reduces the subsequent load-carrying capability, while the moisture also softens the matrix, thus reducing its ultimate strength. Figures 19c and 19d show the increased inelastic behavior that entirely envelopes the matrix at failure. The moisture loading governs the contours, i.e., they remain more nearly symmetric than in the loading condition without moisture (Figure 18d). Again a high interface normal stress is present (Figure 19e), while a high interface shear stress (Figure 19f) contributes to the high octahedral shear stress state shown in Figure 19d. The maximum and minimum principal stress contours (Figures 19g and 19h) have opposite results than in the room temperature, dry specimens, due to the opposite effects of moisture and curing stresses. The minimum principal stress shows a highest absolute value at 45° from the x-axis of symmetry at the interface. Because the absolute value of the maximum principal stress is higher than the minimum principal stress,
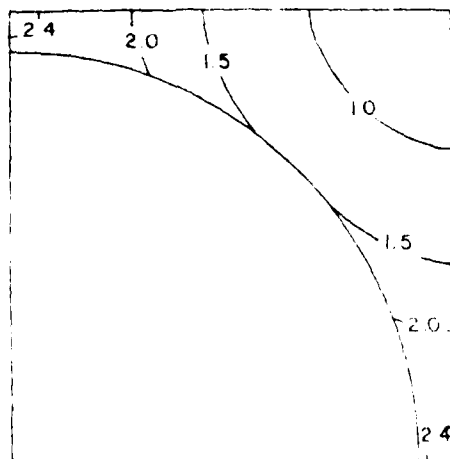
a) Octahedral shear stress
after cooldown from 177°C
cure temperature to 21°C
and moisture absorption of
6.75%M
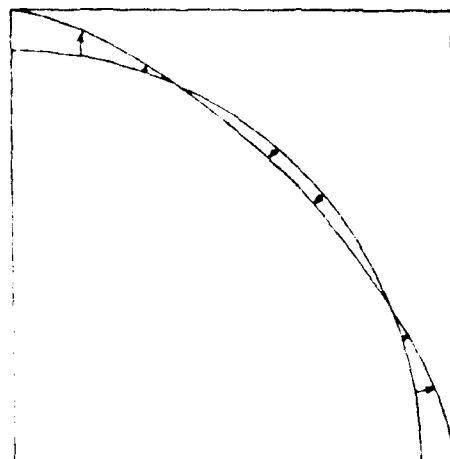
b) Interface normal stress
(ksi) after cooldown from
177°C cure temperature to
21°C and moisture absorption
of 6.75%M
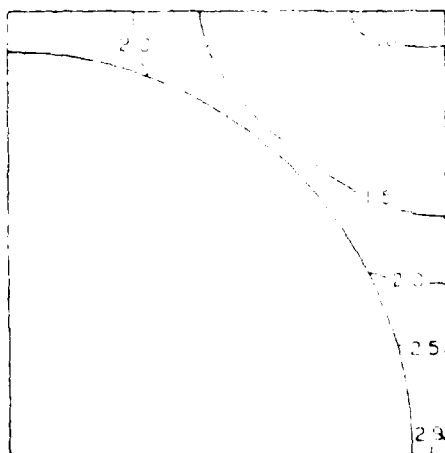
c) Octahedral shear stress at
experimentally determined
composite yield stress,
$\bar{\tau}_{xz}$ = 4.0 ksi
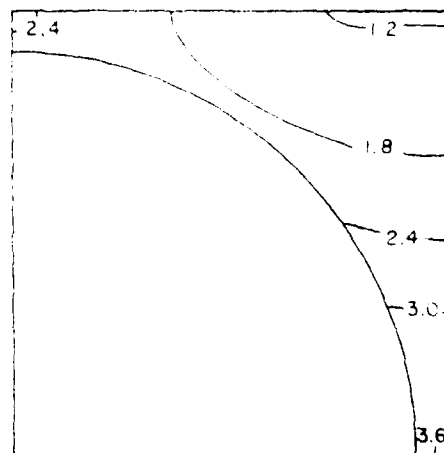
d) Octahedral shear stress at
predicted first element
failure, $\bar{\tau}_{xz}$ = 8.1 ksi

Figure 19. Contour plots of octahedral shear (normalized with respect
to matrix yield stress, 2.88 ksi), maximum principal, min-
imum principal, interface normal, and interface shear stress
within a graphite/epoxy solid rod torsion specimen at room
temperature, saturated conditions (6.75%M by weight).
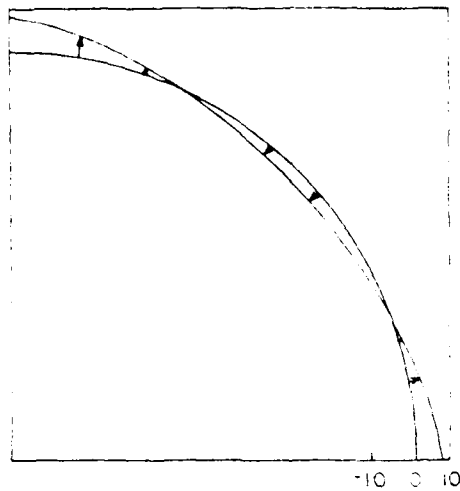
e) Interface normal stress (ksi) at predicted first element failure, $_{xz}$ = 8.1 ksi
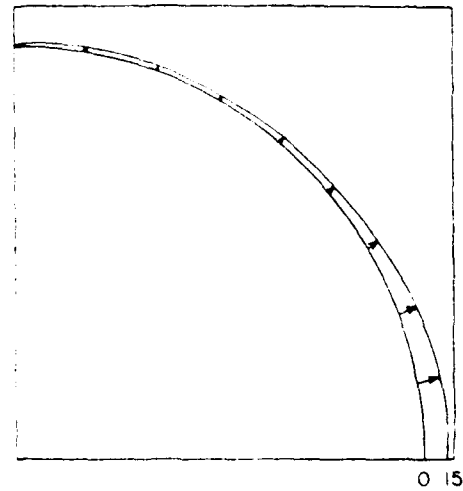
f) Interface shear stress (ksi) at predicted first element failure, $\bar{\tau}_{xz}$ = 8.1 ksi
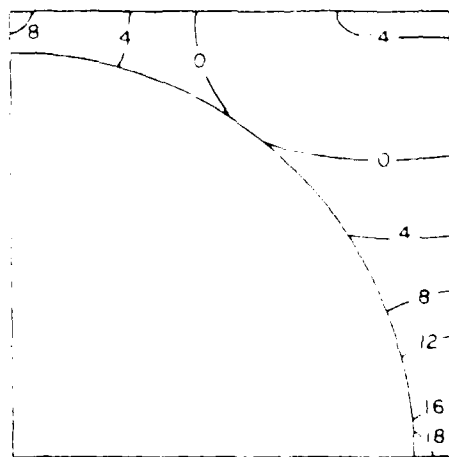
g) Maximum principal stress (ksi) at predicted first element failure, $\bar{\tau}_{xz}$ = 8.1 ksi
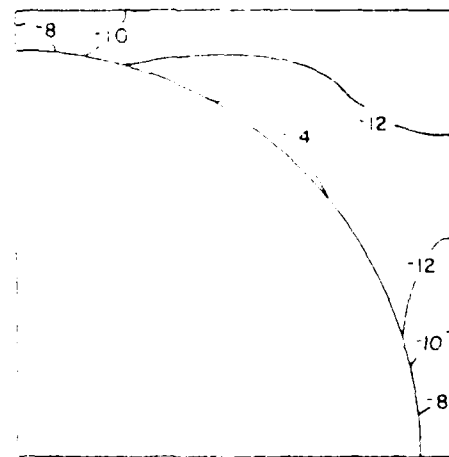
h) Minimum principal stress (ksi) at predicted first element failure, $\bar{\tau}_{xz}$ = 8.1 ksi

Figure 19. (continued) Contour plots of octahedral shear (normalized with respect to matrix yield stress, 2.88 ksi), maximum principal, minimum principal, interface normal, and interface shear stress within a graphite/epoxy solid rod torsio specimen at room temperature, saturated conditions (6.75%M by weight).

failure would be predicted to occur at the fiber-matrix interface nearest the x-axis if the maximum stress criterion were used. A different result is again shown by the octahedral shear stress criterion (Figure 19d), which predicts an interfiber failure, although it is near the same area.

The elevated temperature (100°C) GR/EP specimen under dry conditions shows a relatively less intense octahedral shear stress state due to curing (Figure 20a) than the room temperature, dry specimen. This occurs not only because of the smaller temperature excursion, but also because of the lower stiffness properties at the elevated temperature. As noted earlier, this results in lower stress concentrations when flaws are present in real specimens. Thus the assumption of no flaws and perfect bonds becomes less severe, and the analysis predicts more accurately. Interface normal stresses are negligible compared to the magnitude of the octahedral shear stresses occurring at failure (Figure 20b), while maximum and minimum principal stress contours predict maximum absolute values at the same point as the octahedral shear stress contours: between the fibers on the x-axis of symmetry (Figures 20c, d). Therefore, an elevated temperature GR/EP specimen would tend to fail within the matrix, where a crack would intiate and subsequently begin to propagate.

Because the GL/EP at room temperature and 6.75 percent moisture has a smaller fiber volume (50.5 percent) than the GR/EP at similar conditions, and because the fiber properties are different than graphite, slightly different results can be expected from the
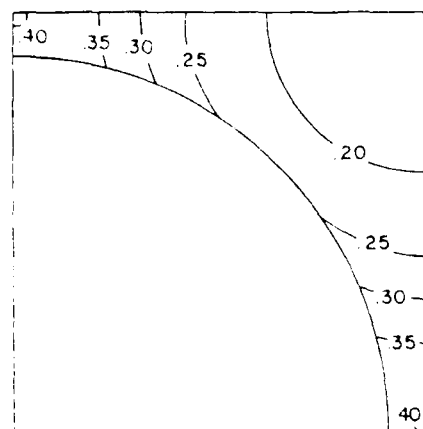
a) Octahedral shear stress after cooldown from 177°C cure temperature to 100°C

b) Octahedral shear stress at predicted first element failure, $\bar{\tau}_{xz}$ = 4.6 ksi
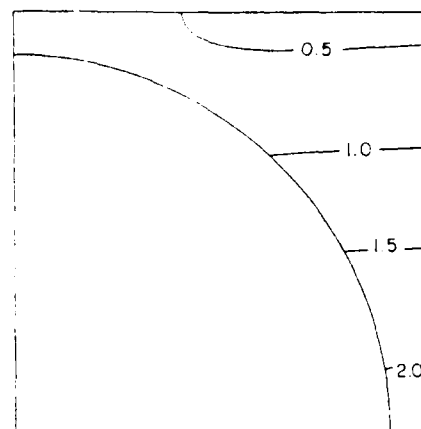
(normalized with respect to matrix yield stress, 2.81 ksi)
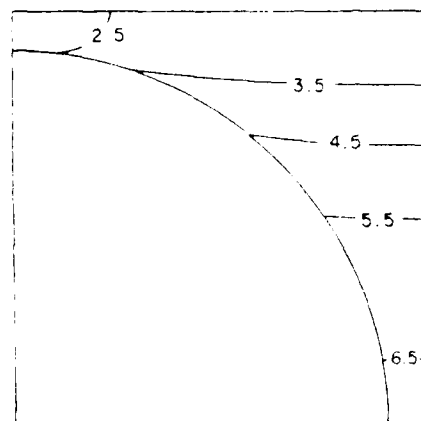
c) Maximum principal stress (ksi) at predicted first element failure, $\bar{\tau}_{xz}$ = 4.6 ksi
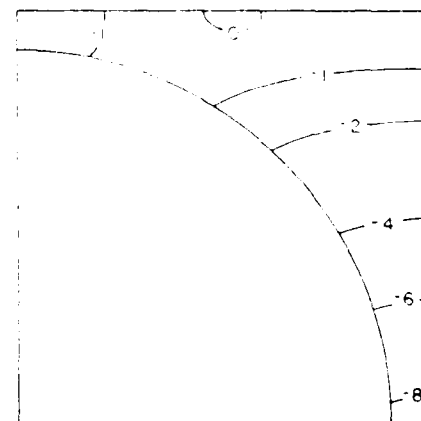
d) Minimum principal stress (ksi) at predicted first element failure, $\bar{\tau}_{xz}$ = 4.6 ksi

Figure 20. Contour plots of octahedral shear, maximum principal and minimum principal stresses within a graphite/epoxy solid rod torsion specimen at 100°C, dry conditions.

microanalysis. But after cooldown from the curing temperature and moisture conditioning, GR/EP and GL/EP show very similar octahedral shear stress contours (see Figures 19a and 21a). Coefficients of thermal expansion vary markedly between the glass fiber and the graphite fiber (see Table 3). The graphite fiber expands axially when temperature is lowered, and contracts in the transverse direction. The glass fiber, being isotropic, contracts in all material directions when temperature is lowered. However, the matrix thermal contraction is much higher than that of either fiber. These large differences between coefficients of thermal expansion from fiber to matrix cause stresses to be induced. These differences are highest in the axial direction of the GR/EP, and lowest in the transverse direction of GR/EP, while the GL/EP is in between, although quite high (see Table 3). Considering this and the fact that more matrix is present in the GL/EP because of its lower fiber volume, the overall thermal and moisture effects tend to be equal for both composites. Therefore, similar contours are seen for both GR/EP and GL/EP in Figures 19a and 21a.

Because of end constraints applied in this analysis, hygrothermal loads will not induce longitudinal shear stresses. Considering the transverse plane only, the overwhelming moisture dilatation tends to push outward on the boundaries. Since the boundaries are constrained to have a constant displacement, the area of highest matrix volume toward the upper right corner of the quadrant will be slightly in compression, while the area of small matrix volume will be in large tension, as shown in Figure 21b. Because the fiber is not affected by
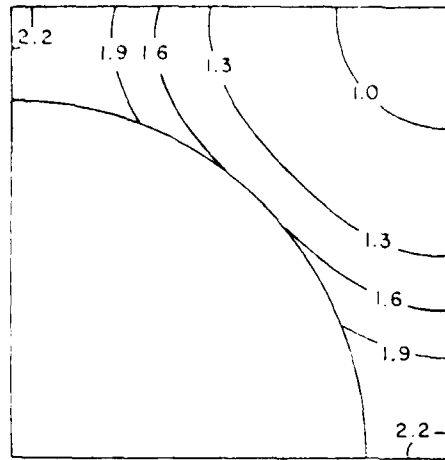
a) Octahedral shear stress after cooldown from 177°C cure temperature to 100°C and moisture absorption of 6.75%M
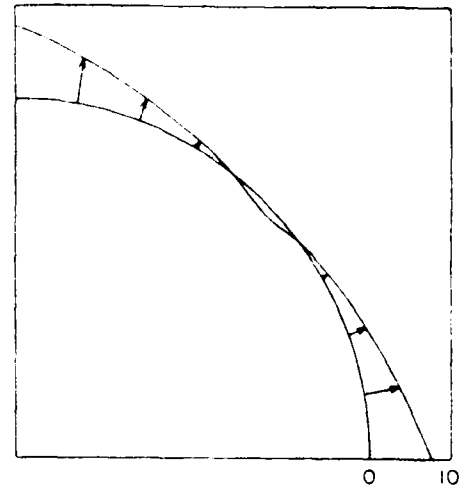
b) Interface normal stress (ksi) after cooldown from 177°C cure temperature to 100°C and moisture absorption of 6.75%M
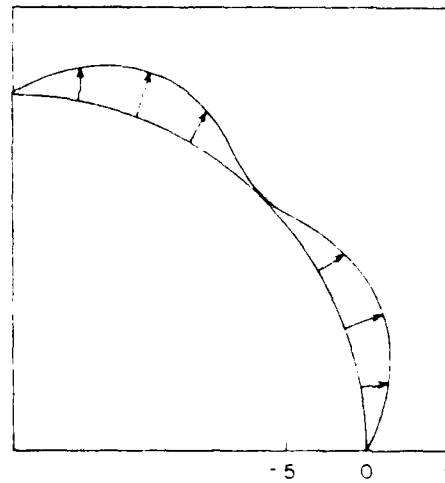
c) Interface shear stress (ksi) after cooldown from 177°C cure temperature to 100°C and moisture absorption of 6.75%M
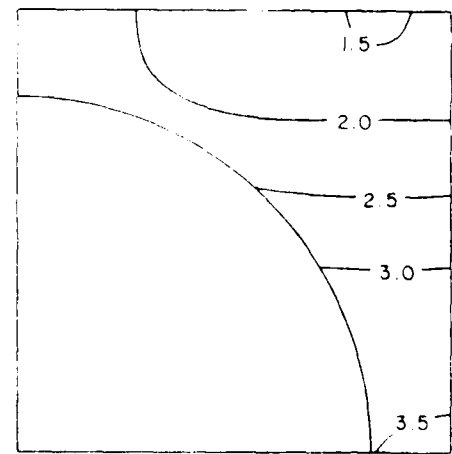
d) Octahedral shear stress at predicted first element failure. τ_{xz} = 9.1 ksi

Figure 21. Contour plots of octahedral shear (normalized with respect to matrix yield stress, 2.88 ksi), interface normal and interface shear stress within a glass/epoxy solid rod torsion specimen at room temperature, saturated conditions (6.75%M by weight).

this moisture, it tends to hold the matrix in place while the matrix tends to dilate out from the center. Thus, shear stress is induced along the interface. Because matrix dilatation occurs in all directions, and because of geometric symmetry, only a hydrostatic stress is present at the center of the fiber/matrix interface, as shown in Figure 21c. Constant displacement boundary conditions at the edge of the quadrant plot restrict shear strains there, and again only a hydrostatic stress is present. This is shown in Figure 21c by the absence of shear stress.

As the applied shear stress is increased until the first element failure occurs, the contours propagate in a manner similar to previous cases. But comparing Figures 21d and 19d, the average stress in the matrix for GL/EP is higher (9.1 ksi) than that for GR/EP (8.1 ksi). The matrix in GL/EP has yielded to a greater extent than in GR/EP, signifying more damage has taken place, and more energy absorbed. Thus, lower fiber volume makes a more uniform stress distribution possible in the matrix, i.e., the stress concentration due to the fiber decreases.

The brief results presented here show good correlation with experimental data, suggesting that the micromechanics analysis is valid. These results cannot be considered conclusive, of course. A much more comprehensive study should be undertaken in the future, to reinforce the present results.

Laminate Analysis

If laminate behavior can be predicted by the microanalysis used
in conjunction with a laminate analysis, further value and accuracy
of the micromechanics analysis can be demonstrated. Longitudinal shear
stresses are indeed a necessary consideration in laminate analysis,
and are capable of being considered in the present micromechanics
analysis. The use of micromechanics analyses was restricted to uni-
directional laminates in prior works, when no longitudinal shear con-
siderations were taken into account. The laminate analysis used must
be compatible with the restrictions of the micromechanics analysis,
and certain assumptions must be made. Because application of in-
plane shear stress (τ_{xy}) is not a capability of the present micro-
mechanics analysis, a two-dimensional classical laminated plate
point stress analysis was chosen over a three-dimensional finite
element laminate analysis. The AC-3 laminate point stress analysis
computer program is operational at the University of Wyoming [5].
Basically, it describes elastic stresses and strains induced in each
ply due to loads applied to the laminate. These can be temperature
and moisture loads as well as mechanical loads.

Compatibility of the two analyses and the scheme of arriving at an
inelastic stress-strain curve for a particular laminate is described
by the following four steps:

1. Calculate ply properties from the micromechanics analysis.

2. Apply the laminate point stress analysis to the prescribed
laminate, loaded in the prescribed manner, to obtain the stress

state induced in each ply.

3. Use the micromechanics analysis to analyze each unique ply of the laminate, holding loads in the same ratios as the laminate analysis predicted. This will result in inelastic stresses and strains in each ply when loaded to high levels.

4. Transform the stress and strain states back to laminate coordinates to obtain a laminate stress-strain curve. This curve can be used for comparisions with laminate experimental data.

Experimental data were available for a 57.5 percent fiber volume, $[\pm45]_{4s}$ GR/EP laminate at four combinations of temperature and moisture conditions [30], viz, room temperature, dry (RTD); room temperature, one percent moisture by weight (RTW); elevated temperature (103 °C), dry (ETD); and elevated temperature ('03°C), one percent moisture (ETW). The conditions will hence be referred to using the abbreviations in parentheses; i.e., RTD, RTW, ETD, ETW, similar to the notation of Reference [30]. Summarizing, Reference [30] was an investigation of compression fatigue properties of composites. Static compression and compression fatigue tests were performed on materials at various hygrothermal conditions. Theoretical predictions of failure mechanisms were studied through a micromechanics analysis [1]. The static compression experimental data for the $[\pm45]_{4s}$ laminate were chosen for the purpose of comparing them with theoretical predictions. Both constituent materials were the same as the graphite and epoxy proviously described in Section 3.

To begin the analysis, unidirectional ply properties are

calculated using the micromechanics analysis, to be consistent with the properties utilized later when inelastic strains are to be calculated. Constituent properties for the AS-graphite fiber and the epoxy matrix are the same as those shown in Section 3. Composite properties are shown in Table 4; the stiffness values correspond closely to properties found by Northrop Corporation and the University of Wyoming [30]. However, thermal and moisture coefficients of expansion differ considerably. It is important to be mutually consistent in the present development from one analysis to the other, i.e., properties used initially in the laminate analysis must correspond to values (see Table 4) used later in the micromechanical analysis. Overall, temperature and moisture lower all the properties recorded. Also, note the small value for longitudinal thermal expansion coefficient at the elevated temperature, due to the negative coefficient of thermal expansion of the graphite constituent.

The ply properties as calculated using the micromechanics analysis are used in the laminate point stress analysis, where ply stress states due to temperature, moisture and/or applied loads are obtained. In applying a thermal or moisture load to the laminate, the laminate analysis assumes the input elastic properties to remain constant throughout the temperature or moisture change. Because the matrix modulus is actually not constant, but decreases significantly with increasing temperatures, the predicted curing stresses will be higher than they actually are. To more accurately estimate the curing stresses, an effective temperature change can be used which is smaller than

TABLE 4

PROPERTIES CALCULATED FROM MICROMECHANICS ANALYSIS
FOR USE IN LAMINATE ANALYSIS

PROPERTY	Predicted Elastic Properties at Environmental Conditions Indicated				Properties at Predicted First Failure
	RTD	RTW	ETD	ETW	RTD
E_L (Msi)	18.700	18.690	18.563	18.554	18.409
E_T (Msi)	1.467	1.450	1.172	1.147	1.559
G_{LT}(Msi)	0.918	0.897	0.611	0.589	0.441
ν_{LT}	0.2573	0.2571	0.2544	0.2542	0.2805
α_L (x 10^{-6}/°C)	0.477	0.455	0.166	0.144	0.531
α_T	32.40	32.35	31.70	31.70	33.86
β_L (x 10^{-3}/%M)	0.042	0.041	0.026	0.025	0.046
β_T	1.082	1.078	1.031	1.027	1.184

the actual temperature change. For curing from 177°C to 21°C, an effective temperature change of 111°C was used rather than the actual 156°C. In curing from 177°C to 103°C, only a 42°C effective temperature change was used. These assumed effective temperature change values were taken from Reference [30]. Actual loads to be applied to model stresses induced in the individual plies during each case of curing and conditioning are shown in Table 5, along with actual load ratio increments due to the subsequently applied axial compressive load. To arrive at these values, the laminate analysis uses the composite ply properties that were calculated by the micromechanics analysis. The resulting stress state is calculated in both ply coordinates and laminate coordinates by the laminate analysis, thus eliminating the necessity of transforming the stress state by hand for subsequent input to the micromechanics analysis.

TABLE 5

LOAD RATIOS CALCULATED FROM LAMINATE
ANALYSIS FOR USE IN MICROMECHANICS
ANALYSIS FOR $[\pm45]_{4s}$ LAMINATE

HYGROTHERMAL LOADS

STRESSES (ksi)	RTD (-111°C)	RTW (1% M,-111°C)	ETD (-42°C)	ETW (1% M,-42°C)
σ_z	-4.65	-3.23	-1.41	-0.33
σ_x	4.65	3.23	1.41	0.33
τ_{xz}	0.0	0.0	0.0	0.0

APPLIED LOAD RATIOS FOR -1000 psi AXIAL COMPRESSIVE STRESS

STRESSES (psi)	RTD	RTW	ETD	ETW
σ_z	-912	-912	-928	-930
σ_x	- 88	- 88	- 72	- 70
τ_{xz}	500	500	500	500

The micromechanics analysis is now assumed to model a single uni-
directional ply of the laminate in ply coordinates by modeling one
quadrant of the repeating unit cell, as depicted in Figure 22. The
assumption that boundaries displace uniformly, was described earlier in
Section 3. The laminate analysis intrinsically makes this assumption,
since classical point stress analyses do not include interlaminar
shear stresses. In an actual composite, certain interlaminar shear
stresses cause shear deformation in the plane transverse to the fiber
direction. This is in-plane deformation for the micromechanics model,
which is inadmissible in this analysis due to the constant displacement
boundary conditions. Therefore, interlaminar shear stresses are as-
sumed to be negligible in the present example. Another assumption is
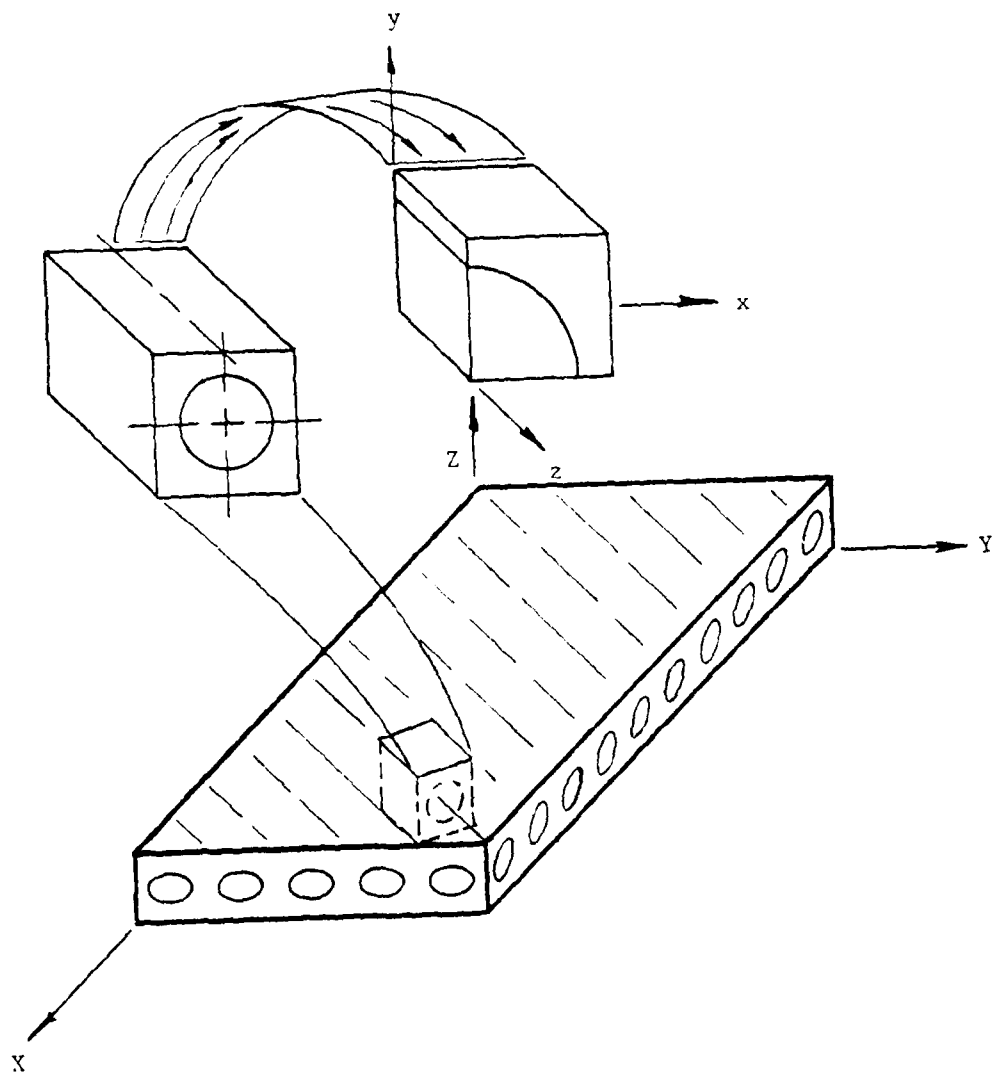
Figure 22. Development of micromechanical model from a 45° ply.

that the load ratios will change only negligibly due to inelastic ma-
terial behavior. One way to check this assumption is by calculating
the composite material properties of a ply while it is loaded into the
inelastic range. These revised material properties (see last column of
Table 4) were found to vary only slightly, except for the shear modulus
which decreased to a value of about half. Due to the ±45° ply orienta-
tion of the laminate, the major loading stress is longitudinal shear
loading. At this high inelastic range of loading, the slope of the
shear stress-shear strain curve is much less than the elastic shear
modulus, explaining the low composite shear modulus. These values can
be used in the laminate analysis to find new load ratios, which when
compared to the original load ratios show only small errors (Table 6).
The new load ratios were calculated from data taken after the ply was

TABLE 6

ERROR ANALYSIS OF LOAD RATIO CHANGES DURING
ENTIRE LOAD EXCURSION

1000 psi Applied Axial Compressive Stress

STRESSES (psi)	ELASTIC PROPERTIES	INELASTIC PROPERTIES	PERCENT ERROR
σ_z	-912	-904	0.87
σ_x	-88	-96	9.10
τ_{xz}	500	500	0.0

axially loaded to -20 ksi to assure maximum accumulated error in load ratios. Notice in Table 6 the high axial load and longitudinal shear load while the transverse normal load is small. The 9.1 percent error accumulated in the small transverse load is negligible compared to the large axial normal load accumulation of less than one percent error. The longitudinal shear load experienced no change, which is expected in this case where both load direction and fiber direction occur in a manner such that the material can be considered specially orthotropic. Because there is no coupling between normal and shear effects in the specially orthotropic case, no change should occur in shear stress, even in the inelastic region. Therefore, it is possible to conclude that no significant error in theoretical predictions can be attributed to variation in load ratios due to inelastic behavior.

With the above assumptions in effect, the entire curing and conditioning history of each ply is approximated, as well as the effect of the applied load increments. The resulting inelastic strains at each incremental applied load are in ply coordinates and must be transformed back to laminate coordinates. This done, longitudinal stress and strain at various increments for each condition are the final results needed to compare with experimental data. Figures 23 through 26 show the predicted incremental stress-strain points compared to the experimental data curves. The complete experimental data curves to failure are not shown here, although they are available in Reference [30].

A very slight overprediction error is seen for both of the room temperature conditions, while the elevated temperature condition
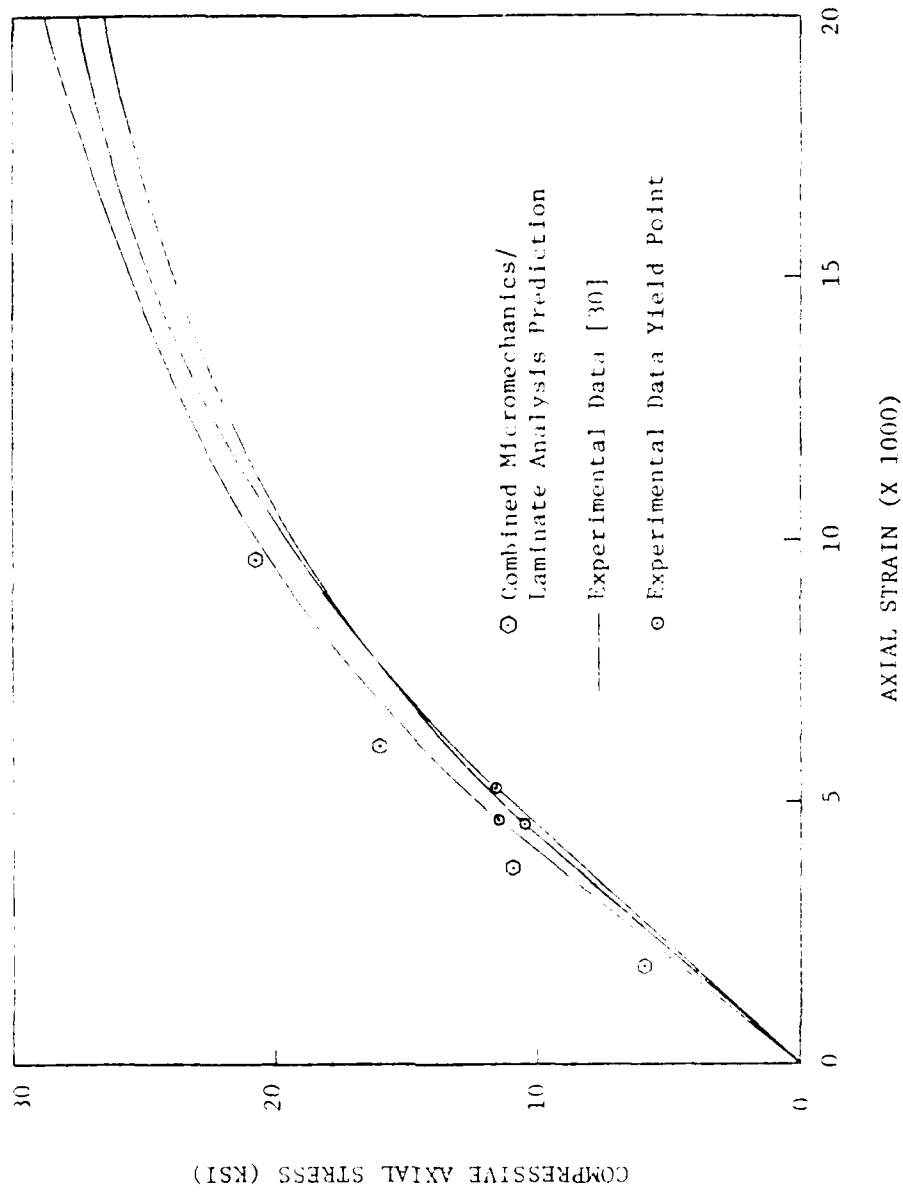
Figure 23. Comparison of room temperature, dry (RTD) experimental data [30] for a [±45 4s laminate with combined micromechanical and laminate analysis predictions.
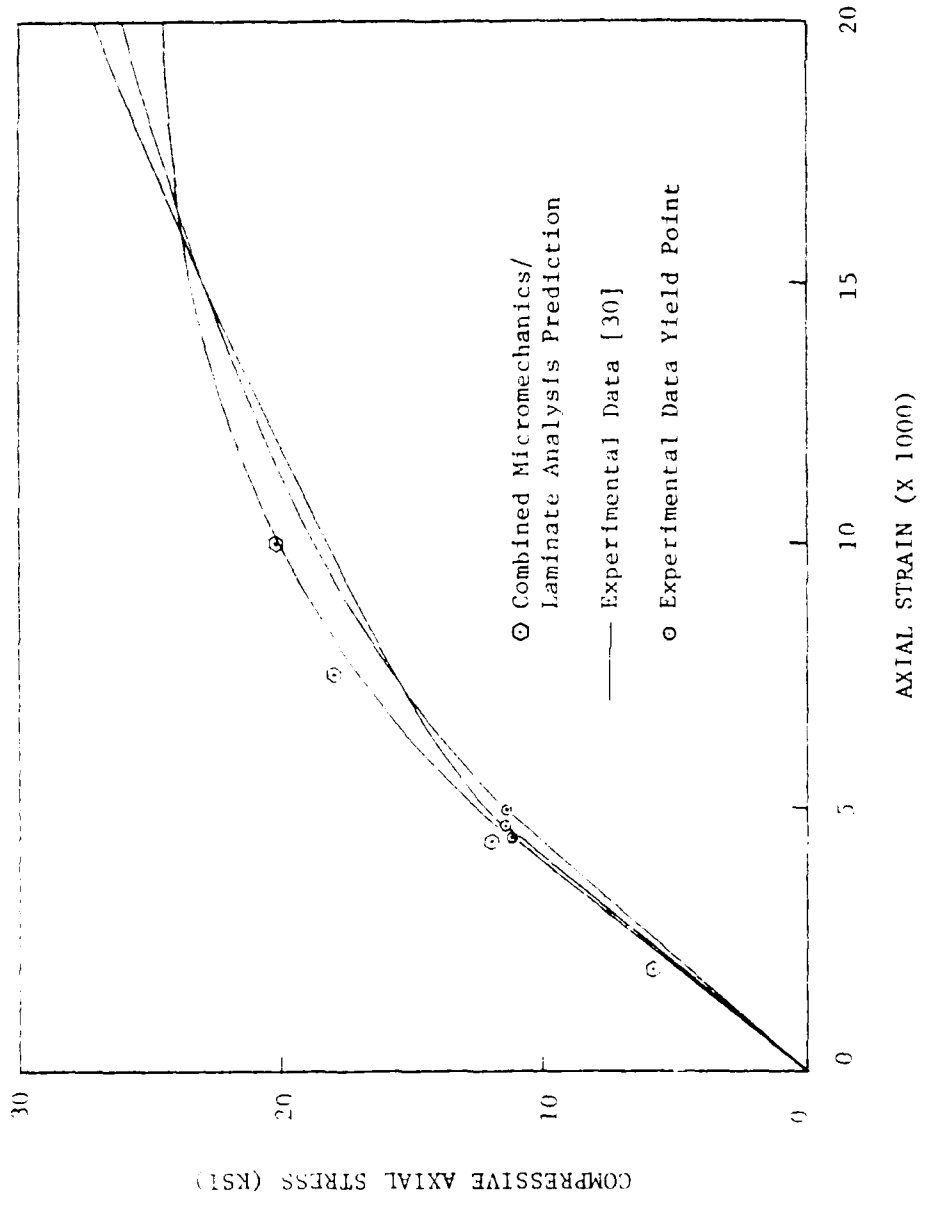
Figure 24. Comparison of room temperature, wet (RTW) experimental data [30] for a [±45]₄s laminate with combined micromechanical and laminate analysis predictions.

AXIAL STRAIN (X 1000)

○ Combined Micromechanics/
  Laminate Analysis Prediction

－ Experimental Data [30]

○ Experimental Data Yield Point

COMPRESSIVE AXIAL STRESS (KSI)
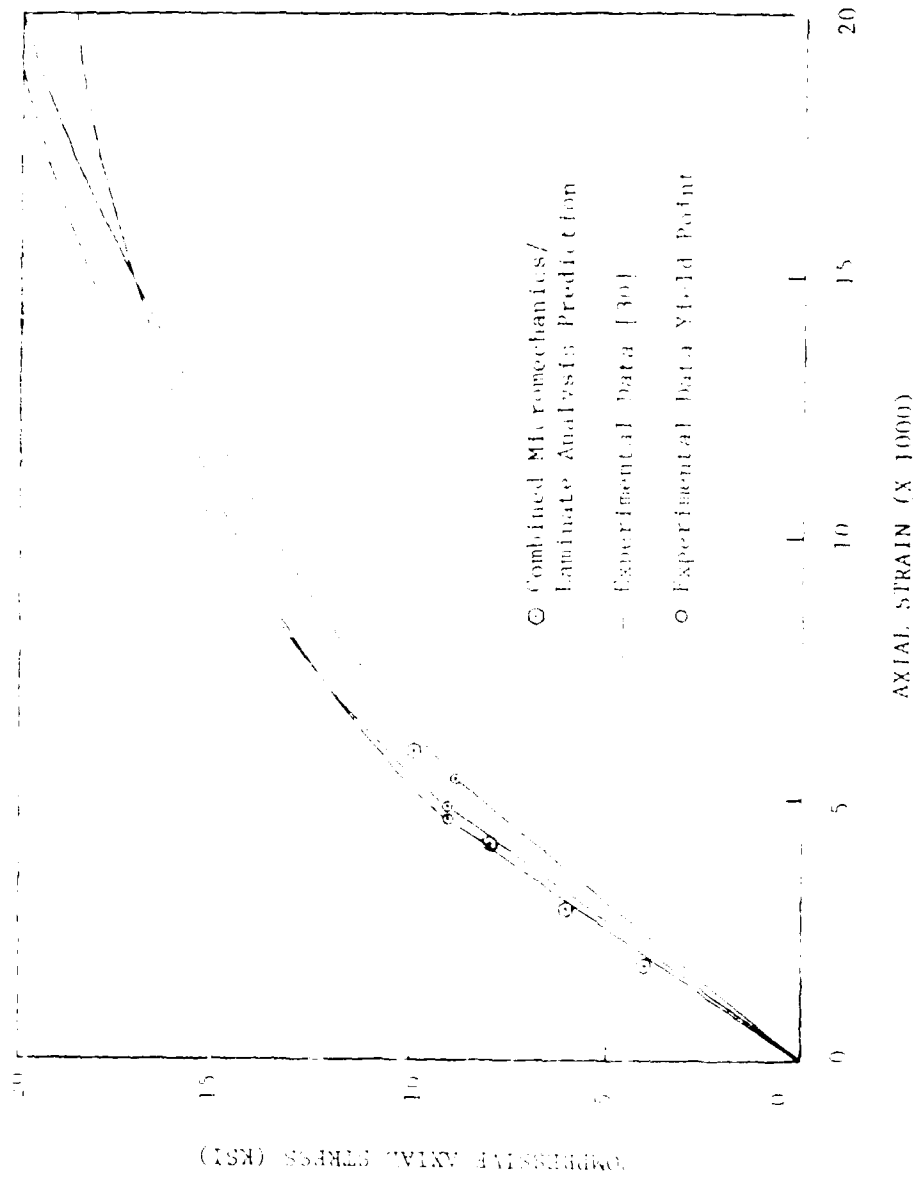
Figure 25. Comparison at elevated temperature, dry (ETD) experimental data [30] for a
[0/±45,5] laminate with combined micromechanical and laminate analysis predictions.
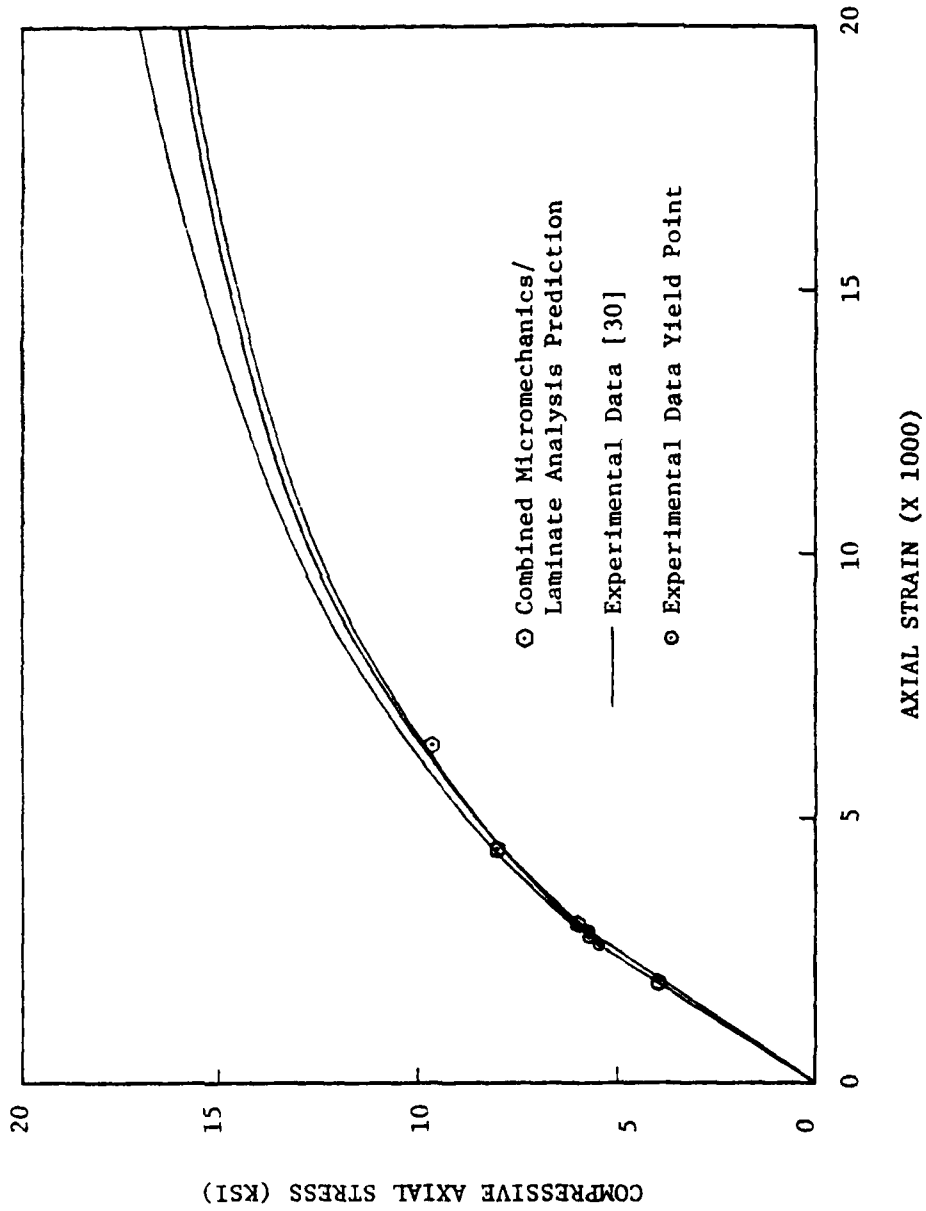
Figure 26. Comparison of elevated temperature, wet (ETW) experimental data [30] for a [±45]4s laminate with combined micromechanical and laminate analysis predictions.

predictions are in excellent agreement with experiment. Although the differences between theory and experiment are perhaps not significant, the most likely explanation for slight differences is based on flaws in the matrix or flaws in the fiber-matrix bond, as hypothesized previously for the case of pure shear loading. Again, the stress concentrations caused by these flaws reduce the strength of the material. The RTD test case (Figure 23) does show this discrepancy. Any softening of the matrix should reduce the stress concentrating effect of flaws. When moisture is added in the RTW case, (Figure 24) it serves as a plasticizer that tends to negate the thermal curing stresses. Now the actual composite behavior is slightly closer to the predicted curve for a composite with no material flaws. This theory is further supported in the elevated temperature test cases (Figures 25 and 26), where the predicted incremental values are in very close agreement with the experimental data. The elevated temperature and moisture in the ETW test case (Figure 26) again softens the matrix, reducing the effect of stress concentrators, and narrowing the gap between experiment and theory.

Neglecting interlaminar shear stresses, calculating load ratios using an elastic analysis, and assuming an effective temperature change were other possible sources of error. All of these effects could definitely increase the stresses in the matrix, which would effectively increase the matrix "damage" consequently lowering the overall stiffness and strength of the actual specimen below the predicted theoretical values.

The reason for the excellent accuracy of the analysis can be investi-
gated by observing the loading history recorded in the stress contour
plots. Also, insight into other possible sources of error may be
attained. Normalized octahedral shear stress contours for the RTD test
case are shown in Figure 27, ranging from curing stresses to the failure
stress state. Referring back to the original step-by-step description
of the laminate analysis presented earlier in this subsection, it will
be noted that hygrothermal effects are considered in separate steps.
First there are stresses induced by hygrothermally-influenced consis-
tuent material properties, (see Figure 27a). Second, other plies are
influenced by hygrothermal effects, which influence the stresses in the
representative ply now being considered (see Figure 27b). These will
be termed "ply curing effects" and "laminate curing effects", respec-
tively. Because Figure 27a is also representative of stresses in a
unidirectional composite, contrasting Figures 27a and b shows curing
stress differences between a unidirectional laminate and a $[\pm 45]$ lam-
inate. But, for the present purposes, it is important to note the
additional curing effects of the ply configuration in Figure 27b and
the magnitude of them. Any material defect which might exist in a
local region of high stress will cause a severe stress concentration,
which in turn can cause premature matrix yielding and failure. This is
a possible reason for the lower stiffness exhibited by the experimental
data at room temperature conditions. Figure 27c shows the amount of
matrix that has already yielded locally when the overall composite re-
sponse first indicates a yield point experimentally. While the tangent
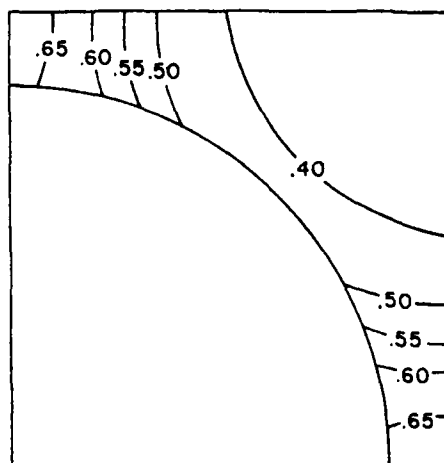
a) Octahedral shear stress
of ply alone after cool-
down from 177°C cure tem-
perature to 21°C
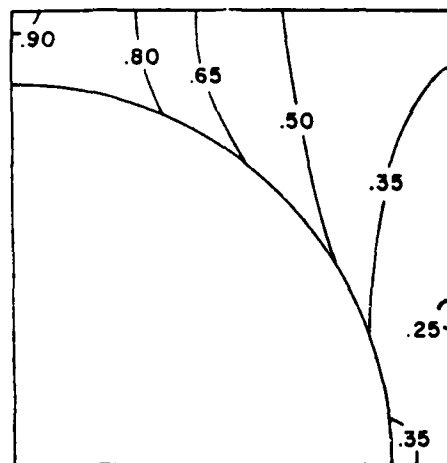
b) Octahedral shear stress
after laminate cooldown
effects
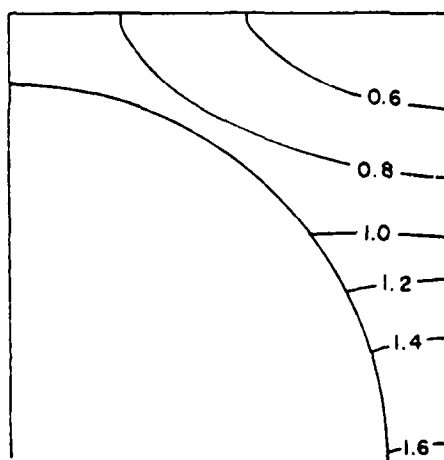
c) Octahedral shear stress at
experimentally determined
composite yield stress,
applied axial load; $\bar{\sigma}_x$ =
-11.5 ksi
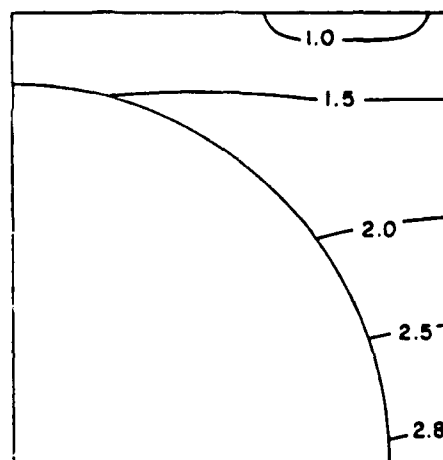
d) Octahedral shear stress at
predicted first element
failure, applied axial
load; $\bar{\sigma}_x$ = 21.0 ksi

Figure 27. Contour plots of octahedral shear (normalized with respect
to matrix yield stress, 4.18 ksi), interface normal and in-
terface shear stress within a graphite/epoxy $[\pm 45]_{4s}$ lam-
inate ply at room temperature, dry conditions (RTD).
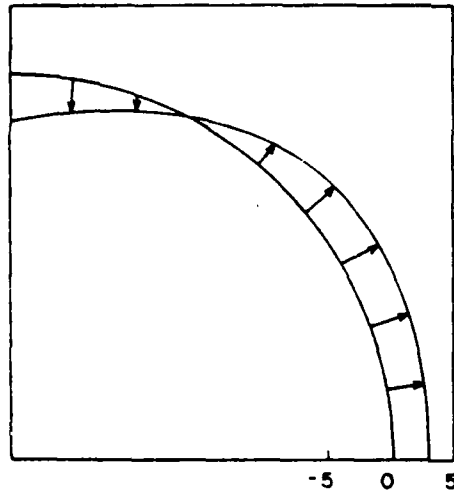
e) Interface normal stress
    (ksi) after laminate cure,
    cooldown, and moisture
    absorption effects
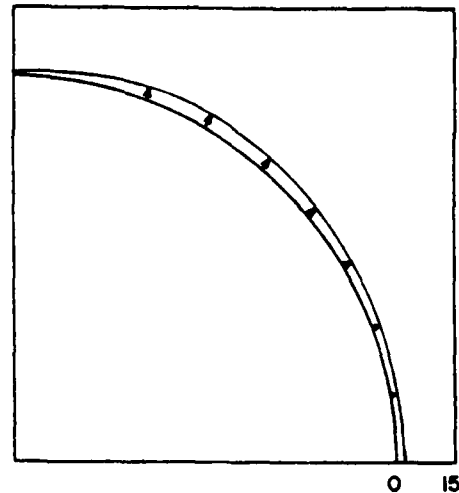
f) Interface shear stress
    (ksi) after laminate cure,
    cooldown, and moisture
    absorption effects
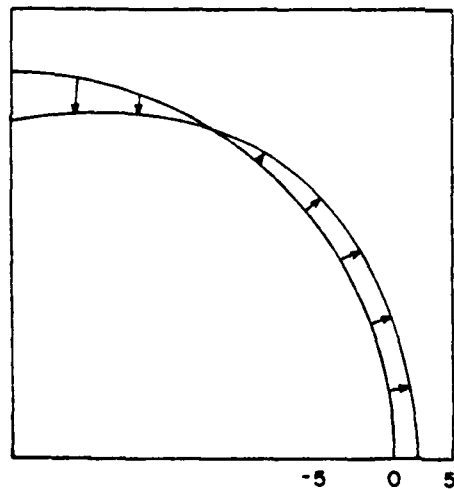
g) Interface normal stress
    (ksi) at predicted first
    element failure
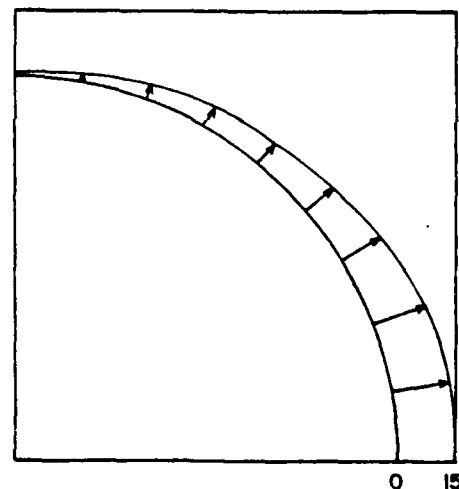
h) Interface shear stress
    (ksi) at predicted first
    element failure

(applied axial load, $\overline{\sigma}_x$ = 21.0 ksi)

Figure 27. (Continued) Contour plots of octahedral shear (normalized
            with respect to matrix yield stress, 4.18 ksi), interface
            normal and interface shear stress within a graphite/epoxy
            $[\pm 45]_{4s}$ laminate ply at room temperature, dry conditions
            (RTD).

modulus of the yielded matrix is still close to the initial modulus, the nonlinearity is not apparent in the composite response. Only after the yielded region has propagated upward a distance equal to half the width of the quadrant, do the experimental data begin to suggest an elastic limit. When the micromechanics analysis predicts first element failure, this implies the initiation of a crack. To prevent this damage initiation, the composite should thus not be loaded past the stress represented by the final predicted point in Figure 23. A more comprehensive study would reveal just how much load could safely be added beyond yield, while preventing major microcracking. After curing, the composite experiences large normal stresses along the interface, as shown in Figure 27e, suggesting a high probability of debonding behavior. There are also fairly high shear stresses along the interface in this as-cured condition, which grow enormously as load is applied and increased to predicted first failure (Figure 27f and 27h). This shear stress is the combined effect of the applied longitudinal shear stress and the transverse normal stress, which are acting in weak directions of the material, and which eventually lead to failure. It will also be noted in Figure 27g that the normal interface stress has been reduced by the applied loads. This is further evidence of how applied loads can relieve some of the stresses induced during cooldown; it is an inelastic coupling effect.

The ETW test case involves two separate forms of curing and contitioning stress. First, stresses are induced independently in each ply by thermal and moisture changes due to the difference in properties

between the fiber and matrix. Secondly, since the individual plies, exhibiting the aforementioned hygrothermal strains, are bonded to each other, they mutually affect each other because of their differing ply orientations. The combination of thermal and moisture loads has far-reaching consequences because of the opposing effects in cooldown and moisture absorption. The temperature drop during cooldown causes the matrix to contract by a relatively large amount, the fiber to contract transversely by a lesser amount, and the fiber to actually expand slightly in its axial direction, (see Table 3). The composite axial strain is predicted to be negative, as can be seen by the positive composite thermal coefficient of expansion in Table 4. Figure 28a, when compared to Figure 28b and 28c, indicates that the octahedral shear stresses induced by curing are almost fully negated by the absorption of one weight percent moisture by the composite. The small hygrothermal stresses which result are the reason for the low average laminate hygrothermal stresses shown in the last column of Table 5. However, the shifting of the octahedral shear stress contours in Figure 28c due to the application of the induced loads will be noted. This is depicted more clearly at first failure, as represented by Figure 28d. The detrimental effect of unfavorable temperature and moisture combinations is clearly shown in comparing the octahedral shear stress contours at first failure of the ETW test case compared to the RTD case. An octahedral first element failure stress of approximately 11.6 ksi (shown normalized in Figure 27d for the RTD case as the 2.8 contour) is reduced to 5.2 ksi in the ETW case (shown normalized in Figure 28d as the 2.2
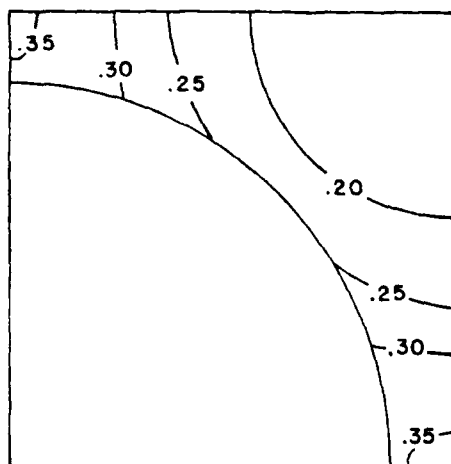
a) Octahedral shear stress of
   ply alone after cooldown
   from 177°C cure temperature
   to 103°C (normalized with
   respect to matrix yield
   stress, 2.74 ksi)
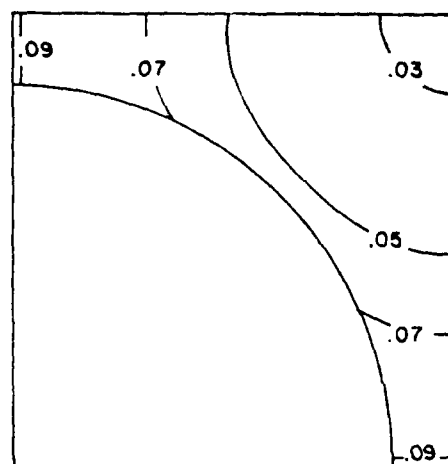
b) Octahedral shear stress
   of ply alone after 1%
   moisture absorption (nor-
   malized with respect to
   matrix yield stress, 2.58
   ksi)
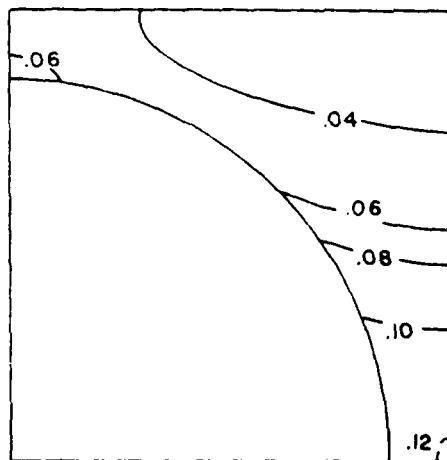
c) Octahedral shear stress
   after laminate hygrothermal
   effects
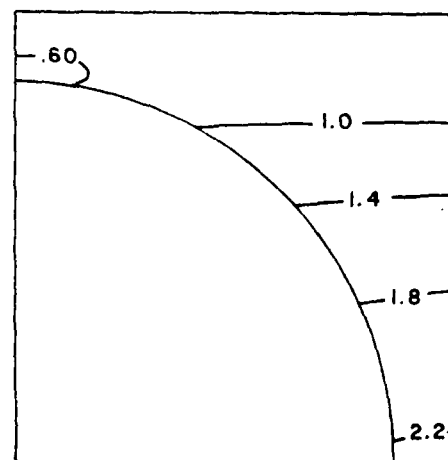
d) Octahedral shear stress at
   predicted first element
   failure, applied axial load;
   $\overline{\sigma}_x = -9.6$ ksi

(normalized with respect to matrix yield stress, 2.58 ksi)

Figure 28. Contour plots of octahedral shear, interface normal and
            interface shear stress within a graphite/epoxy $[\pm45]_{4s}$
            laminate ply at 103°C, 1% moisture by weight (ETW).
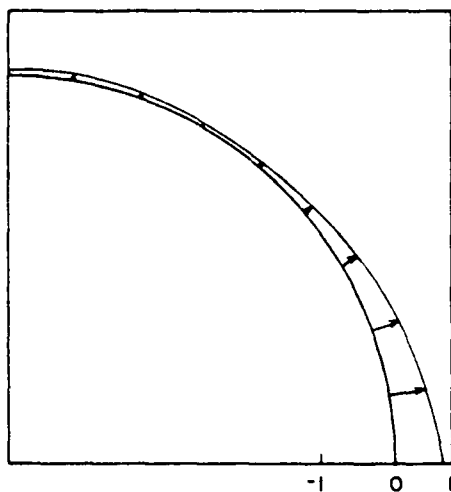
e) Interface normal stress
   (ksi) after laminate cure,
   cooldown, and moisture
   absorption effects
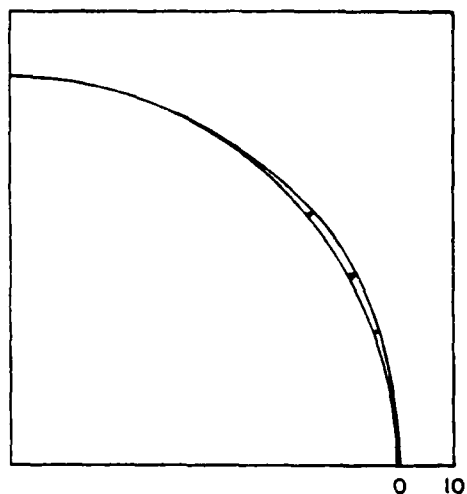
f) Interface shear stress
   (ksi) after laminate cure,
   cooldown, and moisture
   absorption effects
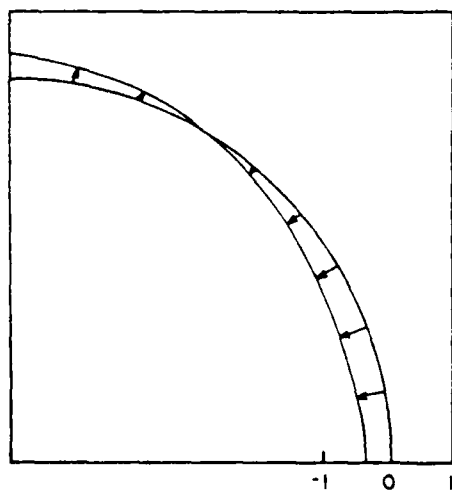
g) Interface normal stress
   (ksi) at predicted first
   element failure
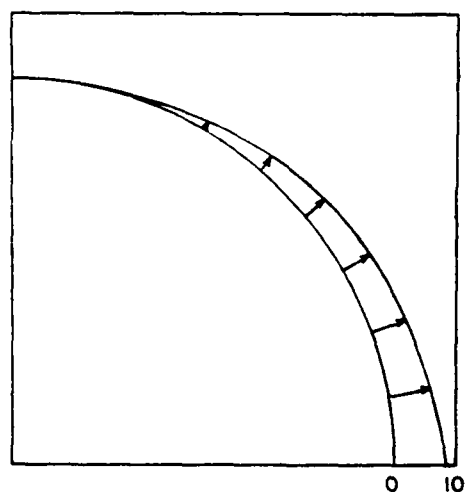
h) Interface shear stress
   (ksi) at predicted first
   element failure

(applied axial load, $\bar{\sigma}_x$ = 9.6 ksi)

Figure 28. (continued) Contour plots of octahedral shear, interface
normal and interface shear stress within a graphite/epoxy
$[\pm45]_{4s}$ laminate ply at 103°C, 1% moisture by weight (ETW).

contour). This is a significant change, considering that it is due to a relatively modest temperature change.

Interface normal stresses induced during cooldown and one percent moisture absorption are relatively small tensile stresses (see Figure 28e), but subsequent mechanical loading of the laminate counteracts the induced tensile stresses, so that near the x-axis of symmetry a small negative value exists at first element failure (Figure 28g). Small tensile stresses are induced near the y-axis of symmetry at first element failure, but are small enough that they have no noticeable effect on subsequent laminate behavior. Although the interface shear stress after curing and moisture conditioning (Figure 28f) is small (4 percent of the ultimate stress), the subsequently applied mechanical loads result in shear stresses along the interface which are very high at first element failure (Figure 28h). Although the interface shear stress is high, the octahedral shear stress is shown to be highest at the outer edge of the model, along the x-axis of symmetry (Figure 28d). Failure in this elevated temperature, one percent moisture condition would probably occur between the fibers in the region of highest octahedral shear stress. But at room temperature, dry conditions, higher stresses would be induced along the interface (see Figure 27d), increasing the probability of failure of the fiber/matrix bond. A resulting hypothesis is that because this failure is likely to occur more often in the RTD laminate, an actual laminate at these conditions has a higher probability of failure initiation due to inherent flaws in the material, especially along the fiber/matrix interface. Thus, experimental

data show a lower initial modulus and a lower overall stiffness than theory predicts, as in Figure 23.

SECTION 6

DISCUSSION

The establishment of a generalized plane strain finite element formulation that includes a longitudinal shear loading capability has further advanced composite materials technology, by making detailed information concerning the micromechanical shear loading response of composite materials available. Such a quasi-three-dimensional formulation approaches the capability of a true three-dimensional analysis, while retaining the conciseness of a two-dimensional analysis. Although the present generalized plane strain analysis only approximates a true three-dimensional analysis, the present results show that it is quite accurate, and therefore valuable in many potentia' applications.

The capabilities of the new analysis developed in the present study will first be summarized. Following a previous formulation [1], an inelastic capability is realized through the use of the tangent modulus approach, with revisions due to the addition of longitudinal shear loading. This capability enables the analysis to accommodate highly inelastic matrix materials such as annealed aluminum. The finite element formulation was adapted by making extensive revisions of the stiffness formulation and Gaussian elimination solution procedures. A special loading technique was developed, to make possible a decrease in the size of the stiffness matrix storage, increasing the efficiency of the program considerably. This, combined with a new, more efficient finite element model, results in a stiffness matrix which has the least

possible amount of wasted space. Even with this improved efficiency, however, the added longitudinal shear loading capability quadruples the size of the stiffness matrix, leading to the conclusion that if a certain problem does not necessitate longitudinal shear considerations, the previous formulation [1] which does not include a longitudinal shear capability, should be employed. Although the two analyses could be combined into one, and a selection process built into the resulting computer program, it would essentially be just that, i.e., two separate programs linked together, with no special advantage being gained.

Consistent with the previous analysis [1], another capability of the new version is combined loadings; that is, increments of temperature, moisture, and five separate applied mechanical stresses can be applied in any order, simultaneously, or in any combination. The inclusion of temperature- and moisture-dependent matrix material properties provides an added dimension in modeling real physical behavior. The program is thus a highly versatile analytical tool, with many applications yet to be explored, suggesting that future work should follow the directions discussed below.

Further verification of this new analysis is not requisite or urgent, the existing verifications being reasonably conclusive, but such work is suggested while additional developments are being undertaken. A comprehensive three-dimensional study of micromechanics should be performed to establish the amounts of error incurred by the special assumptions of generalized plane strain. Such a three-dimensional program is now operational [36]. Usefulness of the present

analysis can thus be shown, as well as those cases where it is most accurate.

With the longitudinal shear loading capability, interfacing with a laminate point stress analysis is made possible, enabling the investigation of complicated laminates. The results of the comparisons between theory and experiment for the $[\pm 45]_{4s}$ laminate presented here are encouraging, although limited to one simple laminate. However, because this particular laminate is dominated by a longitudinal shear loading mechanism, it is assumed that further investigation of various other laminates will again show good agreement with experiment.

The combined micromechanics/laminate analysis predicts only a slightly nonlinear stress-strain curve up to the point where first element failure is predicted to occur. In the present formulation, this is the termination point of the analysis. If a crack initiated at the first element failure is allowed to grow, perhaps an entire stress-strain curve could be modeled, and ultimate stresses predicted. This crack propagation capability has been developed in another micromechanical analysis program [37], which could be closely followed in incorporating a similar capability in the present program. This would provide a capability to more completely model the behavior of laminates over their entire loading range.

The trend toward adhesive bonding of composites rather than using mechanical fasteners suggests further analysis of bonding behavior. Longitudinal shear loading and viscoelastic considerations would be desirable in a study of bonds in conjunction with laminates. Because

a nonlinear viscoelastic capability is already operational in an exist-
ing micromechanics formulation [38], the present analysis could be
revised to incorporate this time-dependent response, and thus handle
special cases of generally orthotropic laminates bonded together with
adhesives, all exhibiting viscoelastic response.

Implications of the assumption of a perfect fiber/matrix bond have
been recognized by previous authors [1]. This is now especially impor-
tant when high longitudinal shear loads are applied. Results presented
here for shear test comparisons and laminate comparisons with actual
experimental data both show an overprediction, thought to be caused, at
least in part, by this assumption of a perfect fiber/matrix interface
bond. The differences are seen to decrease rapidly with increasing
temperature and moisture conditions, at which the plasticized matrix is
more readily able to accommodate the local stress disturbances caused
by the debonding in the actual material. Statistical models of flaw
distributions may also be developed in the future, so that material
properties can be adjusted to account for such damaging conditions.
This would possibly improve the already good predictions of the present
analysis.

Such further developments of the analysis presented here should
lead to the continued advancement of the design of high performance
composite structures. As such analyses develop, design parameters for
composites will become more useful and well-known. Composites will in
turn become the logical material choice for many applications, present-
ing an important alternative to the age old use of homogeneous metals.

REFERENCES

1. A. K. Miller and D. F. Adams, "Micromechanical Aspects of the Environmental Behavior of Composite Materials," Department Report UWME-DR-701-111-1, Mechanical Engineering Department, University of Wyoming, Laramie, Wyoming, January 1977.

2. D. F. Adams and D. R. Doner, "Longitudinal Shear Loading of a Unidirectional Composite," Journal of Composite Materials, Vol. 1, January 1967, pp. 4-17.

3. G. P. Sendeckyj, "Longitudinal Shear Deformation of Composites II, Stress Distribution," Journal of Composite Materials, Vol. 5, January 1971, pp. 82-93.

4. R. L. Foye, "Advanced Design Concepts for Advanced Composite Airframes," Technical Report AFML-TR-68-91, Vol. 1, North American-Rockwell Corporation, Columbus, Ohio, July 1968.

5. D. J. Baker and R. L. Foye, "Advanced Design Concepts for Advanced Composite Airframes," Technical Management Report, No. 2, North American-Rockwell Corporation, Columbus, Ohio, October 1969.

6. R. L. Foye, "Stress Concentrations and Stiffness Estimates for Rectangular Reinforcing Arrays," Journal of Composite Materials, Vol. 4, October 1970, pp. 562-566.

7. R. L. Foye, "Theoretical Post Yielding Behavior of Composite Laminates, Part I - Inelastic Micromechanics," Journal of Composite Materials, Vol. 7, April 1973, pp. 178-193.

8. P. V. Marcal, "A Comparative Study of Numerical Methods of Elastic-Plastic Analysis," Technical Note, AIAA Journal, Vol. 6, No. 1, January 1968, pp. 157-158.

9. D. F. Adams, "Inelastic Analysis of a Unidirectional Composite Subjected to Transverse Normal Loading," Journal of Composite Materials, Vol. 4, July 1970, pp. 310-328.

10. D. F. Adams, "Inelastic Analysis of a Unidirectional Composite Subjected to Transverse Normal Loading," Report RM-6245-PR, The Rand Corporation, May 1970.

11. D. F. Adams, "High Performance Composite Materials for Vehicle Construction: An Elastoplastic Analysis of Crack Propagation," Report R-1070-PR, The Rand Corporation, Santa Monica, California, March 1973.

12. D. F. Adams, "Elastoplastic Crack Propagation in a Transversely Loaded Unidirectional Composite," Journal of Composite Materials, Vol. 8, January 1974, pp. 38-54.

13. D. F. Adams, "Practical Problems Associated with the Application of the Finite Element Method to Composite Material Micromechanical Analyses," Fibre Science and Technology, Vol. 7, No. 2, April 1974, pp. 111-122.

14. D. F. Adams, "A Micromechanical Analysis of Crack Propagation in an Elastoplastic Composite Material," Fibre Science and Technology, Vol. 7, No. 4, October 1974, pp. 237-256.

15. D. F. Adams and A. K. Miller, "Hygrothermal Microstresses in a Unidirectional Composite Exhibiting Inelastic Material Behavior," Journal of Composite Materials, Vol. 11, No. 3, July 1977, pp. 285-299.

16. A. K. Miller and D. F. Adams, "Inelastic Finite Element Analysis of a Heterogeneous Medium Exhibiting Temperature and Moisture Dependent Material Properties," Fibre Science and Technology, Vol. 13, No. 2, March-April 1980, pp. 135-153.

17. F. W. Crossman, "Computer Simulation of the Deformation of Composite Materials by Finite Element Analysis," Ph.D. Thesis, Stanford University, Stanford, California, 1974.

18. T. R. Brennan, "Creep of a Uniaxial Fiber Composite Subjected to a Steady State Normal Load," Ph.D. Thesis, Theoretical and Applied Mechanics, University of Illinois, Urbana, Illinois, June 1971.

19. S. G. Leknitskii, Theory of Elasticity of an Anisotropic Elastic Body, San Francisco: Holden-Day, Inc., 1963.

20. D. F. Adams and S. W. Tsai, "The Influence of Random Filament Packing on the Transverse Stiffness of Unidirectional Composites," Journal of Composite Materials, Vol. 3, 1969, pp. 368-381.

21. O. C. Zienkiewicz, The Finite Element Method, McGraw-Hill Book Co., New York, New York, 1977.

22. L. J. Segerlind, Applied Finite Element Analysis, John Wiley and Sons, Inc., New York, New York, 1976.

23. S. W. Tsai and E. M. Wu, "A General Theory of Strength for Anisotropic Materials," Journal of Composite Materials, Vol. 5, January 1971, pp. 58-80.

24. R. M. Jones, Mechanics of Composite Materials, Scripta Book Co., Washington, D.C., 1975.

25. R. Narayanswami and H. M. Adelman, "Evaluation of the Tensor Polynomial and Hoffman Strength Theories for Composite Materials," Journal of Composite Materials, Vol. 11, October 1977, pp. 366-377.

26. Unpublished Experimental Data for Hercules 3501-6 Epoxy Matrix, Composite Materials Research Group, Department of Mechanical Engineering, University of Wyoming, Laramie, Wyoming, 1978.

27. Unpublished Solid Rod Torsion Experimental Data, Composite Materials Research Group, Department of Mechanical Engineering, University of Wyoming, Laramie, Wyoming, 1978.

28. D. F. Adams and R. L. Thomas, "The Solid Rod Torsion Test for the Determination of Unidirectional Composite Shear Properties," Textile Research Journal, Vol. 39, No. 4, April 1969, pp. 339-345.

29. A. P. Boresi and P. P. Lynn, Elasticity in Engineering Mechanics, Prentice-Hall, New Jersey, 1974.

30. G. C. Grimes and D. F. Adams, "Investigation of Compression Fatigue Properties of Advanced Composites," Northrop Technical Report NOR 79-17, Northrop Corporation, Hawthorne, California; University of Wyoming, Laramie, Wyoming, October 1979.

31. R. M. Richard and G. M. Blacklock, "Finite Element Analysis of Inelastic Structures," AIAA Journal, Vol. 7, No. 3, March 1969, pp. 432-438.

32. C. E. Browning, "The Mechanisms of Elevated Temperature Property Losses in High Performance Structural Epoxy Resin Matrix Materials After Exposures to High Humidity Environments," Technical Report AFML-TR-76-153, Air Force Materials Laboratory, Wright-Patterson Air Force Base, Ohio, March 1977.

33. "Hercules Magnamite Graphite Fibers," Hercules, Inc., Wilmington, Delaware, 1978.

34. "Textile Fibers for Industry," Owens-Corning Fiberglass Corporation, Toledo, Ohio, 1971.

35. R. D. Kriz, W. W. Stinchcomb and D. R. Tenney, "Effects of Moisture, Residual Curing Stresses and Mechanical Load on the Damage Development in Quasi-Isotropic Laminates," Report No. 16, NASA-Virginia Tech. Composites Program, February 1980.

36. M. M. Monib and D. F. Adams, "Nonlinear Three-Dimensional Finite
     Element Analysis of Composite Laminates," Department Report UWME-
     DR-001-102-1, Department of Mechanical Engineering, University of
     Wyoming, Laramie, Wyoming, November 1980.

37. D. P. Murphy and D. F. Adams, "Energy Absorption Mechanisms During
     Crack Propagation in Metal Matrix Composites," Department Report
     UWME-DR-901-103-1, Department of Mechanical Engineering, University
     of Wyoming, Laramie, Wyoming, October 1979.

38. B. G. Schaffer and D. F. Adams, "Nonlinear Viscoelastic Behavior
     of a Composite Material Using a Finite Element Micromechanical
     Analysis," Department Report UWME-DR-001-101-1, Department of
     Mechanical Engineering, University of Wyoming, Laramie, Wyoming,
     June 1980.

39. Y. C. Fung, A First Course in Continuum Mechanics, Prentice-Hall,
     Inc., Englewood Cliffs, New Jersey, 1977.

40. J. L. Swedlow, "Elasto-Plastic Cracked Plates in Plane Strain,"
     International Journal of Fracture Mechanics, Vol. 5, No. 1, March
     1969, pp. 33-44.

APPENDIX A

ISOTROPIC CONSTITUTIVE EQUATION
FOR ELASTOPLASTIC BEHAVIOR

The Prandtl-Reuss flow rule is employed to characterize elasto-
plastic behavior by relating the plastic strain tensor to the devi-
atoric stress as depicted in Eq. (A-1):

$$\varepsilon_{ij}^{(p)} = \lambda s_{ij} \qquad (A-1)$$

where $\varepsilon_{ij}^{(p)}$ is the plastic strain tensor, λ is a positive scalar, and
s_{ij} is the deviatoric stress tensor. From this, a constitutive
equation expressing stress in terms of strain is developed. Index
notation closely following the form by Fung [39] is used in this
derivation. This analysis was developed in terms of incremental
stress and strain for a generalized plane strain formulation by
Adams [11], based upon work by Swedlow [40]. The term λ in Eq.
(A-1) is thus developed as implied in Eq. (A-2):

$$\varepsilon_{ij}^{(p)} = \left(\frac{s_{kl}\dot{\sigma}_{kl}}{6\tau_0\, 2M_T} \right) s_{ij} \qquad (A-2)$$

where the dots indicate increments of stress and strain, as distin-
guished from the total stress or strain of the material, $\tau_0 = (\frac{1}{3} s_{ij}s_{ij})^{\frac{1}{2}}$ is the octahedral shear stress, $2M_T$ is the tangent modulus
of the octahedral shear stress - octahedral plastic shear strain curve,
and $\dot{\sigma}_{kl}$ represents the incremental stress tensor. Adding elastic
incremental strains to the plastic component above yields the overall
expression for incremental strain [11],

$$\varepsilon_{ij} = \frac{1+\nu}{E}\dot{\sigma}_{ij} - \frac{\nu}{E}\dot{\sigma}_{kk}\delta_{ij} + \frac{s_{ij}s_{kl}\dot{\sigma}_{kl}}{6\tau_0{}^2 M_T} \qquad (A-3)$$

To obtain an equation for stress in terms of strain, Eq. (A-3) must be inverted. Inverting this three-dimensional form follows closely the procedure for the case of plane strain [11]. The first step is to express the second and third terms on the right-hand side of Eq. (A-3) in terms of strains by multiplying Eq. (A-3) by the Kronecker delta (δ_{ij}), and simplifying,

$$\dot{\varepsilon}_{ii} = \frac{1+\nu}{E}\dot{\sigma}_{ii} - \frac{3\nu}{E}\dot{\sigma}_{kk} + \frac{s_{ii}s_{kl}\dot{\sigma}_{kl}}{6\tau_0{}^2 M_T} \qquad (A-4)$$

It will be noted that s_{ii} is the first invariant of the deviatoric stress tensor, which is identically zero. Thus, Eq. (A-4) becomes

$$\dot{\varepsilon}_{ii} = \frac{1-2\nu}{E}\dot{\sigma}_{ii} \qquad (A-5)$$

which is easily inverted to obtain an expression for the second term:

$$\dot{\sigma}_{ii} = (\frac{E}{1-2\nu})\dot{\varepsilon}_{ii} \qquad (A-6)$$

For the third term, Eq. (A-3) is multiplied by the deviatoric stress tensor s_{ij}, and simplified,

$$s_{ij}\dot{\varepsilon}_{ij} = s_{ij}\dot{\sigma}_{ij}(\frac{1+\nu}{E}) - \frac{\nu}{E}\dot{\sigma}_{kk}s_{ii} + \frac{s_{kl}\dot{\sigma}_{kl}}{2M_T} \qquad (A-7)$$

This can be expressed as

$$s_{ij}\dot{\varepsilon}_{ij} = s_{ij}\dot{\sigma}_{ij}(\frac{2M_T(1+\nu)+E}{2M_T E}) \qquad (A-8)$$

Finally, solving for $s_{ij}\dot{\sigma}_{ij}$ results in

$$s_{ij}\dot{\sigma}_{ij} = \frac{2M_T E}{2M_T(1+\nu)+E}s_{ij}\dot{\varepsilon}_{ij} \qquad (A-9)$$

which when substituted into Eq. (A-3) along with Eq. (A-6) results
in the desired constitutive equation:

$$\sigma_{ij} = \frac{E}{1 + \nu}\dot{\epsilon}_{ij} + \frac{\nu}{1 - 2\nu}\dot{\epsilon}_{ii}\delta_{ij} - \frac{s_{ij}s_{kl}\dot{\epsilon}_{kl}}{B} \qquad \text{(A-10)}$$

where

$$B = \frac{3\tau_o^2}{E} \; 2M_T(1 + \nu) + E .$$

Expanding Eq. (A-10) in matrix form results in the more useful form
represented by Eq. (6).

APPENDIX B

TWO-DIMENSIONAL GENERALIZED PLANE STRAIN FORMULATION

The displacement components must be in the following form for generalized plane strain, as previously described:

$$u = u(x,y)$$
$$v = v(x,y) \qquad \qquad \text{(B-1)}$$
$$w = w(x,y) + C_1 z$$

The changes involved in converting from plane strain to generalized plane strain will affect the strain-displacement relation and subsequently the entire stiffness formulation. Following the derivation by Zienkiewicz [21], and including the new generalized features of plane strain, the strain-displacement behavior of a triangular element is derived below.

The form for the desired elemental strain-displacement relationship will be:

$$\{F\} = [N]\{\delta\} \qquad \qquad \text{(B-2)}$$

where $\{F\}$ represents displacements at any point within the element, $\{\delta\}$ represents nodal displacements of the element, and the $[N]$ are shape functions, the general functions of position. Considering Eqs. (B-1), the expression in Eq. (B-2) can be specified in terms of generalized plane strain:

$$\{F\} = \left\{ \begin{array}{l} u(x,y) \\ v(x,y) \\ w(x,y,z) \end{array} \right\} \tag{B-3}$$

$$\delta_i = \left\{ \begin{array}{l} u_i \\ v_i \\ w_i \end{array} \right\} \tag{B-4}$$

where the displacement subscript represents a certain node. To solve for the shape functions, a linear polynomial is chosen for each displacement equation. Thus, the "constant strain" element is created, as defined by

$$u = \alpha_1 + \alpha_2 x + \alpha_3 y$$

$$v = \alpha_4 + \alpha_5 x + \alpha_6 y \tag{B-5}$$

$$w = \alpha_7 + \alpha_8 x + \alpha_9 y + \alpha_{10} z$$

Applying nodal conditions to the expressions for u and v follows the work of Zienkiewicz [21] exactly, resulting in representations of displacements in terms of shape functions and nodal displacements:

$$N_i = (a_i + b_i x + c_i y)/2A \tag{B-6}$$

where

$$a_i = X_j Y_k - X_k Y_j$$

$$b_i = Y_j - Y_k$$

$$c_i = X_k - X_j$$

Shape functions N_j and N_k follow the same pattern. It will be noted that the shape functions are functions of nodal coordinates and element area. Expressions for u and v become:

$$u = N_i u_i + N_j u_j + N_k u_k$$

$$v = N_i v_i + N_j v_j + N_k v_k \qquad (B\text{-}7)$$

The nodal conditions for w displacements require that a normal load in the z-direction induce a constant displacement, w_n, regardless of x and y coordinate positions. Assuming the model to have a thickness of unity,

$$w = w_i \quad @ \ z = 0$$

$$w = w_n + w_i \quad @ \ z = 1 \qquad (B\text{-}8)$$

Applying these conditions to the third of Eqs. (B-5):

$$w_i = \alpha_7 + \alpha_8 x + \alpha_9 y$$

$$w_n + w_i = \alpha_7 + \alpha_8 x + \alpha_9 y + \alpha_{10}(1) \qquad (B\text{-}9)$$

Subtracting the first of Eqs. (B-9) from the second results in

$$w_n = \alpha_{10} \qquad (B\text{-}10)$$

Substituting back into the third of Eqs. (B-5):

$$w = \alpha_7 + \alpha_8 x + \alpha_9 y + w_n z \qquad (B\text{-}11)$$

Rearranging,

$$w - w_n z = \alpha_7 + \alpha_8 x + \alpha_9 y \qquad (B\text{-}12)$$

Solving (B-12) for the shape functions is exactly like that used to obtain the solutions for u and v, resulting in the same form of expressions for the shape functions

$$w - w_n z = N_i w_i + N_j w_j + N_k w_k \qquad (B\text{-}13)$$

Rearranging gives the final expression for w in terms of the element shapes and nodal displacements,

$$w = N_i w_i + N_j w_j + N_k w_k + w_n z \qquad (B\text{-}14)$$

To express the element strains in terms of nodal displacements, the strain-displacement relations of a continuum must be followed,

$$\varepsilon_x = \frac{\partial u}{\partial x} \qquad \gamma_{xy} = \frac{\partial u}{\partial y} + \frac{\partial v}{\partial x}$$

$$\varepsilon_y = \frac{\partial v}{\partial y} \qquad \gamma_{xz} = \frac{\partial u}{\partial z} + \frac{\partial w}{\partial x} \qquad (B-15)$$

$$\varepsilon_z = \frac{\partial w}{\partial z} \qquad \gamma_{yz} = \frac{\partial v}{\partial z} + \frac{\partial w}{\partial y}$$

Using Eqs. (B-7) and (B-14) in Eqs. (B-15) results in the following equations:

$$\varepsilon_x = \frac{\partial u}{\partial x} = \frac{1}{2A} \{b_i \; b_j \; b_k\} \begin{Bmatrix} u_i \\ u_j \\ u_k \end{Bmatrix}$$

$$\varepsilon_y = \frac{\partial v}{\partial y} = \frac{1}{2A} \{c_i \; c_j \; c_k\} \begin{Bmatrix} v_i \\ v_j \\ v_k \end{Bmatrix}$$

$$\varepsilon_z = \frac{\partial w}{\partial z} = w_n$$

$$\gamma_{xy} = \frac{\partial u}{\partial y} + \frac{\partial v}{\partial x} = \frac{1}{2A} \{c_i \; b_i \; c_j \; b_j \; c_k \; b_k\} \begin{Bmatrix} u_i \\ v_i \\ u_j \\ v_j \\ u_k \\ v_k \end{Bmatrix} \qquad (B-16)$$

$$\gamma_{xz} = \frac{\partial w}{\partial x} + \frac{\partial u}{\partial z} = \frac{1}{2A} \{b_i \; b_j \; b_k\} \begin{Bmatrix} w_i \\ w_j \\ w_k \end{Bmatrix}$$

$$\gamma_{yz} = \frac{\partial w}{\partial y} + \frac{\partial v}{\partial z} = \frac{1}{2A} \{c_i \; c_j \; c_k\} \begin{Bmatrix} w_i \\ w_j \\ w_k \end{Bmatrix}$$

Combined into matrix form, the strain-displacement relations for generalized plane strain are defined by

$$
\begin{Bmatrix}
\varepsilon_x \\
\varepsilon_y \\
\gamma_{xy} \\
\gamma_{xz} \\
\gamma_{yz} \\
\varepsilon_z
\end{Bmatrix}
= \frac{1}{2A}
\begin{bmatrix}
b_i & 0 & 0 & b_j & 0 & 0 & b_k & 0 & 0 & 0 \\
0 & c_i & 0 & 0 & c_j & 0 & 0 & c_k & 0 & 0 \\
c_i & b_i & 0 & c_j & b_j & 0 & c_k & b_k & 0 & 0 \\
0 & 0 & b_i & 0 & 0 & b_j & 0 & 0 & b_k & 0 \\
0 & 0 & c_i & 0 & 0 & c_j & 0 & 0 & c_k & 0 \\
0 & 0 & 0 & 0 & 0 & 0 & 0 & 0 & 0 & 2A
\end{bmatrix}
\begin{Bmatrix}
u_i \\
v_i \\
w_i \\
u_j \\
v_j \\
w_j \\
u_k \\
v_k \\
w_k \\
w_n
\end{Bmatrix}
\qquad (B-17)
$$

APPENDIX C

COMPUTER PROGRAM
FLOW CHART

MAIN
An administrative program which calls the working subroutines in the proper order. Reads administrative data, i.e., titles, fiber volume, scale factors for plotting, number of loads, output flags, initial temperature, and moisture content. Loop on load increments.

GDATA
Reads mesh data for the finite element model, establishes node point coordinates and connectivity, boundary conditions and expected bandwidth of the global stiffness matrix. Builds the boundary condition vector and indicating vector for special elimination operations in forming the stiffness matrix.

MESH
Plots the finite element grid.

LOAD
Reads applied loads including hygrothermal loads and output flags. Writes out applied loads, accumulated loads, and material properties. This subroutine administrates the formation of the load vector for the specialized Branca [10] solution technique.

RESL
Determines the residual nodal loads due to material dilitation.

FORMK
Administrates the formation of the global stiffness matrix by calling respective subroutines that form elemental stiffness matrices. Forms global stiff-ness matrix in upper triangular form and simul-taneously eliminates rows and columns where boundary conditions are involved.

Inelastic behavior in element?

yes

no

FORMK

STIFT?

Forms the elemental stiffness matrix for elastic behavior

PLASTC(N)

Forms elemental stiffness matrix for inelastic behavior

ELPROP

Calculates material properties as a function of moisture and temperature. Octahedral values are available for inelastic behavior and failure analysis.

PLPROP

Calculates plasticity constants.

SOLVE

Solves simultaneous equations using specialized Gaussian elimination for a triangularized matrix with special Branca [10] boundary condition columns. The resulting displacements in condensed form are expanded to the original size for all nodes for subroutine STRESS.

STRESS

Administrates calculations of stress and failure criteria. Calculates and outputs incremental and total stresses and strains. Checks for unloading elements. Administrates calculations of principal stresses and interface stresses. Checks for hydrostatic failure. Return to MAIN for next load increment.

CMSTR

Calculates elemental stresses and adds hygro-thermal stresses.

OCTA

Checks for octahedral failure or fiber failure and sets failure flags for STRESS. Calculates failure ratio if applied stresses are higher than failure stresses.

OCSTN

Calculates element octahedral shear strains.

PRINCE

Calculates principal values for stress or strain tensor.

DISTRIBUTION LIST

No. of Copies	To
1	Office of the Under Secretary of Defense for Research and Engineering, The Pentagon, Washington, D.C. 20301
12	Commander, Defense Technical Information Center, Cameron Station, Building 5, 5010 Duke Street, Alexandria, Virginia 22314
1	Metals and Ceramics Information Center, Battelle Columbus Laboratories, 505 King Avenue, Columbus, Ohio 43201
1	ATTN: Dr. Bruce Peterson
	Deputy Chief of Staff, Research, Development, and Acquisition, Headquarters, Department of the Army, Washington, D.C. 20310
1	ATTN: DAMA-ARZ
2	Dr. J. I. Bryant
	Commander, Army Research Office, P.O. Box 12211, Research Triangle Park, North Carolina 27709
1	ATTN: Information Processing Office
2	Dr. J. Hurt
1	Dr. G. Mayer
1	Dr. D. Squire
	Commander, U.S. Army Materiel Development and Readiness Command, 5001 Eisenhower Avenue, Alexandria, Virginia 22333
1	ATTN: DRCLDC
	Commander, U.S. Army Armament Research and Development Command, Dover, New Jersey 07801
1	ATTN: Mr. H. Pebly, PLASTEC
1	Mr. A. Slobodzinski, PLASTEC
1	Mr. W. Tanner
	Commander, U.S. Army Natick Research and Development Command, Natick, Massachusetts 01760
1	ATTN: Technical Library
	Commander, U.S. Army Aviation Research and Development Command, 4300 Goodfellow Boulevard, St. Louis, Missouri 63120
1	ATTN: Mr. R. Vollmer
	Commander, Harry Diamond Laboratories, 2800 Powder Mill Road, Adelphi, Maryland 20783
1	ATTN: Technical Information Office
	Commander, U.S. Army Foreign Science and Technology Center, 220 7th Street, N.E., Charlottesville, Virginia 22901
1	ATTN: Military Tech, Mr. Marley

Director, Eustis Directorate, U.S. Army Air Mobility Research and
Development Laboratory, Fort Eustis, Virginia
ATTN: A. Gustavson

Chief of Naval Research, Arlington, Virginia
1   ATTN: Code 471

Director, Naval Research, Boston Branch, 495 Summer Street,
Boston, Massachusetts   02210
ATTN: Dr. L. H. Peebles

Naval Research Laboratory, Washington, D.C.
ATTN: Dr. W. B. Moniz, Code 6120
        Dr. I. Wolock, Code 8455
        Dr. W. D. Bascom, Code 6120
        Dr. L. B. Lockhart, Jr., Code 6120

Commander, Naval Air Systems Command, Washington, D.C.
ATTN: Mr. C. Bersch

Commander, Naval Surface Weapons Center, White Oak,
Silver Spring, Maryland   20910
ATTN: Dr. J. M. Augl

Air Force Office of Scientific Research (NC), Building 410,
Bolling Air Force Base, Washington, D.C.
ATTN: Dr. D. R. Ulrich

Air Force Materials Laboratory, Wright-Patterson Air Force Base, Ohio   45433
ATTN: Dr. S. W. Tsai
        Dr. N. J. Pagano
        Dr. H. T. Hahn
        Dr. C. E. Browning

Air Force Flight Dynamics Laboratory, Wright-Patterson Air Force Base,
Ohio   45433
ATTN: Dr. G. P. Sendeckyj

National Aeronautics and Space Administration, Lewis Research Center,
21000 Brookpark Road, Cleveland, Ohio   44135
ATTN: Dr. T. T. Serafini (49-1)
        Dr. C. C. Chamis

Massachusetts Institute of Technology, Cambridge, Massachusetts   02159
ATTN: Prof. F. J. McGarry
        Prof. C. S. P. Sung
        Dr. J. F. Mandell

Professor K. H. G. Ashbee, University of Bristol, H. H. Wills Physics Lab.,
Bristol, England BS81TL

117

No. of Copies	To

1   Professor O. Ishai, Department of Mechanics, Technicon – Israel Institute of Technology, Haifa, Israel

1   Dr. D. H. Kaelble, Science Center, Rockwell International, Thousand Oaks, California 91360

1   Dr. B. W. Rosen, Materials Science Corporation, Blue Bell, Pennsylvania 19422

Defense Research Establishment Office, Sheelay Bay, Ottawa, Ontario KIA 0Z4
1   ATTN: Mr. H. L. Nash
1   P. McLean

Defence Standard Laboratories, Department of Supply, P.O. Box 50, Ascot Vale 3052, Victoria, Australia
1   ATTN: Dr. D. Pinkerton
1   Dr. G. George

Owens Corning Fiberglass, Technical Center, P.O. Box 415, Granville, Ohio 43023
1   ATTN: Dr. R. Wong

Case Western Reserve University, Cleveland, Ohio 44106
1   ATTN: Prof. J. Koenig

Iowa State University, Ames, Iowa 50011
1   ATTN: Prof. G. Martin

Virginia Polytechnic Institute and State University, Blacksburg, Virginia 24061
1   ATTN: Dr. K. L. Reifsnider

Princeton University, Princeton, New Jersey 08540
1   ATTN: Prof. J. Gillham

Director, Army Materials and Mechanics Research Center, Watertown, Massachusetts 02172
2   ATTN: DRXMR-PL
1   DRXMR-PR
1   DRXMR-PD
1   DRXMR-AP
5   DRXMR-RC, Dr. R. W. Lewis

A micromechanical region of a unidirectional composite is modeled by a finite element micromechanical analysis using a generalized plane strain formulation, but including longitudinal shear loading. The analysis is capable of treating elastic, plastic, transversely isotropic fiber materials, as well as isotropic or elastoplastic matrix materials. Matrix material properties are considered to be temperature- and/or moisture-dependent. A special Gaussian elimination procedure is modified for the present treatment. Stresses are calculated for each element and appropriate failure criteria invoked. Fiber-element failure is the limit of the present analysis. Other possible forms of results are: unidirectional composite properties, overall composite stress-strain response, and various plots of internal stress contours.

A micromechanical region of a unidirectional composite is modeled by a finite element micromechanical analysis using a generalized plane strain formulation, but including longitudinal shear loading. The analysis is capable of treating elastic, plastic, transversely isotropic fiber materials, as well as isotropic or elastoplastic matrix materials. Matrix material properties are considered to be temperature- and/or moisture-dependent. A special Gaussian elimination procedure is modified for the present treatment. Stresses are calculated for each element and appropriate failure criteria invoked. Fiber-element failure is the limit of the present analysis. Other possible forms of results are: unidirectional composite properties, overall composite stress-strain response, and various plots of internal stress contours.

DATE
FILMED

8